Oxygen Engineered Hafnium Oxide Thin Films grown by Reactive Molecular Beam Epitaxy

TECHNISCHE
UNIVERSITÄT
DARMSTADT

vom Fachbereich
Material- und Geowissenschaften

genehmigte

Dissertation

zur Erlangung des akademischen Grades
eines Doktors der Ingenieurwissenschaften (Dr.-Ing.)

von

Dipl.-Ing. Erwin Matti Hildebrandt

geb. in Darmstadt

Darmstadt 2013

D17

Referent:	Prof. Dr. Lambert Alff
Zweitreferent:	Prof. Dr. Thomas Schröder
Tag der Einreichung:	14.12.2012
Tag der Disputation:	28.02.2013

Acknowledgements

Zuvorderst möchte ich mich bei Herrn **Prof. Dr. Lambert Alff** für die Gelegenheit zur Anfertigung einer Dissertation im Fachgebiet Dünne Schichten bedanken. Weiterer Dank gebührt überdies

Herrn **Prof. Dr. Thomas Schröder** für die freundliche Übernahme der Rolle des Zweitgutachters.

Herrn **Prof. Dr. Wolfgang Ensinger** und Herrn **Prof. Dr. Wolfgang Donner** für die freundliche Übernahme der weiteren Prüfungsverantwortung.

dem **LOEWE-Zentrum AdRIA** für die überwiegende Finanzierung meiner Promotion und **allen Mitarbeitern** von AdRIA für die gute Zusammenarbeit.

Dr. Jose Kurian for his support during my doctoral thesis, for introducing me into the world of science and to reactive molecular beam epitaxy.

Herrn **Jürgen Schreeck**, Frau **Gabi Haindl** und Herrn **Heinz Mohren** für stete Hilfsbereitschaft und tatkräftige Unterstützung in allen technischen Angelegenheiten.

der gesamten **Arbeitsgruppe Dünne Schichten**.

den zahlreichen **Professoren, wissenschaftlichen Mitarbeitern und Doktoranden am Fachbereich Material- und Geowissenschaften**, welche unterstützend durch Rat, Tat und Diskussion zu dieser Arbeit beigetragen haben, aber auch für das freundschaftliche und aufgeschlossene Arbeitsklima.

der **mechanischen und elektronischen Werkstatt** des Fachbereichs Materialwissenschaft für tatkräftigste Unterstützung in allen an sie herangetragenen Aufgabenstellungen.

allen **Mitarbeitern des IHP**, Frankfurt (Oder), für Ihre tatkräftige Unterstützung in vielen Bereichen.

Herrn **Hanns Stoffregen** und dem **Fachgebiet PTW** am Fachbereich Maschinenbau für die erfolgreiche und sehr angenehme Zusammenarbeit auf Gebieten jenseits von Dielektrika und dünnen Schichten.

meiner gesamten **elterlichen Familie**, ohne ihre bedingungslose und tatkräftige Unterstützung nach Möglichkeiten in allen Bereichen wäre es nicht möglich gewesen, die Fülle aller Projekte der letzten Jahre zu bewältigen.

meinem Sohn **Matti Erwin** für Momente der Zerstreuung und grenzenloser Freude.

und schlussendlich **meiner Frau Sandra Hildebrandt** für die schöne gemeinsame Zeit fernab der Universität. Wir haben in den letzten zehn Jahren gemeinsam viel erlebt, erreicht und durchstehen müssen, gerade im Jahre 2012. Hoffentlich stehen uns in Zukunft weiterhin gesunde, glückliche und gemeinsame Jahre in ruhigerem Fahrwasser bevor.

Eidesstattliche Erklärung

Hiermit versichere ich an Eides statt, dass ich die vorliegende Dissertation selbstständig und nur mit den angegebenen Hilfsmitteln angefertigt habe.

Darmstadt, im Dezember 2012

Erwin M. Hildebrandt

Curriculum Vitae

Erwin Matti Hildebrandt, born 05th of October 1981 in Darmstadt, Germany. A married man, one child.

School teaching

08-88 – 06-92	Primary school Friedrich-Ebert-Schule, Darmstadt, Germany
08-92 – 06-01	Secondary school Georg-Büchner-Schule, Darmstadt, Germany Examination “Abitur”

University study

10-02 – 01-08	Study of materials science at TU Darmstadt, Darmstadt, Germany Engineering diploma in materials science Title of the Diploma Thesis: “*Investigation of Oxygen Deficiency and Ferromagnetism in Hafnium Oxide Thin Films grown by Reactive MBE*”
01-08 – 09-08	Scholarship from Graduiertenkollegs GRK 1037 „Tunable Integrated Components in Microwave Technology and Optics” Research area: dielectric thin films
10-08 – 02-13	Doctoral thesis at Advanced Thin Film Technology (ATFT), Institute of Materials Science, TU Darmstadt. Supervisor: Prof. Lambert Alff Title of Doctoral Thesis: “*Oxygen Engineered Hafnium Oxide Thin Films grown by Reactive Molecular Beam Epitaxy*”
02-13	Postdoc at Advanced Thin Film Technology (ATFT), Institute of Materials Science, TU Darmstadt. Supervisor: Prof. Lambert Alff.

List of acronyms

2-DEG	two-dimensional electron gas
AAS	atomic absorption spectroscopy
ADOMBE	advanced oxide molecular beam epitaxy
AES	auger electron spectroscopy
AFM	atomic force microscopy
ALD	atomic layer deposition
amu	atomic mass unit
ARPES	angular-resolved photoemission spectroscopy
CAD	computer-aided design
CCD	charge-coupled device
CMOS	complementary oxide semiconductor
CVD	chemical vapour deposition
DFT	density functional theory
DMS	dilute magnetic semiconductors
e-beam	electron beam
e.g.	*exempli gratia*
EDX	energy dispersive X-ray
EIES	electron impact emission spectroscopy
emu	electromagnetic unit
EOT	equivalent oxide thickness
Eq.	equation
et al.	*et alii*
FET	field effect transistor
Fig.	Figure
FWHM	full width at half maximum
GXRR	gracing incidence X-ray reflectivity
HRTEM	high-resolution transmission electron microscopy
ICDD	International Centre of Diffraction Data
ITRS	International Roadmap for Semiconductors
LDA	low density approximation
LN_2	liquid nitrogen
MBE	molecular beam epitaxy
MFC	mass flow controller
MIM	metal-insulator-metal
MOCVD	metal-organic chemical vapour deposition
MOMBE	metal organic molecular beam epitaxy
MOSFET	metal oxide semiconductor field effect transistor
MPMS	magnetic property measurement system
NVM	non-volatile memories
PID	proportional-integral-derivative
PLD	pulsed laser deposition
QCM	quartz crystal microbalance
QHE	quantum hall effect
RBS	Rutherford backscattering spectroscopy
rf-power	radio frequency-power
RGA	residual gas analyser
RHEED	reflection high energy electron diffraction
RMBE	reactive molecular beam epitaxy
RRAM	resistive random access memories
RSO	reciprocating sample option
sccm	standard cubic centimetres per second
SIMS	secondary ion mass spectrometry
SQUID	superconducting quantum interference device
STO	strontium titanate
TDDFT	time dependent density functional theory
TEM	transmission electron microscopy
UHV	ultra-high vacuum
XPS	X-ray photoelectron spectroscopy
XRR	X-ray reflectivity
YSZ	yttria stabilised zirconia

Preface

The role of oxygen vacancies in oxide thin films becomes more and more important, as most known functionalities of oxide films are more or less dependent on oxygen stoichiometry. Commonly used deposition techniques do not allow for exact and reproducible control of the oxygen content in oxide thin films, thus there is no reliable control of oxygen deficiency other than full oxidation to stoichiometry. In contrast, reactive molecular beam epitaxy offers a unique oxide thin film deposition tool allowing for reproducibly grow oxide thin films with defined oxygen content. More than that, RMBE allows tuning the oxygen content in those films, which in turn allows selective manipulation of thin film functionalities. Oxygen engineering of thin film functionalities is the key to tailor physical properties according to specific needs and demands, as an example, tuning of the band gap of a dielectric material could help to solve the challenge of proper band offsets and band alignment when bringing the dielectric in contact with new electrode materials.

This study applies RMBE to grow thin films of hafnium oxide, a widely studied material which has found its way into commercialisation as a replacement of SiO_2 in a field effect transistor. After investigating different substrates and probing various deposition conditions, RMBE-grown films of hafnium oxide yielded to epitaxial films of hafnia on *c*-cut sapphire. Having the ability to grow high-quality thin films of hafnium oxide allows studying the influence of defined oxygen deficiency on its physical properties, as the next step of this work. The optical properties changed dramatically from colourless and transparent for stoichiometric HfO_2 to dark black and opaque for highly deficient films of HfO_{2-x}. The optical band gap could be tuned within more than one eV, visualising the introduction of defects (oxygen vacancies) *in situ* during growth. In fact, Hafnia showed a metal to insulator transition as a function of the oxygen content, conductive HfO_{2-x} exhibited electrical *p*-type conductivity with resistivities of 300 $\mu\Omega$cm, charge carrier concentrations of 6 times 10^{21} cm^{-3} at mobilities of 2 $cm^2/(Vs)$. The observed conductivity seems to be intrinsic to oxygen deficient hafnia and not due to a percolation of a conducting phase in an insulating matrix, as evident from various characterisations. A simple defect band structure model has been developed based on the observations, covering the formation of defect bands within the band gap being responsible for electrical conductivity and absorption of radiation within the visible range. With respect to reports on high-T_c ferromagnetism, no evidence for d^0-ferromagnetism and room temperature ferromagnetism in Ni-doped HfO_{2-x} could be found.

List of publications and conference contributions

Publications

E. Hildebrandt, J. Kurian, J. Zimmermann, A. Fleissner, H. von Seggern, and L. Alff
“Hafnium Oxide Thin Films: Effect of Growth Parameters on Oxygen and Hafnium Vacancies”
J. Vac. Sci. Technol. B **27**, 325-328 (2009).

R. M. Öksüzoğlu, M. Yildirim, H. Çinar, **E. Hildebrandt**, and L. Alff
“Effect of Ta buffer and NiFe seedlayers on pulsed-DC magnetron sputtered Ir20Mn80/Co90Fe10 exchange bias”
J. Magn. Magn. Mater. **323**, 1827–1834 (2011).

E. Hildebrandt, J. Kurian, M. M. Müller, T. Schroeder, H.-J. Kleebe, and L. Alff
“Controlled oxygen vacancy induced p-type conductivity in HfO_{2-x} *thin films”*
Appl. Phys. Lett. **99**, 112902 (2011).

A. Senyshyn, **E. Hildebrandt**, R. Mole, D. Mikhailova, and B. Schwarz
“Magnetic Ordering in $Co_{10}Ge_3O_{16}$*”*
Diffus. Defect Data B, Solid State Phenom. **170**, 360 (2011).

M. Kayhan, **E. Hildebrandt**, M. Frotscher, A. Senyshyn, K. Hofmann, L. Alff, and B. Albert
“Neutron diffraction and observation of superconductivity for tungsten borides, WB and W_2B_4*”*
Solid State Sci. **14**, 1656-1659 (2012)

E. Hildebrandt, J. Kurian, and L. Alff
“Physical properties and band structure of reactive molecular beam epitaxy grown oxygen engineered $HfO_{2\pm x}$*”*
J. Appl. Phys. **112**, 114112 (2012)

I. Uhlmann, D. Hawelka, **E. Hildebrandt**, J. Pradella, and J. Rödel
“Structure and mechanical properties of silica doped zirconia thin films”
Thin Solid Films, **527**, 200 (2013)

Conference contributions

E. Hildebrandt, J. Kurian, and L. Alff
“Growth of HfO_x Thin Films by Reactive Molecular Beam Epitaxy”
DPG-Spring Meeting 2008, Berlin, Germany, 25. – 29. February 2008.

E. Hildebrandt, J. Kurian, Y. Krockenberger, A. Suter, F. Wilhelm, A. Rogalev, and L. Alff
“Investigation of Ferromagnetism in Oxygen Deficient Hafnium Oxide Thin Films”
DPG-Spring Meeting 2008, Berlin, Germany, 25. – 29. February 2008.

E. Hildebrandt, J. Kurian, and L. Alff
“Hafnium Oxide Thin Films: Effect of Growth Parameters on Oxygen and Hafnium Vacancies”
15th Workshop on Dielectrics in Microelectronics, Bad Saarow, Germany, 23. – 25. June 2008.

E. Hildebrandt, J. Kurian, H.-J. Kleebe, and L. Alff
“Growth of Conductive HfO_{2-x} Thin Films by Reactive Molecular Beam Epitaxy ”
DPG-Spring Meeting 2009, Dresden, Germany, 22. – 27. March 2009.

M. Baghaie-Yazdi, J. Kurian, E. Ionescu, **E. Hildebrandt**, and L. Alff
“Epitaxial Growth of Magnetite Thin Films for Spintronics ”
DPG-Spring Meeting 2009, Dresden, Germany, 22. – 27. March 2009.

R. M. Öksüzoğlu, M. Yildirim, H. Cinar, **E. Hildebrandt**, L. W. Alff, and H. Fuess
“Magnetic Interactions in Pulsed-DC Sputtered Specular Bottom Spin Valve with Cu-Oxide spacers”
11th International Conference on Advanced Materials, Rio de Janeiro, Brazil, 20. – 25. September 2009.

E. Hildebrandt, J. Kurian, and L. Alff
“Oxygen Engineering of Hafnium Oxide Thin Films by Advanced Oxide MBE”
5th NTT-BRL school, Tokyo, Japan, 24. – 27. November 2009.

E. Hildebrandt, J. Kurian, P. Zaumseil T. Schröder, and L. Alff
"Oxygen Engineering of HfO_{2-x} Thin Films grown by Reactive Molecular Beam Epitaxy"
DPG-Spring Meeting 2010, Regensburg, Germany, 21. – 26. March 2010.

M. Yildirim, H. Cinar, **E. Hildebrandt**, and R. M. Öksüzoğlu
"Influence of seed and under layer thickness on interface structure and magnetic properties in Pulsed-DC Magnetron Sputter deposited IrMn based exchange bias multilayers"
4th Seeheim Conference on Magnetism, Frankfurt, Germany, 28.03. – 01.04. 2010.

R. M. Öksüzoğlu, M. Yildirim, H. Cinar, **E. Hildebrandt**, and U. Sarac
"Correlation between residual stress, structure and magnetic properties in Pulsed-DC Magnetron Sputter deposited IrMn based exchange bias Spin Valves"
4th Seeheim Conference on Magnetism, Frankfurt, Germany, 28.03. – 01.04. 2010.

E. Hildebrandt, J. Kurian, and L. Alff
"Magnetic Properties of Hafnium Oxide Thin Films Deposited by Reactive Molecular Beam Epitaxy (RMBE)"
10th Expert Evaluation & Control of Compound Semiconductor Materials & Technologies (Exmatec), Darmstadt/Seeheim, Germany, 19. – 21. May 2010.

E. Hildebrandt, J. Kurian, I. Costina, T. Schroeder, and L. Alff
"Oxygen Engineering of Hafnium Oxide Thin Films Grown by Reactive Molecular Beam Epitaxy (RMBE)"
16th Workshop on Dielectrics in Microelectronics, Bratislava, Slovakia, 28. – 30. June 2010.

E. Hildebrandt, J. Kurian, and L. Alff
"Oxygen Engineering of Hafnium Oxide Thin Films by Advanced Oxide MBE"
16th International Conference on Molecular Beam Epitaxy, Berlin, Germany, 22. – 27. August 2010.

Erwin Hildebrandt, Jose Kurian, Thomas Schröder, and Lambert Alff
"*p*-type Conductivity in Oxygen Deficient HfO_2 Thin films"
Deutscher MBE-Workshop, Berlin, Germany, 05. – 06. Oktober 2011.

Erwin Hildebrandt, Jose Kurian, Mathis M. Müller, Thomas Schroeder, Hans-Joachim Kleebe, and Lambert Alff
"*p*-type conductivity in oxygen deficient HfO_{2-x} thin films grown by Reactive Molecular Beam Epitaxy"
DPG-Spring Meeting 2012, Berlin, Germany, 26. – 30. March 2012.

E. Hildebrandt, J. Kurian, M. M. Müller, H.-J. Kleebe, T. Schroeder, and L. Alff
"Oxygen vacancy induced *p*-type conductivity in HfO_{2-x} thin films grown by Reactive Molecular Beam Epitaxy"
17th Workshop on Dielectrics in Microelectronics, Dresden, Germany, 25. – 27. June 2012.

E. Hildebrandt, J. Kurian, M. M. Müller, T. Schroeder, H.-J. Kleebe, and L. Alff
"Oxygen defect induced *p*-type conductivity in hafnia"
EMRS 2012 Fall Meeting, Warsaw, Poland, 17 – 21. September 2012.

E. Hildebrandt, J. Kurian, M.M. Müller, H.-J. Kleebe, and L. Alff
"Oxygen defect induced *p*-type conductivity in HfO_{2-x} thin films"
Workshop on Oxide Electronics 19, Apeldoorn, Netherlands, 30.09. – 03.10 2012.

Index

1 Introduction

The class of oxides has a unique variety of very simple and highly complex materials among all existing matter. Oxide materials exhibit an extensive variety of physical and chemical functionalities, covering, e.g., ferroelectricity, pyroelectricity, piezoelectricity, paramagnetism, ferromagnetism, antiferromagnetism, superconductivity, magnetoresistivity, birefringence, optical nonlinearity, semiconductivity, non-conductivity, metallicity, and several acoustic properties. Many of these properties are exploited in numerous applications, such as semiconducting thin film devices, actuators, sensors, coatings, storage devices, optical devices; just to name a few. When having a closer look at the physical origin of the mentioned functionalities, it is remarkable that many of them are based on comparable or similar chemistry and crystal structure, principally offering the combination of different functionalities in one single material. This upgrades the class of oxides to a real multifunctional platform, allowing selectively developing and designing novel oxide materials for new emerging demands. When it comes to the transformation from bulk solids to thin films, the range of functionality broadens even more, as some physical phenomena are evoked only in the case of thin films grown in a highly ordered manner on selected substrates.

Molecular beam epitaxy in general is the method of choice to fabricate highly ordered, epitaxial thin films of nearly any material, if possible. As an enabling technology it has paved the way for many key applications based on thin films, especially the success of past Si-based semiconductor industry is owed to the development of MBE. Later, during intensive research activities in the field of high-T_c superconductors, the classical MBE has been modified to oxide MBE by adding the possibility of introducing a reactant (oxygen) during growth. Today, oxide MBE supports among others further development of novel high-T_c superconductors, ferroelectrics, dielectrics, as well as magnetic thin films for data storage. Although there are outstanding examples of oxide MBE thin film growth in various thin film systems, there is still a lot to be done in oxide MBE to reach same level of reproducibility and perfection as known for classical semiconductor MBE.

The development of complex oxide thin films has been fostered by the advancement of MBE to oxide MBE, merging the capabilities of classical MBE with *in situ* oxidation and control of oxygen content in thin film oxides. This allows growing well-ordered thin films with defined interfaces, epitaxially strained on single crystal substrates with stoichiometric control. As the oxygen content in thin films is governed by thermodynamics, the representable oxygen off-stoichiometry in thin films is very limited for classical deposition methods, whereas oxide MBE allows stabilising films with a stoichiometry beyond thermodynamic equilibrium. As proven for numerous binary and ternary oxide systems, the control of oxygen stoichiometry, thus the control of oxygen vacancies, allows manipulating physical properties of oxide thin films, since most of them are more or less dependent on the oxygen content. Due to its high level of controllability, oxide MBE allows to tune these physical properties, which in turn allows exploiting them for novel thin film devices and applications. To put it in a nutshell, oxygen engineering of simple and complex oxides by oxide MBE could be a key to novel combinatory functionalities, fostering the continuous development of new break-through thin film devices.

1.1 Development of oxide MBE

From 1977 to 1979 the growth of aluminium oxides on AlGaAs/GaAs substrates by molecular beam epitaxy has been reported by Ploog *et al.*, which are among the first reports in literature of MBE growth of thin films based on single element evaporation.[1, 2] Their deposition chamber was equipped with several effusion cells for elemental evaporation, *in situ* RHEED for growth monitoring, a quadrupole mass spectrometer, and a high capacity (at least during those days) turbo molecular pump. Molecular oxygen has been introduced by means of a simple stainless-steel tube pointing to the substrate. Already in that state, oxide thin films could be grown with fair control of stoichiometry, but the demand for the development of more efficient and controllable oxygen sources fostered further development of oxide MBE. In 1982, Stall was first to grow ternary oxides of Al_2MgO_4 by MBE using oxidation agents instead of molecular oxygen.[3] The evaporation of As_2O_3 and Sb_2O_3 via effusion cells leads to the decomposition of these metal oxides, providing oxygen for thin film growth, whereas the amount of oxygen released due to decomposition is controlled by the effusion cell temperature. The advantage is a significantly lower deposition chamber pressure, as no gaseous reactant has to be introduced. Until then, most of the grown films were of polycrystalline to amorphous nature. In the same year, Maloney succeeded in the growth of homoepitaxial, single crystalline silicon oxide on silicon wafers with unintended oxygen deficiency.[4] As oxidation agent molecular oxygen backfilled in the deposition chamber was used. Two years later, Betts and Pitt succeeded in the growth of probably the first multifunctional oxide thin film by MBE, which was lithium niobate on single crystalline $LiNbO_3$ and a-cut sapphire substrates, as it combines ferroelectric, pyroelectric, piezoelectric, acoustic, and nonlinear optical properties in one material.[5]

After oxidation has been established with molecular oxygen via gas inlets, chamber backfilling with oxygen, and utilising oxygen from the decomposition of unstable oxide materials, extensive research activities on the field of high-T_c superconductors starting in the late 80ies up to the late 90ies led to the introduction of ozone as an oxidation agent in MBE thin film growth. Hosokawa and Ichimura introduced a method to thermally control the generation and evaporation of ozone, which was fed into the deposition chamber. This system has been called 'ozone jet generator'.[6] Ozone possesses much higher oxidation power in comparison to molecular oxygen, thus allowing reducing the amount of gaseous species to be introduced into the growth chamber during deposition, while maintaining the same oxidation power. A decrease in background pressure during growth fosters better film formation with higher crystallinity at lower substrate temperatures. Besides molecular oxygen and ozone, radical oxygen is nowadays a widely used alternative oxidation agent for thin film growth. Starting in 1999, thin films of ZnO have been grown with radical oxygen, as it provides stronger oxidation than molecular oxygen, much lower gas flow rates, and high controllability.[7] In comparison to ozone, which is difficult to handle, the generation of low-energy oxygen atoms (radicals) is much easier and less dangerous, as just the amount of radicals needed for oxidation (usually a few sccm) is created.

The development of MBE to oxide MBE was not limited to the controlled introduction of gaseous reactants into the deposition chamber during growth, but also involved the development of new evaporation techniques and oxygen-resistant evaporation sources. As an example, the development of the titanium source Ti-Ball^{TM} (ref. [8]), offering superior rate stability under relatively high oxygen partial pressure, advanced the efficient growth of Ti-based oxides, such as lead titanate, barium titanate, strontium titanate, etc.[9] The combination of PLD, denoting to the ablation and transfer of target material to the substrate by striking the target with high energy laser pulses, with extreme low growth pressures led to the term 'laser MBE', although the growth techniques MBE and PLD are different.[10, 11] Nevertheless, the combination of MBE with *in situ* characterisation tools which go beyond RHEED, e.g., with AFM, XPS, angular-resolved photoemission spectroscopy (ARPES), and AAS in integrated cluster systems allows for much more comprehensive analysis of physical thin film properties. In the case of the quantum hall effect, MBE has played an important role in the development of high-mobility samples and two-dimensional electron gases.[12] Only the continuous improvement of the vacuum quality by the introduction of ultra-high vacuum cryopumping, and since 1998 the SI-modulation-doping from both sides of a quantum well have made such developments possible.[13]

The achieved and still continuing technical developments of (oxide) MBE allows us today to grow complex oxide thin film, however, there is still a demand for further improvements, especially when it comes to the precise determination of thin film oxygen stoichiometry. This is of special importance, as already minor changes in stoichiometry do have significant impact on film properties. Muller *et al*. applied annular-dark-field microscopy and core-level electron spectroscopy to visualise oxygen deficiency in $SrTiO_{3-\delta}$ thin films on an atomic scale, as detailed as known only for high-resolution transmission microscopy of crystal structures.[14] Although their results look promising, this method is sometimes seen critically and cannot be transferred easily to other oxide thin film systems, especially when it comes to lower film quality. In comparison, Jia *et al*. have performed atomic-resolution measurements of oxygen concentration in twin boundaries of $BaTiO_3$ utilising high-resolution imaging at negative spherical aberration of the objective lens in an aberration-corrected transmission electron microscope.[15] Although there are a few examples for monitoring oxygen content in thin films, the absolute and exact determination of oxygen content (oxygen vacancies) in oxide thin films remains to be challenging, as relevant oxygen vacancy physics plays a role at vacancy concentrations sometimes below one atom per cent, which none of the known spectroscopic tools is able to resolve properly. Additionally, to describe oxygen deficiency attributed physical phenomena in oxygen deficient thin films it is vital to know, whether oxygen vacancies are distributed homogeneously in the film, or whether they are accumulated either at the interface or film surface. The fact that a lot of oxide thin films are grown on substrates which are oxides themselves hardens the task of exact oxygen content determination without substrate contribution. These aspects visualise one of today's dilemmas in oxide thin film growth, as on the one hand the capabilities of oxide MBE allow a precise and reproducible growth of oxygen deficient thin films, but on the other hand there is a lack of proper spectroscopic and especially spectrometric characterisation tools for precise, depth-resolved oxygen (vacancy) determination in thin films.

The combination of single element evaporation, *in situ* oxidation, and precise rate controllability is the key to fabricate oxide thin films of high quality in a reproducible fashion. As there are no standardised and commercially available oxide MBE systems on the market, the growth of oxide thin films by oxide MBE usually goes hand in hand with the development of oxide MBE equipment. Figure 1.1 shows the scheme of an advanced oxide molecular beam epitaxy unit developed during the last five years at TU Darmstadt in collaboration with MPI Stuttgart. It combines elemental evaporation via electron beam and effusion cells,

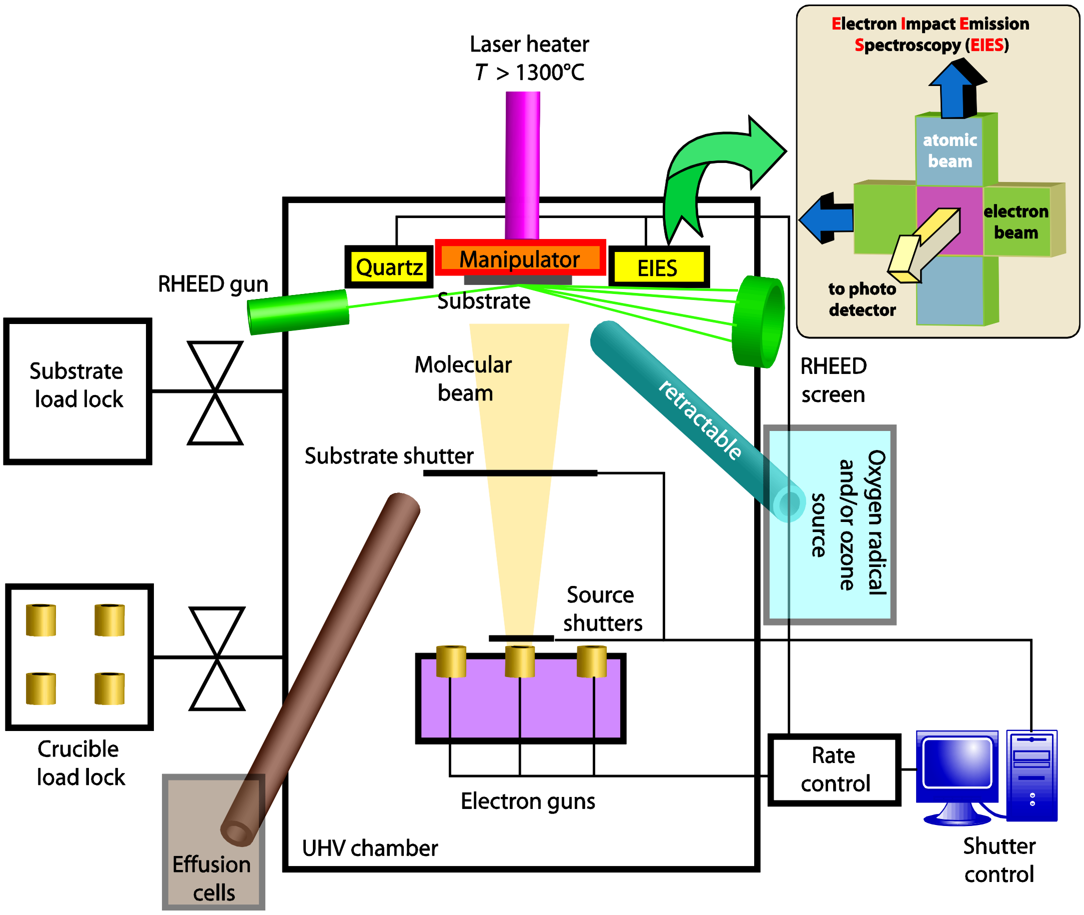

Fig. 1.1: Schematic of the advanced oxide molecular beam epitaxy unit developed within the last five years as a collaborative work between TU Darmstadt and MPI Stuttgart.

state-of-the-art rate monitoring (QCM and EIES), *in situ* growth monitoring (RHEED), and in situ oxidation via activated oxygen (O*) or ozone (O_3) . Features like a separate crucible storage chamber, *in situ* exchange of samples, crucibles & quartz crystals, a laser heater for substrate temperatures above 1,300 °C, and the integration of the deposition unit in an integrated deposition cluster together with PLD outlines the unique capabilities of this in-house developed ADOMBE.

1.2 Milestones of thin film engineering by oxide MBE

During the last decade, selected examples of epitaxial growth of oxide thin films on oxide substrates by oxide MBE demonstrate that oxide MBE is about to reach the stage of GaAs epitaxy grown by classical MBE in terms of film quality. As an example, Schlom *et al*. deposited layered oxide heterostructures and superlattices of dielectric and ferroelectric oxides, such as SrO, $SrTiO_3$, $BaTiO_3$, $PbTiO_3$, and $Bi_4Ti_{13}O_{12}$, by nano-engineering of those oxides.[16] This was accomplished by supplying the single compounds in the desired layering sequence with submonolayer composition control.[16] It is vital to have precise compositional control during growth in order to fabricate thin films with monolayer accuracy. There are two different approaches to grow stoichiometric monolayers, (i) via adsorption controlled growth, and (ii) via RHEED-based composition control. In practice, the first method is based on the finite adsorption of single components and desorption of excess other elements at the same time, so film composition could be controlled by controlling the atomic flux of only one source, whereas the other sources can be operated within a comparable broad growth window. The second (RHEED-based) approach allows controlling film composition by obtaining non-classical RHEED oscillations, as fractional coverage results in a modulation of the RHEED intensity oscillation envelope, so film composition could be controlled within an accuracy of 1%.[17] This method has been developed for epitaxial growth of GaAs and AlGaAs much earlier in 1988 by Horikoshi *et al.*, but is still the method of choice for thin film growth today.[18] However, in the case of oxides, very often epitaxial films are formed without the observation of RHEED oscillations.

The growth of separate, single layers of thin film oxides on an atomic scale with no interfacial layer helped to trace down the origin of many physical phenomena. Logvenov *et al.* demonstrated that copper oxide-based superconductors show high-T_c superconductivity at film thicknesses down to one single monolayer.[19] They used MBE to deposit bilayers of $La_{1.65}Sr_{0.45}CuO_4$ and La_2CuO_4 with each layer just three unit cells thick, doped with Zn atoms as markers to suppress superconductivity in selected layers.

Superior control of compositional stoichiometry has been demonstrated for the epitaxial growth of the first five members of the Ruddlesden-Popper homologous series of $Sr_{n+1}Ti_nO_{3n+1}$ on single crystalline strontium titanate substrates with shuttered MBE by Haeni *et al.*[20] However, *in situ* oxidation was achieved by means of simple molecular oxygen, backfilled into the growth chamber. The Ruddlesden-Popper homologous series is a perfect example for the necessity of strict composition control, as already small deviations from stoichiometry lead to the stabilisation of $SrTiO_3$ ($n = \infty$). In the case of $SrTiO_3$, compositional control includes precise control of the oxygen content, as stoichiometric $SrTiO_3$ is an insulating, transparent material, whereas $SrTiO_{3-x}$ exhibits electrical conductivity, and shows a reduced transparency due to absorption.[21, 22] Another good example for multifunctional oxide thin films is the combination of ferromagnetic and ferroelectric ordering in materials, so-called ‘magnetoelectric multiferroics’, opening up entirely new fields of application in microelectronics, as the magnetic properties of such materials could be controlled by applying an electrical field or vice versa. Bismuth ferrite ($BiFeO_3$) is among the prominent magnetoelectric multiferroic candidates, which needs to be grown epitaxially with high crystal perfection and perfect oxygen stoichiometry, necessary for device structures of $BiFeO_3$ exhibiting superior device performance.[23]

Coming from oxide-on-oxide systems to oxide-on-semiconductor (oxide-Si) systems, the growth of complex oxides other than that of SiO_2 on silicon substrates, free of interfacial layer formation, has been demonstrated by McKee *et al.* in 1998.[24] They have grown a few monolayers of STO on silicon wafers, resulting in an equivalent oxide thickness of less than 10 Å. In those days STO was considered as a possible candidate to replace SiO_2 as a gate dielectric in field effect transistors, as the dielectric permittivity of STO can exceed values of 10,000 in comparison to 4 known for SiO_2. The growth of STO on Si points out a major break-through on the way to today’s state-of-the-art microelectronics based on HfO_2, however, STO has proven not to be the material of choice to replace SiO_2 as a gate dielectric.

Recently, Son *et al.* succeeded in the homoepitaxial growth of La-doped $SrTiO_3$ (STO) on STO substrates and heteroepitaxial growth of STO on $(LaAlO_3)_{0.3}(Sr_2AlTaO_6)_{0.7}$ (LSAT), resulting in electron-doped STO with mobilities of 30,000 cm^2/Vs exceeding those known for single crystals.[25] To grow STO films with such high mobility, they have developed a so-called ‘hybrid molecular beam epitaxy’ approach, which combines strontium evaporation from effusion cells, oxidation from rf-activated oxygen (oxygen radicals), and the evaporation of titanium via a metal-organic source (titanium tetra isopropoxide).[26] Electron doping of STO is a textbook example for the advantages of oxide MBE as a low energy thin film growth technique compared to high energy deposition methods. In contrast to MBE-grown films, PLD-deposited heterostructures of Nb-doped STO/undoped STO on STO substrates yield to lower mobilities than observed for single crystals.[27] The observed conductivity in STO with charge carrier mobilities of 30,000 cm²/Vs is a strong function of the doping concentration in the material. Hence, a deposition tool (oxide MBE) is needed which is capable of controlling the dopant/defect concentrations in oxide thin films with high accuracy.

Besides advances in oxide electronics, oxide MBE has also fostered further discovery of novel high-T_c superconductors based on cuprates. Exemplarily, the synthesis of single phase and metastable *T'* (La, Ce)$_2$CuO$_4$ (LCCO; *T'* denotes to 't-prime') thin films and infinite-layers of $Sr_{1-x}La_xCuO_2$ on $DyScO_3$ substrates led to a T_c^{end} of 30 K and 41 K, respectively, which are known to be highest in the *T'* family.[28, 29] For the growth of *T'* structures, reactive MBE offers precise rate control, high & controllable oxidation conditions, and UHV conditions, allowing to reduce the growth temperatures below 700 °C, which is the key to stabilise thin films of LCCO in *T'* structure.

Today, oxide MBE is a versatile deposition technique serving to grow simple and complex oxide thin films of nearly any kind. However, there is still a demand for further development of oxide MBE on the way to comparable perfection known for non-oxide semiconductors grown by classical MBE. As thin film research of oxides is still in its infancy compared to the research on bulk compounds, there are still numerous materials already studied in bulk which could be investigated in their thin film morphology. Many compounds are known and already studied in bulk for decades, all their properties seemed to be discovered, characterised, and exploited. This assumption can be a fatal error, as demonstrated for MgB_2, a material discovered in 1954 by Jones *et al.*,[30] which was reported by Nagamatsu *et al.* to be superconducting with a T_c of 39 K nearly half a century later in 2001, the highest T_c known at that time for non-cuprate superconductors.[31] This example clearly demonstrates that there are still important discoveries to be made even for well-studied, binary compounds. This becomes even more prominent as (i) there are lots of materials and compounds showing certain physical phenomena only in thin film form, and (ii) the flexibility in varying materials composition and stabilising metastable phases away from thermodynamic equilibrium in thin films is much higher than for conventional bulk synthesis techniques. Additionally it has been shown that interface engineering, the substitution of specific elements by others (doping), and engineering the oxygen content could evoke new functionalities in oxide thin films, which are only accessible by oxide MBE. The focus of classical MBE on defect-freeness and maximum perfection in film stoichiometry has moved for oxide MBE to purposefully introducing defects in a highly controlled and reproducible manner (defect engineering). This leads consequently to the point that even seemingly simple binary oxide thin films, which are well-studied and commercialised within billion dollar markets, might still exhibit new physical properties and possible (multi)functionalities beyond stoichiometry, which are only accessible with oxide MBE. The potential of functionality tailoring by defect engineering with oxide MBE is demonstrated in this study taking the high-κ dielectric hafnium dioxide as an example, which is introduced in detail in the following chapters.

1.3 Hafnium oxide

The motivation for investigating hafnium oxide thin films by oxide MBE (reactive MBE), a principally well-studied and already commercially exploited thin film material, was manifold. At first, controversially discussed reports on room temperature ferromagnetism, which is attributed to the formation of oxygen defects, has called our attention on hafnium oxide (see chapter 1.3.3). Via classical theory it is not possible to explain oxygen vacancy-induced room temperature ferromagnetism in undoped, closed shell configured insulating oxides, exhibiting Curie temperatures above 350 K. However, it seems to be accepted that oxygen vacancies are responsible or at least influence the observed phenomenon. As there is no other thin film deposition tool as oxide MBE which allows controllably growing thin films with defined oxygen deficiency in a reproducible way within a wide range, this was our main motivation to step into the field of dielectrics with hafnium oxide. First, to our knowledge there are no reports on precise and reproducible control of oxygen content in HfO_{2-x}, as hafnium (in contrast to, e.g., titanium or cerium) is extremely stable in its valence 4+ and very unlikely to form stable deficient phases of hafnia. Second, as already illustrated for various oxide materials and compounds, oxygen content (oxygen vacancies) seems to influence most physical properties and functionalities and possibly evoke new, unexpected physical phenomena also in HfO_{2-x}. After our very first experiments on HfO_{2-x} thin films grown by RMBE, results have indicated that the controlled introduction of oxygen vacancies manipulates optical and electrical properties of hafnia in an unexpected way. Besides the interest in the discovery of new functionalities of hafnium oxide due to defect engineering, the extensive commercial application of HfO_2 in microelectronics could ease up the later utilisation and exploitation of such functionalities in novel devices.

The following chapters shed light on hafnium oxide, starting from very basic physical and chemical properties, describing commonly utilised thin film deposition methods for hafnia, highlighting selected physical properties, as well as giving an introduction to the state-of-the-art of relevant commercial applications of hafnium oxide thin films.

1.3.1 Chemical and physical properties

Hafnium oxide (Hafnia) is a hard, transparent, and insulating material with a dielectric constant of 25 in the case of m-HfO_2, and having a wide band gap of around 5.7 eV for stoichiometric, bulk HfO_2.[32-35] Reported values for the band gap of HfO_2 thin films differ between 5 eV and 6 eV, depending on the utilised deposition method, substrate type, and the resulting polymorphs of HfO_2 thin films.[36, 37] Besides the slight variations of the optical band gap and the description of band characteristics of HfO_2 reported in literature, the model of a direct band gap seems to be mostly accepted, although there are reports indicating indirect transitions close in energy to direct transitions.[36, 37] The ions in hafnium oxide have homologous outer shell configurations, Hf^{4+} [Xe] $4f^{14}$ and O^{2-} [Ne],[38, 39] the properties of hafnia are expected to be similar to zirconia (ZrO_2). This similarity is commonly attributed to the lanthanide contraction of Hf that is responsible for the nearly similar atomic and ionic radii of Hf and Zr as well as their similar ionisation potentials.[40] Recent density functional theory (DFT) studies confirm these similarities, but also point out differences in atomic radii and equations

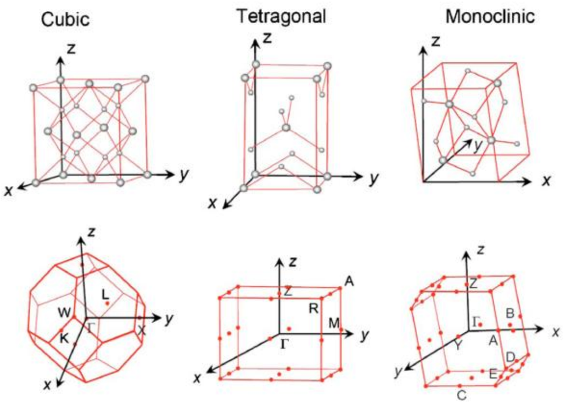

Fig. 1.2: Schematics of unit cells for three different morphologies of hafnium oxide existing at ambient pressures but different temperatures, taken from ref. [44].

of state.[41] The superior thermal stability and hardness of hafnia qualifies HfO_2 for applications as protective coatings.[35, 42]

Hafnium oxide exists in three polymorphs at atmospheric pressure; C^5_{2h} m-HfO_2 ($P2_1/c$) at low temperatures, C^{15}_{4h} t-HfO_2 ($P4_2/nmc$) at elevated temperatures above 2,000 K, and O^5_h c-HfO_2 ($Fm3m$) at temperatures above 2,870 K.[43, 44] HfO_2 undergoes phase transitions as a function of the applied external pressure at 4.3 ± 0.3, 12 ± 0.5, and 28 ± 2 GPa to denser structures following $P2_1/c$ (monoclinic) → $Pbcm$ (orthorhombic) → $Pnma$ (orthorhombic), respectively.[41, 45-47] Fig. 1.2 shows schematically the mentioned morphologies of hafnia existing at atmospheric pressure at different temperatures. As m-HfO_2 is known to be the most stable crystalline phase under ambient conditions, Fig. 1.3 illustrates the simulated structure of eight m-HfO_2 unit cells by VESTA[48], where small red dots represent oxygen atoms and big blue dots Hf atoms. (-111) crystallographic planes are inserted as grey planes for better clarity. Considering monoclinic symmetry ($a \neq b \neq c$, $\alpha = \gamma = 90°$, $\beta \neq 90°$), according to the pdf-card 00-034-0104 from the International Centre of Diffraction Data (ICDD) for m-HfO_2, m-HfO_2 lattice constants are a = 5.285 Å, b = 5.182 Å, c = 5.116 Å, β = 99.259°. Note that the values for the lattice parameters a, b, and c are very close to each other and do not differ very much for t-HfO_2, c-HfO_2, and o-HfO_2. Practically this hardens a possible determination of crystal symmetry for textured and epitaxial thin films of HfO_2, as for all different crystallographic morphologies out-of-plane reflections (observable in X-ray diffraction) are very close to each other.

1.3.2 Deposition Methods of HfO_2 thin films

A variety of deposition methods have been utilised to grow thin films of hafnium oxide, such as ALD, sputtering, PLD, CVD,[49] e-beam evaporation, high-energy ion beam assisted deposition,[50] metal organic MBE (MOMBE),[51] and sol-gel methods. All mentioned deposition methods do have unique features and therefore turned out to have certain advantages and drawbacks for the growth of HfO_2 thin films regarding its physical properties. Figure 1.4 summarises the most prominent deposition methods of hafnium oxide, naming pros, cons, and crystal structure of the resulting thin films. In the following a brief overview of selected deposition techniques for HfO_2 thin films is presented, focussing on resulting film crystallinity and stoichiometry.

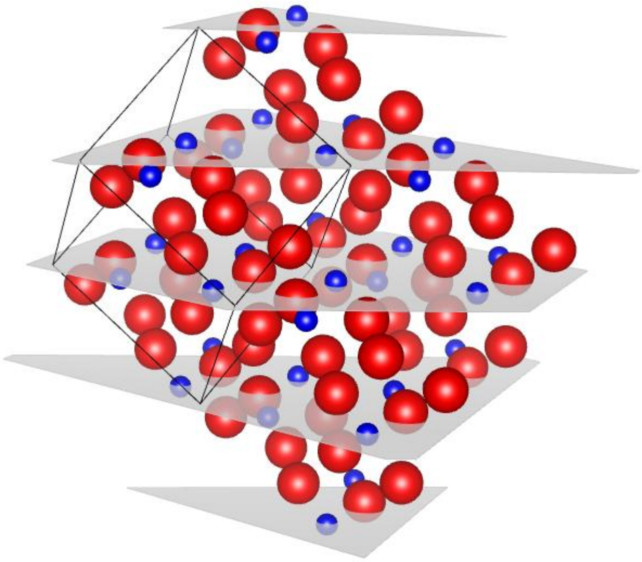

Fig. 1.3: Simulation of *m*-HfO_2 with VESTA[48]. Displayed are 8 unit cells, one unit cell is framed with black lines. Big red dots represent oxygen, small blue dots represent hafnium atoms, (-111) planes are presented in grey.

1.3.2.1 Sol-gel methods

The growth of HfO_2 thin films by sol-gel methods is based on organometallic precursors, such as hafnium tetrachloride,[52] hafnium ethoxide,[53, 54] and hafnium *n*-butoxide.[55] Advantages of thin HfO_2 films fabricated by sol-gel technique are high purity, good composition control, relatively low processing temperatures, and large deposition areas.[56, 57] Sol-gel deposited films tend to be amorphous, only after firing at 500 °C or annealing at 550 °C films crystallised in the monoclinic phase.[52, 54] No reports on the study of film stoichiometry have been found.

1.3.2.2 Sputtering

Sputtering hafnia thin films can be realised in two ways, either by rf-sputtering of a stoichiometric HfO_2 target under argon or by rf-magnetron sputtering of a metal Hf target under oxygen plasma.[58] The latter one allows for variations in stoichiometry as sputtering power and plasma intensity can be varied within a certain extend. Similar to sol-gel fabricated thin films of HfO_2, sputtered films tend to be amorphous for low growth temperatures. Film annealing leads to crystallisation in monoclinic or tetragonal symmetry of the resulting polycrystalline films at temperatures around 1,000 °C.[59] Numerous studies have been conducted on how to influence the interface formation of sputtered HfO_2 films and silicon substrates, such as the variation of gas mixture (O_2/Ar),[60] deposition voltage, and thermal annealing processes.[61]

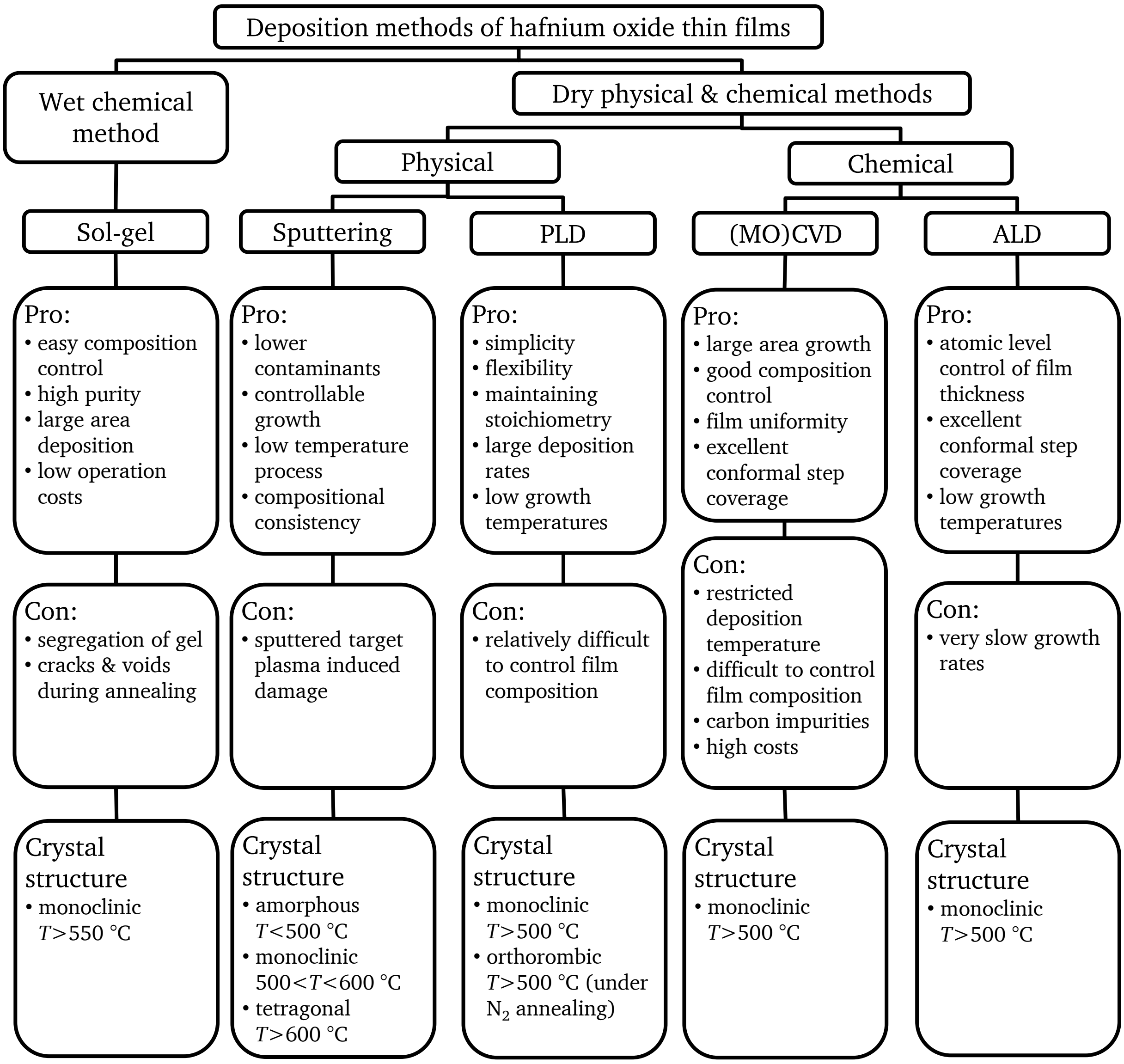

Fig. 1.4: Schematic of different deposition methods applied to grow thin films of hafnium oxide. Redrawn from ref. [73].

1.3.2.3 Pulsed laser deposition

PLD, one of the most prominent physical deposition methods, allows the deposition of thin films based on the stoichiometric transfer of material from a solid state synthesised target to a (heated) substrate by extreme short and highly energetic laser pulses.[62] Additionally, PLD allows influencing film stoichiometry by introducing reactive gases into the growth chamber during deposition, such as oxygen, nitrogen, or hydrogen. In the case of HfO_2 thin films it is possible (i) to ablate from a metal Hf target under an sufficiently high oxygen partial pressure in the deposition chamber during film growth (up to 200 mTorr),[63] and (ii) to ablate from a stoichiometric HfO_2 ceramic target.[64, 65] It is reported that deposition temperature does not influence film composition (Hf/O ratio), whereas a change in oxygen partial pressure during growth obviously affects the Hf to O ratio. Films deposited at low temperatures are amorphous, but recrystallize after thermal annealing at temperatures of minimum 500 °C.[62, 64]

Table 1: List of common precursors used for ALD of metal oxides and nitrides. Reprinted from ref. [73] with references therein.

Precursor type	Formula	Examples
Metal alkyls	MR_y	$Al(CH_3)_3$
Metal alkoxides	$M(OR)_y$	$Hf[OC(CH_3)_3]_4$
		$Hf(O\text{-}t\text{-}C_4H_9)_4$
Metal alkylamides	$M(NR_2)_y$	$Hf[N(C_2H_5)_2]_4$
		$Hf[N(CH_3)(C_2H_5)]_4$
Metal β-diketonates	$M(thd)_y$	$Hf(O_2C_5H_7)_4$
	$M(acac)_y$	
	$M(thd)_y(OR)_z$	
Metal halides	MX_y	$HfCl_4$
		WF_6
		TiI_4
Metal cyclopentadienyl	$M(C_pR_x)_y$	$Hf(C_p)_2(CH_3)_2$, $Ru(EtC_p)_2$
	$M(C_pR_x)_yR_y$	$(CpMe)_2HfMe_2$, $Cp_2Hf(OMe)_2$,
		$(CpMe)_2Hf(OMe)Me$,
		$(CpMe)_2Hf(OMe)_2$
Metal amidinates	$M(R\text{-}AMD)_y$	$La(^iPr\text{-}AMD)_3$, $La(^iPr\text{-}fAMD)_3$,
		$Ti(^iPr\text{-}MeAMD)_3$, $Ni(^iPr\text{-}MeAMD)_2$
Metal nitrates	$M(NO_3)_y$	$Hf[NO]_4$

PLD-grown films on silicon substrates have been post deposition annealed to study the reduction of the interfacial layer as a function of annealing under nitrogen atmosphere.[65, 66]

1.3.2.4 Metal-organic chemical vapour deposition

MOCVD principally offers large area deposition, good composition control, film uniformity, and good conformal step coverage on non-planar device geometries. HfO_2 thin films grown with MOCVD based on tetrakis-diethylamidohafnium showed contaminations with carbon leading to poor dielectric film properties, a very common observation for MOCVD-grown films.[67] Reducing such contaminations could be achieved by providing an additional reactive oxidant such as oxygen plasma, H_2O or O_3.[68] However, no studies concerning oxygen stoichiometry have been reported for films grown with MOCVD.

1.3.2.5 Atomic layer deposition

Probably ALD is known to be the most common fabrication technique of depositing thin films of hafnium oxide, especially when it comes to upscaling to industrial fabrication standards of state-of-the-art hafnium-based microelectronics.[69, 70] ALD is considered to be an enabling technology for most of today's semiconductor devices, due to its relative easiness and simplicity, provided that suitable precursors are available.[71] A recent review of the growth of ALD-based high-κ oxides and novel ALD developments is provided by Niinistö *et al.*[72] The technique is based on subsequent pulses of reactive precursors separated by inert gas purges to eliminate gas-phase reactions and remove volatile by-products. The first reactant is chemisorbed on a substrate until saturation (full coverage), then a second pulse introduces the second precursor reacting with the first precursor, again until saturation. Repetition of these subsequent gas pulses allows layer-by-layer film growth on large areas with high quality in a slow and well controllable fashion. Numerous precursors have been used for ALD-based hafnium oxide thin films; an overview is given in Table 1, taken from ref. [73] and references therein. In order to obtain crystalline films, post deposition annealing processes have to be applied, known as ‘rapid thermal annealing’ or ‘film activation’ in semiconductor industry. The control of oxygen content in high-quality ALD-fabricated thin films is poor, as no additional reactant like oxygen or additional oxidants can be introduced during growth, and utilised precursors provide known amounts of oxygen for film formation. However, it is possible to grow films with nearly perfect Hf to O stoichiometry (Hf : O = 1 : 2).

1.3.2.6 Molecular beam epitaxy

There are only very few reports on the growth of hafnium dioxide thin films by MBE. Yan *et al.* have grown thin films of HfO_2 on silicon substrates by e-beam evaporation of metal Hf providing an oxygen radical beam from an HD25 OAR radical source.[74] As their films were grown at substrate temperatures of 350 °C, the resulting films were of amorphous nature. Film stoichiometry was estimated from XPS and AES measurements to be HfO_2, however, no studies on the variation of the Hf to O ratio have been conducted. Lee *et al.* report on the growth of HfO_2 thin films by MBE utilising e-beam evaporation from stoichiometric HfO_2 pellets.[75] No additional oxygen has been introduced into the deposition chamber during growth. Again, films were grown on silicon substrates at room temperature exhibiting amorphous films of presumably stoichiometric HfO_2. No studies on oxygen content in hafnia have been conducted. Lehan *et al.* fabricated thin films of hafnia for optical coatings on various substrates by e-beam evaporation of small, crushed HfO_2 pellets (i) without reactant, (ii) with molecular oxygen backfilled into the deposition chamber, (iii) reactive ion beam assisted growth with 300 eV O^{2-} ions, and (iv) low energy reactive ion beam assisted growth with 50 eV O^{2-} ions.[76] The comparison of these films with RBS yielded to O/Hf ratios greater than two for films grown with oxidation agents (ii) to (iv), and ratios below two for films grown without reactant (i). This depicts the necessity to provide supplementary oxygen for the growth of stoichiometric HfO_2 thin films by e-beam-based MBE, and demonstrates the great influence of growth parameters on oxygen content. It is not possible to reproducibly grow stoichiometric films of HfO_2 by simply evaporating HfO_2 pellets in a vacuum chamber, the presence of an additional and controllable oxygen source is vital for obtaining high-quality thin films of hafnia with defined Hf to O ratio.

1.3.3 Room temperature and d^0–ferromagnetism

In 2004 reports on the observation of room temperature ferromagnetism in HfO_2 by Venkatesan *et al.* introduced an additional research topic in scientific community for the class of insulating dielectrics.[77] The combination of the physical properties film transparency, electrical insulation, wide band gap, and room temperature ferromagnetism in one material would open up new possibilities for application in spintronics, beyond classical applications in

Table 2: Dilute ferromagnetic oxide materials exhibiting high-T_c ferromagnetism. Reprinted from ref . Coey *et al.* and references therein.

Material	E_g (eV)	Doping x	Moment (μ_b)	T_c (K)
GaN	3.5	Mn-9%	0.9	940
		Cr	-	>400
AlN	4.3	Cr-7%	1.2	>600
TiO_2	3.2	V-5%	4.2	>400
		Co-1-2%	0.3	>300
		Co-7%	1.4	650-700
		Fe-2%	2.4	>300
SnO_2	3.5	Fe-9%	1.8	610
		Co-5%	7.5	650
ZnO	3.3	V-15%	0.5	>350
		Mn-2.2%	0.16	>300
		Fe-5%, Cu-1%	0.75	550
		Co-10%	2.0	280-300
		Ni-0.9%	0.06	>300
Cu_2O	2	Co-5%, Al-0.5%	0.2	>300
$In_{1.8}Sn_{0.2}O_3$	3.8	Mn-5%	0.8	>300

microelectronics, leading to a new class of materials known as dilute magnetic semiconductors (DMS).[78] Various transition metal oxides were investigated, such as zinc oxide, titanium dioxide, tin oxide, and hafnium oxide; Table 2 gives a more detailed overview on the material variety. The claim of room temperature ferromagnetism in doped and undoped wide band gap insulators has been discussed extensively, as in insulating materials spins usually tend to couple antiferromagnetically. However, there is lots of scepticism in the wider magnetism community regarding the origin of the observed high-T_c ferromagnetism. 2005 Coey *et al.* proposed a model for ferromagnetic exchange mediated by shallow donor electrons that form bound magnetic polarons, which overlap to create a spin-split impurity band.[79] The effect of room temperature ferromagnetism with high Curie temperatures is not limited to DMS from Table 2, but has also been demonstrated for undoped systems, such as $SrTiO_3$, irradiated by Ar^+ ions.[80] In general, films of hafnium oxide which exhibit room temperature ferromagnetism can be categorised in two groups, undoped (and contamination-free) and doped hafnia.

1.3.3.1 Undoped hafnia

In the case of HfO_2, neither the cation Hf^{4+} nor the anion O^{2-} are magnetic ions and the *d* and *f* shells of Hf^{4+} are full and empty, respectively. The electronic spins in insulating oxides do couple by nearest-neighbour interactions (superexchange or double exchange), due to the closed shell configuration no long-range order below the percolation threshold can be explained by classical theory.[81] A model explaining d^0-ferromagnetism (d^0-ferromagnetism denotes to ferromagnetism in materials with closed *d*-shell configuration) has been proposed by Venkatesan *et al*. They suggest the formation of an impurity band due to the formation of oxygen vacancies in HfO_2 during deposition.[77] This impurity band could hybridise with the empty 5*d* states of Hf^{4+}, transforming a portion of electrons into these states. This allows the 5*d* states to polarise the impurity band, which in turn could now couple ferromagnetically.[77] Coey *et al*. reported that films of pure (undoped and contamination-free) HfO_2 thin films grown on *r*-cut and *c*-cut sapphire substrates exhibit ferromagnetic moments of 150 – 400 μ_B nm^{-2} with Curie temperatures far beyond 400 K.[82] The magnetic moment did not scale with film thickness and was highly anisotropic. This anisotropy in combination with the near absence of a ferromagnetic hysteresis has been interpreted by the presence of persistent orbital currents due to unpaired electrons in extended molecular orbitals associated with oxygen vacancies.[82] The ferromagnetic moment could be influenced by post deposition heat treatments. When annealing under oxygen the ferromagnetic moment decreased, whereas annealing under vacuum retrieved the moment. In the same study, hafnium oxide powder has been heat treated in a similar way, showing similar results. Wang *et al*. conducted annealing experiments of HfO_2 powder in a highly reducing hydrogen atmosphere, thus likely to create more oxygen vacancies than annealing in vacuum.[83] In contrast to Coey *et al*., they could not find any changes of the diamagnetic behaviour of HfO_2 powder as a function of annealing conditions.

Contrary to the proposed defect band model, Abraham *et al*. suggested the presence of magnetic impurity clusters in the films due to contamination.[84] This contamination was traced down to sample handling with metallic tweezers. The observed magnetic characteristics (anisotropy, coercivity, saturation field, and magnitude of magnetic moment) matched well with values obtained by Venkatesan *et al*. PLD-grown thin films of HfO_2 on (100) yttria stabilised zirconia substrates, covering a broad range of growth parameters, were studied by Ramachandra Rao *et al*.[85] Here, the substrate temperature has been varied from 600 to 850 °C, whereas the oxygen partial pressure during growth has been explored from 1x10^{-1} to 1x10^{-6} Torr, yielding to pure diamagnetic films.

1.3.3.2 Doped hafnia

In the case of doped semiconducting oxides with transition metals, e.g., Fe^{3+}, Ni^{2+}, Co^{2+}, Mn^{2+}, V^{3+}, according to classical theory room temperature ferromagnetism would exhibit only if enough cations are doped into the dielectric matrix, allowing for long range spin ordering. In principal the dopant could be incorporated in two ways, either homogeneously distributed in the dielectric matrix or accumulated in clusters segregated in the matrix. The amount of dopant necessary to form one magnetic cluster is lower than a few per cent, whereas the amount needed to cross the percolation threshold for homogeneously distributed dopants is far above 5%. The existence of room temperature ferromagnetism in diluted insulating materials is widely accepted, however, the origin of the observed effect is still under debate. The model of cluster formation could of course easily explain the source of ferromagnetism, but many studies do highlight cluster-free grown DMS proven by various spectroscopic and spectrometric analysis tools.

Surprisingly, doping with transition metals in the range of a few atom per cent, which is below the percolation limit, exhibited ferromagnetism with moments too large to be explained by a clustered impurity phase formed in the dielectric matrix.[86, 87] Hong *et al*. have deposited 5 atom per cent Ni-doped thin films of hafnia by laser ablation, leading to ferromagnetic moments in the range of 2.7 μ_B/Ni.[88] They rule out the presence of magnetic clusters, as the observed magnetic domains are larger than 10 μm in size. This study was followed by the investigation of Fe-doped HfO_2 thin films grown by PLD with Fe concentrations in the target of 1 and 5 atom per cent by the same group.[89] It could be demonstrated that with increasing dopant level from 1 to 5% the magnetic moment increased by a factor of three, and the moment could be influenced by post deposition annealing steps. As a result of the post deposition studies, the observed magnetic moment was attributed to the amount of defects (oxygen vacancies) in the material. With increasing defect level (annealing under vacuum) the magnetic moment increased, whereas with decreasing defect level (annealing in air/oxygen) the magnetic moment decreased and finally vanished. A comparison between clustered and unclustered Co-doped HfO_2 grown by MBE has been performed by Soo *et al*. They show that presumably unclustered films, grown at low deposition temperatures (~100 °C) stay as such even after annealing steps to temperatures up to 700 °C, whereas films grown at elevated temperatures (~700 °C) show extensive cluster formation, even for low doping levels of 1%.[90] The homogeneous implantation of 200 keV Ni-ions in HfO_2 thin films grown by rf-sputtering with subsequent 100 MeV Si^{8+} irradiation confirmed the observation of room temperature ferromagnetism in doped HfO_2.[91] Very recently, Yamada *et al*. demonstrated how the phenomenon of room temperature ferromagnetism could be controlled by the electric field effect in Co-doped TiO_2, as they ascribe room temperature ferromagnetism in Co-doped TiO_2 to be mediated by a charge carrier mechanism.[92] They demonstrate that by applying a voltage of a few volts one can transform a low-carrier paramagnetic state into a high-carrier ferromagnetic state. This result points out the potential of DMS for spintronics, as they would allow combining two fundamental physical effects in one device made of one material, often described as gate-tuneable ferromagnetism in an FET. Besides doping HfO_2 with metals, mixtures of hafnium oxide and aluminium oxide have been investigated, exhibiting room temperature ferromagnetism scaling with substrate type, but not with film thickness.[93] This suggests that interfacial defects are responsible for the observed ferromagnetic feature.

In summary it is evident that controlling the number of oxygen vacancies in such materials is the key to understand and control the observed phenomenon of ferromagnetism in an insulating dielectric. The observation of high-T_c ferromagnetism as a function of oxygen vacancies is a palpable example for a debated phenomenon which could be unravelled by utilising the capabilities of RMBE to fabricate oxygen deficient thin films of Hafnia.

1.3.4 Resistive switching

Besides room temperature ferromagnetism, probably the most recently discovered application possibility is the utilisation of HfO_2 in non-volatile memories (NVM) or resistive random access memories (RRAM) based on the resistive switching effect. Resistive switching in HfO_2 as a function of the applied voltage allows the non-volatile storage of information and would significantly boost the importance of hafnium oxide for microelectronics, since it has already been qualified for standard CMOS processing. Resistive switching describes the effect of changing abruptly a materials resistance as a function of an applied voltage. The high resistance and the low resistance state can be interpreted as ‘on’ and ’off’ or ‘0’ and ‘1’, qualifying such materials for the use in logic devices.

Resistive switching is categorised into two different switching mechanisms, (i) unipolar and (ii) bipolar switching. In the case of unipolar switching, the switching procedure is not

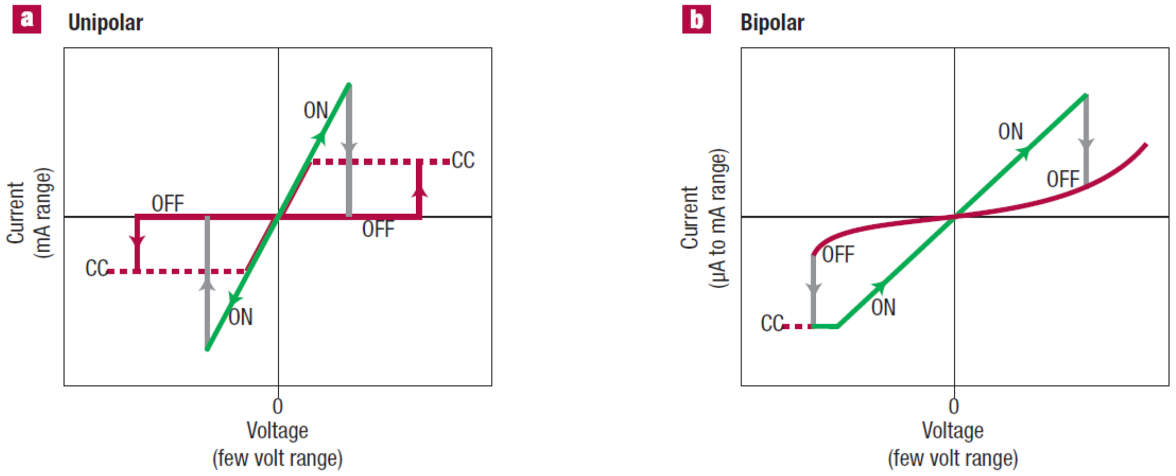

Fig. 1.5: Scheme of (a) unipolar and (b) bipolar switching in resistive switching materials, illustrating the different set ('on') and reset ('off') procedures. Taken from ref. [94].

dependent on the polarity of the voltage and current signal, whereas in the case of bipolar switching the set and reset procedures need opposite polarity, see Fig. 1.5.[94] The physical origin of the resistive switching effect is still under debate, possible explanations include Schottky barrier modification at electrodes, migration of electrode ions (impurity metal ions), space-charge-limited current, Mott's variable range hopping via defect states, filamentation by ordered oxygen deficiency, etc., see ref. [95] and references therein. As an example, in the case of titanium oxide the switching mechanism seems to be based on the formation and rupture of dendrites composed of Magnéli-phases, which are stable crystalline phases of titanium oxide with Ti in a lower valence state than 4^+.[96] In contrast to titanium dioxide, in which stable crystalline phases can be stabilised with lower oxygen content than in TiO_2, there are no such existing stable phases known for hafnia by now.

For hafnium oxide it is assumed that oxygen vacancy percolation is the mechanism responsible for the change in resistance as a function of the applied voltage, an extensive review on oxygen vacancy percolation is presented by Waser *et al.*, see ref. [97]. Summarising this review, the low resistance state in this mechanism is characterised by an oxygen deficient percolation path between cathode and anode formed during electroformation, whereas the high resistance state is characterised by the diffusion of oxygen ions and their recombination with oxygen vacancies, which in turn decrease electrical conductivity along the percolation path.[95] In other words, the resistive switching effect in HfO_2 is strongly dependent on oxygen stoichiometry, the device or path resistivity does change as a function of the oxygen content. Walczyk *et al.* identified a Poole-Frenkel hopping mechanism with a trap energy level of positively charged oxygen vacancy defects ~0.35 eV below the conduction band for the electrical conductivity in Au/HfO_2/TiN stacks, assuming *n*-type conductivity of oxygen deficient $HfO_{2\text{-}x}$.[98, 99]

Today, there are examples of fully integrated $HfO_{2\text{-}x}$-based RRAM devices in 0.18 μm CMOS technology, exhibiting low operation currents down to 25 μA, high on/off ratios (above 1,000), fast switching speed (5 ns), and satisfactory switching endurance ($> 10^6$ cycles) with reliable data retention of 10 years extrapolated at 200 °C.[100] During electroformation and switching, the number of oxygen vacancies is varied, however, to introduce oxygen vacancies into the device most $HfO_{2\text{-}x}$ resistive switching stacks are based on Ti or TiN electrodes, as Ti is

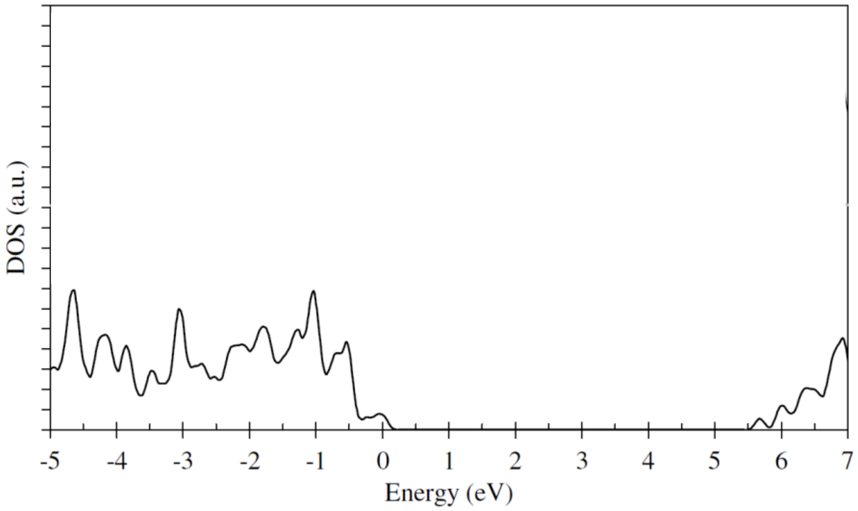

Fig. 1.6: Total density of states (DOS) for ideal monoclinic Hafnia calculated using local density approximation (LDA). Note that the conduction band states of HfO_2 have been rigidly shifted by 1.89 eV to account for the typical LDA underestimation of the electronic gap. Taken from ref. [104].

a strong oxygen getter material leading to the formation of TiO_2/Magnéli Phases and TiO_xN_y interfacial layers, respectively, when annealing (activating) the electrode/HfO_2/electrode stack.[95, 100, 101] Only the combination of oxygen getters as electrodes and successful activation yields to device functionality. Studies on the influence of the top electrode in metal/insulator/metal hafnium oxide-based diodes correlated oxide formation enthalpy, ΔH_f^0, of metal electrode materials (Al, Cu, Hf, Pt, Ti) with stack performance revealing that stacks with Ti electrodes (high ΔH_f^0) show bipolar switching at best performance.[102]

From this short introduction in hafnia-based resistive switching it is evident that controlling oxygen stoichiometry in hafnia is the key to control resistive switching in hafnia-based memristive devices. In contrast to the introduction of oxygen vacancies by activation (formation) via annealing of HfO_2 in contact with an oxygen getter, or controlling the amount of oxygen vacancies of TiO_2-based stacks by the introduction of additional Ti layers,[103] RMBE could *in situ* introduce oxygen vacancies into HfO_{2-x} *during growth* in a highly controlled manner, without the necessity for oxygen getters thereby eliminating the electroforming step altogether. This could open up entirely new possibilities in device design, as also electrodes with low oxide formation enthalpies could be utilised, and specific variations of the oxygen content by RMBE could significantly help to shed light on the physical origin of the resistive switching phenomenon.

1.3.5 Defect chemistry of hafnia

A general understanding of the defect chemistry of hafnium oxide thin films is vital to understand the origin of most of its physical properties, e.g., optical, electrical, and magnetic properties. As known, ideal (defect-free) monoclinic hafnium oxide is an insulator with a wide band gap of around 5.7 eV. Figure 1.6 shows the LDA calculated density of states for ideal monoclinic hafnium dioxide.[104] Note that the conduction band states have been shifted rigidly by 1.89 eV to account for the typical LDA underestimation of the electronic gap from experimental data (5.68 eV).[104]

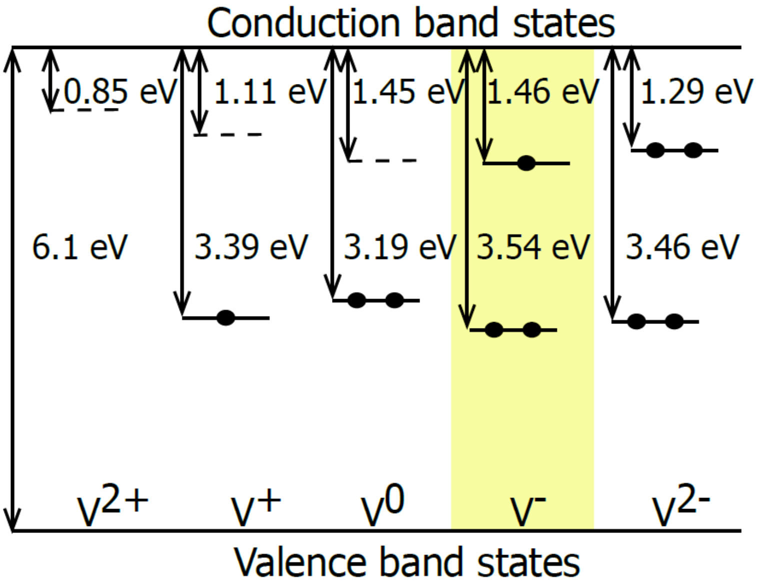

Fig. 1.7: One-electron level diagram for the four-coordinated oxygen vacancy in *m*-HfO_2 calculated using the periodic model. Continuous lines represent occupied states, dotted lines represent unoccupied states. Reproduced after ref. [106].

According to classical defect chemistry, removing Hf ions from the crystal lattice can be described by *p*-doping, whereas the removal of oxygen atoms, thus introducing oxygen vacancies, can be described by *n*-doping. There are mainly three different possible vacancies in hafnia, three-fold and four-fold coordinated oxygen vacancies, and a seven-fold coordinated hafnium vacancy. Oxygen vacancies in hafnia can be double or single positively charged (V_O^{++}, V_O^{+}), neutral (V_O), and single or double negatively charged (V_O^{-}, V_O^{--}), dependent on the number of trapped electrons. The corresponding energy levels have been calculated using the screened exact exchange and weighted density approximation methods within the local density formalism.[105] These methods have the advantage of giving the correct band gap of stoichiometric HfO_2. Similar results for the simulation of localised one-electron oxygen vacancy defect energies have been obtained by Muñoz-Ramo *et al.*, results are shown in Fig. 1.7.[106]

As one electron level differences only provide a poor estimate of optical transition energies, time dependent DFT (TDDFT) has been applied leading to different absorption energies.[107] As an example, for V_O^{-} states the transition energy from occupied mid-gap states to the conduction band is calculated to be 3.54 eV via the one-electron level, whereas for TDDFT this energy is calculated to be 3.20 eV. Muñoz-Ramo *et al.* confirm that both hole and electron polarons in *m*-HfO_2 could be observable as stable immobile defects at low temperatures and exhibit hopping mobility at relatively high temperature.[107] Broqvist *et al.* have calculated oxygen vacancy defect states using a hybrid density functional leading to exact reproducibility of the optical band gap, and show that three-fold and four-fold oxygen vacancies can account for a Poole-Frenkel type trap assisted hopping conduction mechanism.[108] Simulations of the formation energy of all five types of oxygen vacancies in hafnium oxide as a function of the Fermi energy allow the determination of the most likely type of defect for different defect concentrations (the higher the defect concentration, the higher the Fermi energy).[105, 108] According to this model, the V_O^{++} is the most stable oxygen vacancy for low Fermi levels (in the middle of the band gap); with increasing Fermi level, thus increasing defect concentration, V_O^{++} is replaced by V_O^{+} as the most stable defect, V_O, V_O^{-}, and V_O^{--} follow consequently.

By experiment, the formation and change of concentration of oxygen vacancies has been visualised at various physical phenomena. As an example, it has been shown that photoluminescence is evoked in oxygen vacancy-rich hafnium oxide and can be scaled as a function of the annealing conditions in either reducing or oxidising atmosphere.[109] However, such studies are limited to a qualitative proof that oxygen vacancies can be introduced in thin films of hafnium oxide, but lack of descriptions on the absolute number of defects and their energetic classification with respect to valence and conduction band. Complementary to oxygen vacancies, Foster *et al.* have performed plane wave density functional theory calculations on atomic and molecular oxygen interstitials in hafnium oxide thin films on silicon substrates, pointing out that obviously the incorporation of atomic oxygen is favoured against the incorporation of molecular oxygen as interstitials.[110] The influence of different *p*-gate metals and their different mechanisms of Fermi level pinning have been investigated by Robertson *et al.*, as for the utilisation of HfO_2 in aggressively scaled CMOS devices at low EOT, the Fermi level seems to be pinned inside the optical band gap regardless of the metal gate material, as defects (oxygen vacancies) are introduced within the band gap pinning the Fermi level.[111]

Theoretical calculations and simulations of defects in hafnia have also been extensively used to explain the origin of room temperature ferromagnetism in oxygen deficient hafnium oxide. Weng *et al.* have performed first-principles calculations on hole-doped hafnium oxide thin films with non-magnetic ions (K, Sr, Al) and hafnium vacancies, leading to possible ferromagnetism in oxygen *p*-orbitals.[112] Das Pemmaraju *et al.* attribute the source of ferromagnetism to Hf vacancies, which show a high-spin state in their calculations with an associated moment of 3.5 μ_B.[113] These are ferromagnetically coupled via minority-spin electron delocalization across the bridging Hf sites, with a large coupling strength suggesting high Curie temperatures.[113] Other reports on the simulation of Ce-doped, oxygen deficient hafnium oxide predict that even in the case of *n*-doping by Ce, the removal of oxygen atoms leads to localised states not only containing Ce 4*f* electrons but also receiving substantial contribution from electrons remaining on the oxygen vacancy sites.[114] In contrast to *p*-type doping, Venkatesan *et al.* proposed *n*-type doping of hafnia due to the introduction of oxygen vacancies, as each removed oxygen atom dopes two electrons into the system.[77] These at discrete defect sites localised electrons tend to form a defect band in close vicinity to the conduction band. Mixing of the defect band with the conduction band could lead to the polarisation of the defect band by transferring a fraction of an electron per oxygen vacancy into empty 5*d* states, providing ferromagnetic coupling.[77]

As evident from this literature survey, there are ample reports on the theoretical calculation and simulation of defect energies in hafnium oxide thin films, especially energetic levels of different types of oxygen vacancies revealing their role in selected physical phenomena. However, most of these studies assume low defect concentrations and do not cover cases with extensive oxygen deficiency. As shown later in this study, RMBE is capable of introducing much higher defect concentrations than what is possible with other deposition methods of hafnia, leading to effects which are, to our knowledge, not yet described by theoretical calculations.

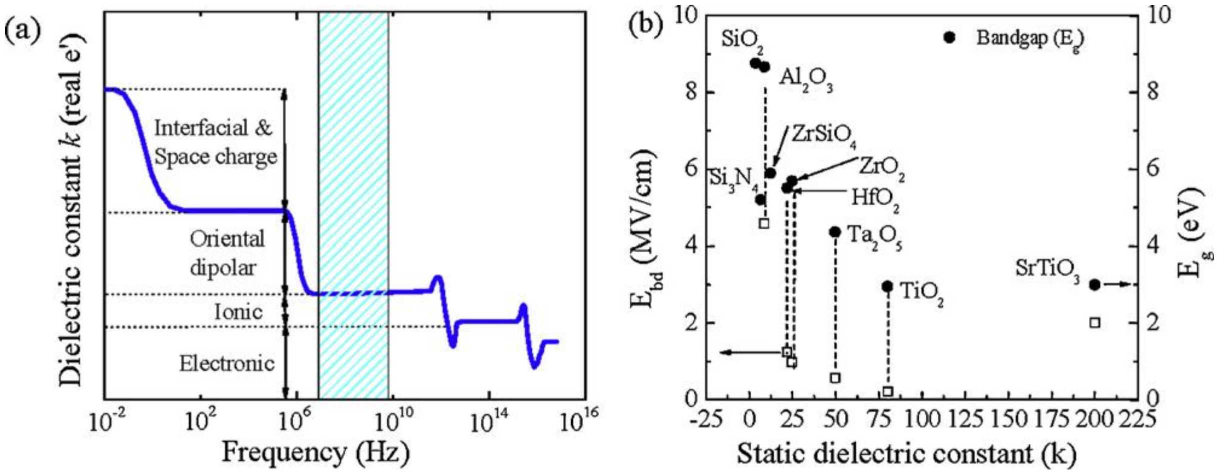

Fig. 1.8: (a) Schematic diagram illustrating the dependence of static dielectric constant on frequency. (b) Band gap (E_g) vs. dielectric constant (κ), and electrical breakdown field (E_{bd}) for representative high-κ materials. From ref. [118] and ref. [73].

1.3.6 HfO_2 as a gate dielectric

It has been evident that the well-known system of Si/SiO_2 in field effect transistors (FET) had to be replaced by novel functional materials. The aggressive scaling of FET structures pushed the SiO_2 gate dielectric thickness to its physical limits of ~1.2 nm, leading to a drastic increase in tunnelling currents up to 100 A/cm^2 at 1 V.[115] This increase in tunnelling currents inhibits the further use of SiO_2 as a gate dielectric in FET devices. To keep up with Moore's law, which predicts a doubling of transistor density every two years,[116] SiO_2 as a gate dielectric had to be replaced by a suitable high-κ material allowing to increase the gate oxide thickness while maintaining similar gate capacitance. Replacing the established Si/SiO_2 system as a gate dielectric in CMOS devices has risen various challenges to be solved, especially process compatibility with existing CMOS fabrication methods, to facilitate the usage of existing production lines, capacities and know-how. Besides process integration, other challenges had to be faced, which are maximising the dielectric constant, having wide band gaps but proper band alignment, solving chemical and structural substrate compatibility, establishing chemical, structural and electrical compatibility with state-of-the-art contact materials, and ensuring the control of formation of unwanted interfacial layers, just to name a few. In order to face the mentioned challenges, extensive research efforts have been invested over the last decade.

For the application as a gate dielectric, metal candidates with large atomic number (large number of electrons) forming an ionic bond with oxygen are needed, as the dielectric permittivity is largely dependent on the ionic and electronic polarisability, see Fig. 1.8 (a). Besides dielectric permittivity, one also has to focus on other properties, such as the attainable band gap, E_g, and the breakdown field, E_{bd}, otherwise no proper band alignment can be achieved in a later device in contact with standard electrode materials. Obviously it is not possible to maximise κ, E_g, and E_{bd} simultaneously, as stronger polarisability implies weaker bonding, and weaker bonding implies a smaller separation between bonding and antibonding energies.[117] In Fig. 1.8 (a) the dependence of the static dielectric constant is shown as a function of frequency,[118] Fig. 1.8 (b) shows prominent screened candidates for the application as a gate dielectric as a function of κ, E_g, and E_{bd}.[73] A compromise between κ, E_g, and E_{bd} made HfO_2 to be among the best candidates, as it exhibits a static dielectric permittivity of around 25, a band gap of 5.7 eV, and a breakdown field of around 5.5 MV/cm.

Nowadays hafnia has proven to be among the best candidates in terms of performance and semiconductor processing compatibility.[73, 119] However, additional efforts have been put on the further maximisation of the dielectric constant in hafnium oxide by stabilising HfO_2 in its tetragonal or cubic phases exhibiting higher κ-values than observed for the known stable monoclinic structure. This stabilisation was expected to be moderated by doping with, e.g., Si, C, Ge, Sn, Ti, and Ce.[120, 121] Devices with hafnium oxide as a gate dielectric fabricated by ALD, the method of choice for industrial device fabrication, exhibit leakage current densities in the range of 10^{-9} A/cm^2 at an EOT of 0.5 nm and a bias voltage of -1.5 V.[122] Today, the short-channel transistor with Hf-based gate dielectric in a 32 nm node gate-first high-performance technology, comparable to an EOT of ~0.8 and 1.0 nm for *n*-FET and *p*-FET, respectively, marks state-of-the-art CMOS technology.[123] Although this performance is remarkable compared to aggressively scaled Si/SiO_2 technology, the International Roadmap for Semiconductors (ITRS) predicts an EOT of 0.55 nm for high-performance logic transistors on bulk Si in the year 2014, which could refuel the search for even higher-κ materials and metal oxide systems.[124]

1.4 Physics of thin film growth

A brief overview on the basic theory of thin film growth is given in this section, starting with the definition of a thin film, describing film nucleation, and ending with the description of different observable film growth modes.[125-129] The variety of thin film deposition techniques for the growth of hafnium oxide thin films is given in section 1.3.2, whereas technical aspects of hafnium oxide thin films grown by RMBE are given in section 2.

There are manifold definitions of what a thin film is. Regarding film thickness, in semiconductor industry they exhibit thicknesses in the range of a couple of 10 nm down to just one monolayer. In contrast, in electroplating industry film thicknesses are in the μm range, just to give two examples. Thin films of certain materials or compounds exhibit entirely different characteristics compared to their bulk morphology due to a variety of reasons, such as epitaxial strain, quasi-two-dimensional nature, and influence of the surface or interface. In industry thin films do play an important role in nearly all branches, from semiconductors over corrosion protections, wear resistance coatings, sensors, to optical coatings, just to name a few. Dependent on the application, the thin film material, and the substrate type there are various film deposition methods available leading to films of entirely different characteristics and functionalities. Nowadays, tailoring thin film properties according to specific needs and demands becomes more and more important. In this study it is shown how selected physical properties (electrical conductivity, optical band gap) of a thin film can be tuned in a wide range. In the following paragraphs an overview on the theoretical background on thin film formation via evaporation in vacuum is given.

Evaporation of the target material or its single elements is usually the first step to grow a thin film under vacuum conditions. This implies a phase transformation from solid to gaseous either directly via sublimation or via the formation of a melt, whereas the energy for this phase transformation is provided by means of thermal heating. Dependent on the deposition method, the gaseous species do have either low kinetic energy like in the case of slow thermal heating by resistive heating boats, or do have high kinetic energies by evaporation via short

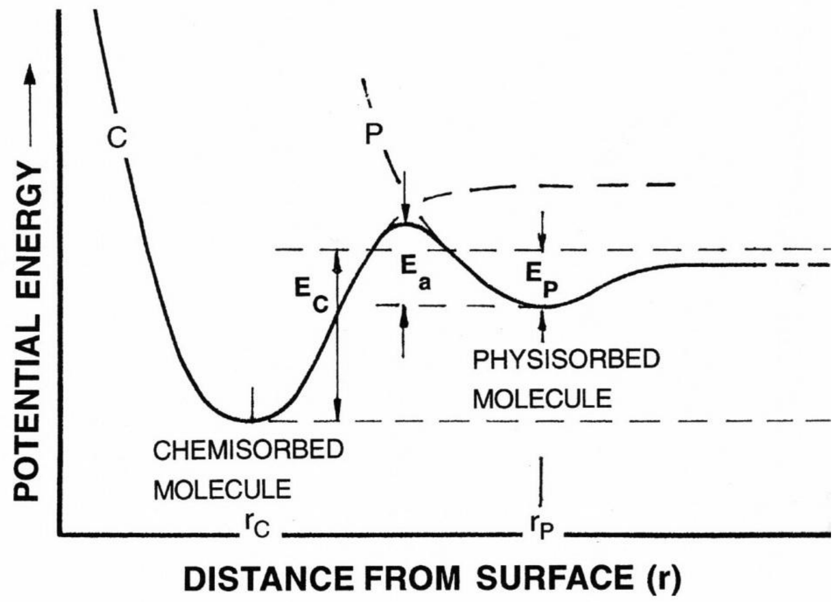

Fig. 1.9: Interaction potential between adsorbate and surface vs. distance *r*, describing the difference between physisorption and chemisorption. Taken from ref. [128].

laser pulses, as an example. Once the material has been transformed into its gaseous aggregate, a mean free path longer than the distance between source and substrate has to be provided in order to allow the evaporated species to reach the substrate without prior interaction with other species. This environment is commonly achieved by placing the experiment in a deposition chamber with a chamber pressure of 10^{-4} mbar or lower, corresponding to a mean free path of 100 cm or more. For comparison, at atmospheric pressure (~1 bar), the mean free path of a molecule is not more than 68 nm.

Considering that the evaporated species arrive at the substrate surface, interaction between hot atoms/molecules (free atoms/molecules with kinetic energy) and substrate takes place by either physi- or chemisorption. Physisorption describes the adsorption of species onto a surface and its binding via van-der-Waals forces, whereas chemisorption considers the change in identity of the adsorbed species by forming ionic or covalent bonds. The adsorption energies differ for physisorption and chemisorption, which are in the range of ~0.25 eV and 1-10 eV, respectively. Figure 1.9 shows the potential energy as a function of the distance of the hot species to the surface, demonstrating the difference between physisorption and chemisorption. The process of adsorption in general (physically and chemically) is called film nucleation, the initial interaction between hot arriving species and the substrate surface. Considering homogeneous nucleation, which is rare since it does not account for the heterogeneous sites that do exist on an accommodating substrate surface, the nucleation rate, $\dot{N}$, is proportional to the product of the equilibrium concentration of stable nuclei, N^* (cm^{-3}), where ω represents the rate in cm^2/s at which atoms/molecules impinge onto the nuclei with a critical area, A^* (cm^2).

$$\dot{N} = N^* A^* \omega \qquad \text{Eq. 1.1}$$

As N^* is temperature-driven, the consideration of a Boltzmann factor for the equilibrium concentration of stable nuclei, N^*, is appropriate.

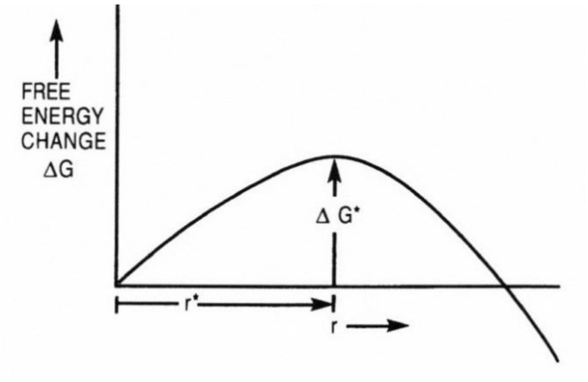

Fig. 1.10: Change of free energy as a function of nucleus radius. For $r < r^*$ the cluster is unstable, for $r > r^*$ the nucleus is stable and starts growing. ΔG^* represents the critical free energy barrier for nucleation, taken from ref. [128].

One can then formulate $N^* = n_s\, exp - (\Delta G^*/k_B T)$, where n_s is the density of all possible nucleation sites, ΔG^* the corresponding free energy, k_B the Boltzmann constant, and T the temperature. The atom impingement flux is equal to the product of the concentration of vapour atoms and the velocity with which they strike the nucleus. This flux ω is given by $\alpha(P_V - P_S)N_A/(2\pi MRT)^{1/2}$, where M is the atomic weight, N_A the Avogadro's number, P_S the vapour pressure above the solid, P_v the pressure of the supersaturated vapour, α the sticking coefficient, and R the ideal gas constant. The nucleus area A^* is given by $4\pi r^2$, as gas atoms impinge over the entire spherical surface. Combining these terms allows the formulation of $\dot{N}$ as follows.

$$\dot{N} = n_S \left[exp - \frac{\Delta G^*}{k_B T}\right] 4\pi r^2 \frac{\alpha(P_V - P_S)/N_A}{\sqrt{2\pi MRT}} \qquad \text{Eq. 1.2}$$

Equation 1.2 shows the strong dependence of the nucleation rate on the free energy ΔG^* due to the exponential expression; ΔG^* itself is very much dependent on the supersaturation S according to $\Delta G = -k_B T/\Omega \ln(1+S)$ where Ω represents the atomic volume and $S = (P_v - P_S)/P_S$. It means that when the vapour supersaturation is sufficiently large, homogenous nucleation *in the gas* is possible. Homogeneous nucleation plays a role mostly in CVD processing as an unwanted parasitic effect, since nucleation takes place already in the gas phase and not only on the substrate surface. In terms of the nucleus radius, r, one can define a critical radius r^*, which corresponds to a critical free energy barrier of ΔG^* that has to be accompanied in order to form a stable nucleus. Below r^* the nucleus remains unstable, above r^* the nucleus starts growing, as depicted in Fig. 1.10. However, heterogeneous nucleation is much more complicated, as the nucleation surface sites can be kinks, ledges, dislocations, etc. Considering nucleation on substrate surfaces, the gain in free energy as the driving force for nucleation can be described by means of surface tensions, γ_{sv}, γ_{fv}, and γ_{fs} where the indexes f, s, and v represent film, substrate, and vapour, respectively. The schematic of basic nucleation processes on a substrate surface during vapour deposition is depicted in Fig. 1.11, showing corresponding surface energies and processes during film formation, which are deposition, desorption, vapour adsorption, and surface diffusion. The surface nucleation reaches mechanical equilibrium among the horizontal components when the gain in surface energy by wetting substrate surface is balanced by the loss in energy due to interface and nucleus surface formation. This yields to Young's law (Eq. 1.3).

$$\gamma_{sv} = \gamma_{fs} + \gamma_{fv} cos\theta \qquad \text{Eq. 1.3}$$

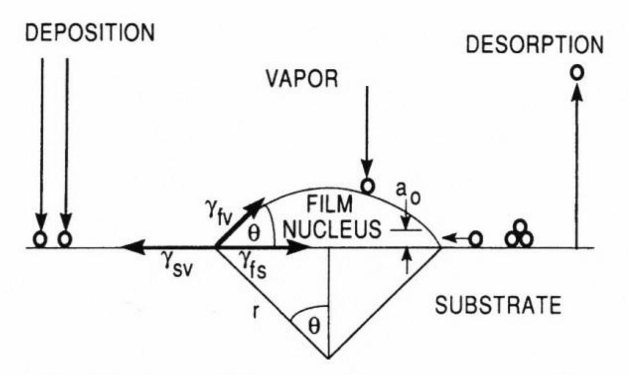

Fig. 1.11: Schematic of the basic atomistic nucleation processes including visualisation of surface tensions, taken from ref. [128].

For heterogeneous growth, the nucleation rate is again very much dependent on the energetics involved, similar to the nucleation rate for homogeneous nucleation. Without deriving the exact formula; $\dot{N}$ for heterogeneous nucleation is the product of two terms, A and B. A equals to the term derived for homogeneous nucleation (Eq. 1.2), whereas B adds a wetting factor dependent on the wetting angle θ, see Fig. 1.11. $\dot{N}$ becomes zero for a wetting angle of 0° and unity for a wetting angle of 180°. In other words, when the film wets the substrate, there is no barrier for nucleation, whereas for the case of extreme de-wetting, the energy barrier is highest and therefore similar to Eq. 1.1 for homogeneous nucleation. This implies that the surface energy of the substrate greatly influences film formation. Dependent on substrate type and film material, the wetting angle θ changes and thus influences the number of nuclei forming on the surface.

Summarising the previous paragraph, film nucleation is the first and most important step in film growth, since it greatly influences film quality. We have seen that for heterogeneous nucleation there is a strong dependence on the different surface and interface tensions, pointing out that mostly the substrate surface properties are influencing the nucleation rate. Qualitatively, the substrate moderates film growth due to lattice misfit, thermal stress, defects appearing at the interface, chemical interactions, and segregation. All these factors determine the three tension factors from Young's formula. Besides surface properties, the nucleation rate is mainly dependent on substrate temperature and deposition rate. For better clarity, the influence of substrate temperature and deposition rate is summarised in the following bullet points.

- Higher substrate temperature leads to an increase in critical nucleus size.
- Discontinuous island structure persists to a higher average coverage for higher substrate temperatures.
- The nucleation barrier decreases with lowering substrate temperature.
- A continuous film takes longer to form for higher temperatures.
- Increasing deposition rate leads to smaller islands.
- High substrate temperatures and low growth rates yield to large crystals or even single crystals, whereas
- low substrate temperature and high growth rates yield to polycrystalline deposits.

The last part of section 1.4 describes the different growth modes obtained during vacuum-based thin film growth. One can distinguish between five different growth modes, which

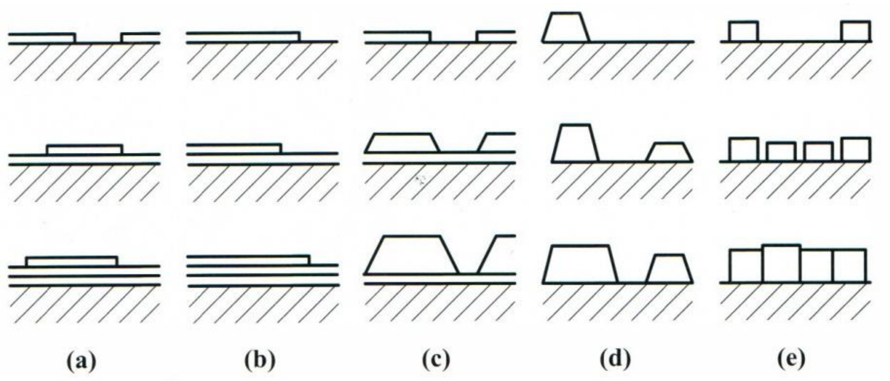

Fig. 1.12: Schematic visualisation of the five different growth modes, (a) Layer-by-Layer or Frank-van-der-Merwe; (b) step flow; (c) layer plus island or Stranski-Krastanov; (d) island or Vollmer-Weber; (e) columnar growth mode, from ref. [126].

are Volmer-Weber mode, Frank-Van der Merwe mode, Stranski-Krastanov mode, columnar growth mode, and step flow mode. The mode by which the film grows on the substrate is very much determined by the earlier described factors, substrate temperature, deposition rate, and lattice misfit, which are all input variables to the surface tension γ.

The Volmer-Weber growth mode (island growth mode) describes the situation when the atoms or molecules from the evaporated species directly nucleate on the substrate surface and form islands. In this case, the atoms/molecules are strongly bound to each other and weakly bound to the substrate surface ($\gamma_{fs}\uparrow$). This mode is observed for the growth of many metals on insulators or metals on alkali halides.

The Frank-Van der Merwe growth mode describes the opposite case of Volmer-Weber; the film atoms/molecules are strongly bound to the substrate surface and weakly bound to each other ($\gamma_{fs}\downarrow$). In the ideal case, all formed nuclei merge together and form a single layer on the substrate before the second layer starts to form. Subsequent layers form less tightly bound on top, provided there is a monotonic decrease in binding energy towards the value known for a bulk crystal. This growth mode is prominent for the adsorption of gases on metal surfaces, observable in some metal – metal and semiconductor – semiconductor systems.

As a mixture of Volmer-Weber and Frank-Van der Merwe growth modes, Stranski-Krastanov growth mode describes the formation of a first monolayer on substrate surface followed by the formation of islands on top. The effect of island formation on the first or first few monolayers occurs due to a disturbance of the monotonic decrease in binding energy. Reasons for Stranski-Krastanov growth mode can be manifold, it is often observed in the case of high interface energies in combination with high strain energy in the film. With increasing thickness, the three growth modes Volmer-Weber, Frank-Van der Merwe, and Stranski-Krastanov, do lead to a continuous film in the end, meaning that formed islands merge together at sufficient film thickness forming a connected structure.

Other than that, the columnar growth mode starts with island growth and ends with columnar structures of the film material, which have no structural connectivity and thus can be cleaved and ruptured easily. The resulting structure can be compared with a Whisker-like structure of highly oriented (textured) grains on a substrate. Columnar growth mode is favoured when adsorbed atoms exhibit extreme low mobilities leading to the formation of highly defective atomic columns.

The last growth mode to be mentioned is the step flow growth, which is highly important in the case of epitaxial growth on single crystalline substrates. Nearly all single crystal substrates show a certain miscut with respect to a crystallographic orientation, in other words, the angle between surface normal and corresponding lattice plane normal is greater than 0°. In the case of sufficiently low substrate temperatures and/or high deposition rates (compare with the bullet points earlier), two-dimensional growth can take place, similar to Frank-Van der Merwe and Stranksi-Krastanov growth modes. If the thermal energy of the adsorbed species is increased (higher temperature, lower deposition rate), the increased mobility leads to increased surface diffusion, which in turn allows diffusion and incorporation into the crystal terraces on the substrate surface directly. The result is the simultaneous growth of all steps initially present on the substrate surface, comparable to single waves propagating on top of each other (→ ‘step flow’). All the above mentioned growth modes are visualised in Fig. 1.12.

2 Reactive molecular beam epitaxy

As mentioned in the introductory section of this study, HfO_2 thin films are of high importance for existing and future applications in microelectronics. Attributing to the numerous unexpected physical phenomena related to oxygen vacancies, which still remain to be under debate, the need for a versatile tool to grow hafnium oxide thin films with a precise control of stoichiometry is evident. Since oxygen vacancies in hafnium oxide thin films seem to be responsible for most of their physical properties, defect engineering could certainly help to control the functionalities of hafnia. In this study, reactive molecular beam epitaxy (RMBE) has been used to grow $HfO_{2\pm x}$ thin films with x varying over a broad range. The following sections will give a detailed overview on RMBE in general and explain selected details of the utilised deposition unit for this study and the deposition process.

Molecular beam epitaxy is a UHV-based thin film deposition technique for the growth of high quality, epitaxial structures with monolayer control. Its principle is the evaporation of single atoms or clusters forming an atomic/molecular beam striking a (often heated) substrate. Heating provides thermal energy allowing for diffusion processes, atom migration, and incorporation of atoms into the growing film. The main advantage of MBE is the great flexibility to *in situ* vary film stoichiometry with no need for *ex situ* bulk target preparation, as needed for PLD and sputtering. MBE allows the growth of metastable systems far beyond their thermodynamic equilibrium, for example, by utilising epitaxial strain effects between substrate and film.[130-132] MBE has paved the way for the success of semiconductor industry within the past decades, as all relevant inorganic, semiconductor-based thin film systems of superior quality have been grown by MBE. The continuous search for high-T_c superconductors based on complex oxide materials,[133, 134] the further development of oxide semiconductors,[135, 136] and the increasing importance of complex oxide thin films in general,[20, 137] fostered the advancement of MBE to reactive MBE. RMBE is the combination of MBE with an additional reactant, which could be oxygen, nitrogen, or hydrogen, to name the prominent ones. The reactant is provided simultaneously during evaporation. In the case of oxides, oxygen is mainly supplied by means of radical sources (O^*), ozone generators (O_3), or molecular oxygen (O_2).

Principally two approaches can be distinguished for MBE, (i) shuttered MBE and (ii) simultaneous evaporation of various, usually elemental sources.

i. Shuttered MBE describes elemental evaporation from various sources, which are usually spatially separated by metal plates. Each source is equipped with one separate shutter. All sources are continuously driven at a specific operation point during deposition. For film growth, shutters are opened sequentially leading to a sequential deposition of elements on the substrate. The subsequent opening of shutters, thus the subsequent deposition of different elements, leads to a defined elemental ratio in the film. Diffusion processes during deposition due to substrate heating ensure phase formation. For shuttered MBE, all sources are calibrated once prior to deposition and are operated at one fixed deposition rate. Film composition/stoichiometry is mainly defined by the shutter opening/closing sequence. As all sources are operated at one defined rate, no rate monitoring or rate control during growth is necessary.

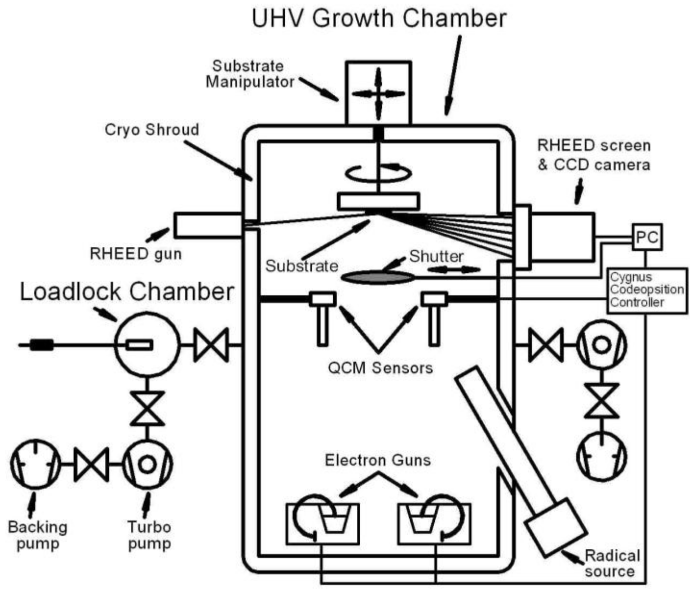

Fig. 2.1: Scheme of the reactive molecular beam epitaxy unit used for this study. For details see text.

ii. In contrast to shuttered MBE, in the second approach various sources are evaporated simultaneously with precise rate monitoring and rate control in real-time. No separate shutters are installed, usually only one shutter at substrate level is used. Film composition is achieved by precise real-time *in situ* rate control of all sources by means of, e.g., quartz crystal microbalances, electron impact emission spectroscopy, or atomic absorption spectroscopy. As film stoichiometry is controlled directly by the source evaporation rates, precise (rate deviation below 1%), fast (within few seconds or faster), and feed-back looped rate control is decisive.

For this study, a custom-made RMBE unit based on co-evaporation of single elements has been used. During these studies, a new state-of-the-art RMBE has been developed and set up in an integrated cluster system, combining PLD and ADOMBE, see section 1.1. The following sections describe characteristics and functionalities of the UHV system of the utilised unit, focussing on electron beam evaporation, *in situ* oxidation capabilities, and rate & growth monitoring. The chapter finishes with a description of the growth procedure specific to the growth of hafnium oxide thin films. Theoretical background on fundamentals and historical developments of MBE in general can be found in ref. [125-127], for oxide-MBE in ref. [138-140].

2.1 UHV-system

2.1.1 Technical aspects

The RMBE unit used for this study consists of a custom-made ultra-high vacuum stainless-steel chamber (base pressure ~10^{-9} mbar) with a load lock arrangement, as illustrated in Fig. 2.1. and Fig. 2.2 (by courtesy of Gabi Haindl). A base pressure below 10^{-4} mbar is necessary to provide a mean free path of the evaporated atoms/molecules of more than 100 cm (or at least chamber size). Besides the provision of a mean free path, contamination issues due to residual gases are minimised, diffusion processes of adsorbed atoms on substrate surface are enhanced, and operating conditions for e-beam evaporation, mass spectrometry/spectroscopy,

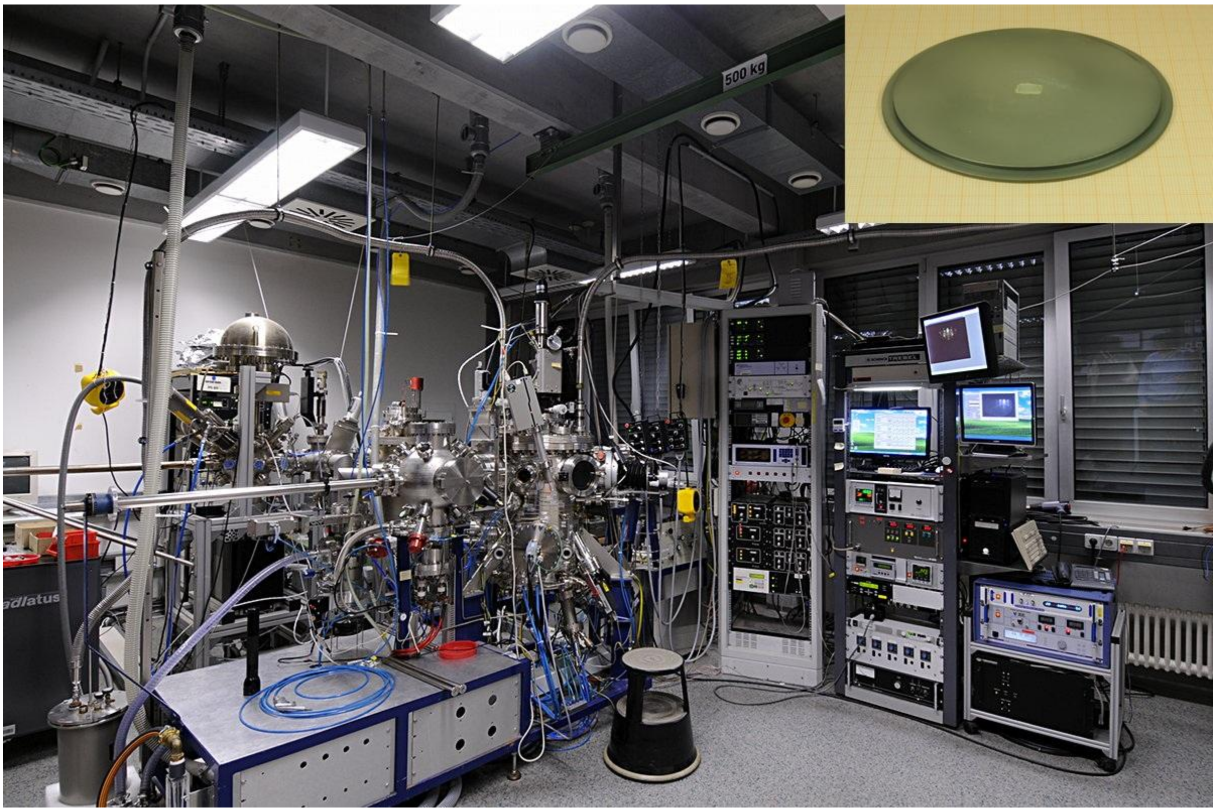

Fig. 2.2: Image of the utilised RMBE for this study. Inset shows photograph of a 7 x 4 mm^2 substrate pasted with silver paste on a 4” stainless-steel substrate holder.

and RHEED are provided. Vacuum generation is achieved by means of standard, oil-based rotary vane pumps for chamber roughening, equipped with oil adsorption traps and vibration dampers in combination with high-capacity turbo molecular pumps. A cooling shroud (double-walled stainless-steel jacket) is mounted inside the vessel that can be filled with liquid nitrogen during growth, then acting as a cryo pump by providing a 77 K cold surface for gas adsorption. Growth chamber and load lock chamber are equipped with separate pumping systems, corresponding pneumatic valves are remote-controlled via a valve board as a 19” rack insert, see Fig. 2.3.

In the case of MBE, maintaining UHV conditions is usually achieved by means of passive vacuum preservative devices, such as, getter pumps, cryopumps, and cooling shrouds, as the amount of residual gases is limited during growth. As for RMBE, reactive gases (in the present case molecular and radical oxygen) are introduced for *in situ* reaction, continuous and high-throughput pumping systems (e.g., high-capacity turbo molecular pumps) are applied. For residual gas analysis during growth, for leak checking with gaseous Helium, for monitoring reactive gas inlets, and for monitoring chamber bake-out, a quadrupole mass spectrometer or residual gas analyser (RGA) is attached to the chamber. Besides total pressure measurement, it allows the detection of particles up to 200 atomic mass units (amu) with an accuracy of 1 amu, thus allowing the identification of most species found as residuals in HV and UHV chambers.

The substrate manipulator, one of the most important components of a deposition system, is mounted on top of the growth chamber. Besides substrate manipulation (rotation, *x*-, *y*-, and *z*-movement), the manipulator provides facilities for substrate heating, which is essential for high quality thin film growth. In the present case, substrates are fixed with silver paste

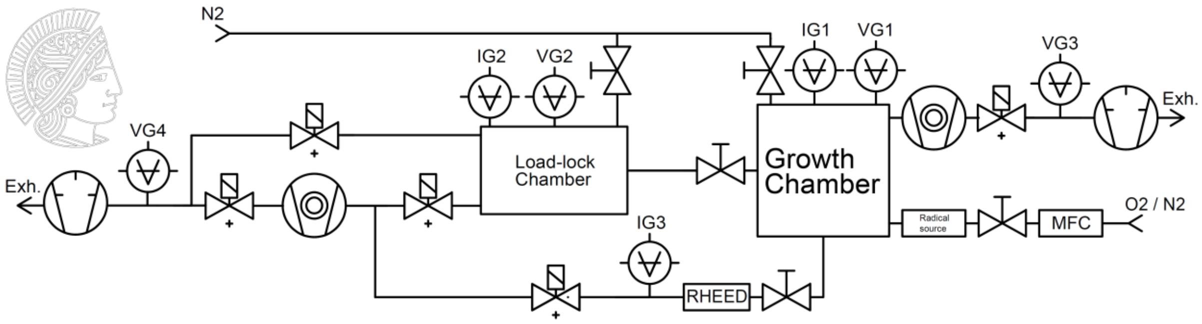

Fig. 2.3: Schematic of the 19” valve board of the utilised RMBE unit including corresponding vacuum gauges (IG = ion gauge; VG = convectron/pirani gauge).

onto 4” stainless-steel holders, which are radiantly heated on the rear side with a ceramic area heater of 2” diameter (see inset of Fig. 2.2, by courtesy of Gabi Haindl). Substrate temperature is measured by a calibrated thermocouple located on the backside of the substrate holder. Temperature calibration is achieved by means of a pyrometer pointing on the substrate holder front. Direct temperature measurement of the substrate and/or the film forming on the substrate is usually not possible with pyrometers, as the emissivity changes during deposition. For calibration purposes, a two colour pyrometer can be attached to the chamber, allowing emissivity-independent measurements. For *in situ* oxidation a radical source is attached to the chamber bottom, which is described in detail in section 2.3. The system is equipped with three e-beam evaporation systems, located equidistant to the substrate at the chamber bottom, which are described in section 2.2. For growth monitoring a 25 keV RHEED system is attached to the chamber, including electron gun, phosphor screen, CCD-camera, and ksa 400 evaluation software, see section 2.5. Rate monitoring is achieved by four QCMs, one for each e-gun located at the unit bottom, and one QCM at substrate level for *in situ* calibration, see section 2.4.

2.1.2 Chamber Preparation

Ensuring a contamination-free ultra-high vacuum, the system has to be baked out at temperatures above 100 °C after each exposure to atmospheric conditions. Baking above 100 °C removes the majority of adsorbed water molecules and yields to a base pressure in the range of 10^{-9} mbar. Lower base pressures are usually not required for RMBE, as in the case of oxide thin films, oxygen radicals are introduced into the growth chamber during growth leading to growth pressures in the range of 10^{-7} mbar or even higher. All substrate holders are sandblasted to remove old deposit or other possible contaminations, ensuring holder cleanliness and defined emissivity. Holders are pre-heated prior to deposition to temperatures of 800 °C to allow decomposition of organic binders and solvents (silver paste) and to allow degassing. Extreme care is taken during every step involving handling of UHV-exposed parts to reduce the possibility of introducing contaminations into the deposition chamber, which could lead to a contamination of the grown thin films. Pasting substrates with silver paste provide good thermal contact to substrate holder, proper physical fixing, and usually well accessible samples in terms of RHEED. Limitations are maximum operation temperature (silver starts melting at 960 °C in ambient conditions, in vacuum even lower) and contamination issues due to silver diffusion into the films. The shroud is filled with LN_2 prior to e-gun operation, as the cooled shroud acts as a cryogenic pump providing a cold (77 K) surface allowing freezing out

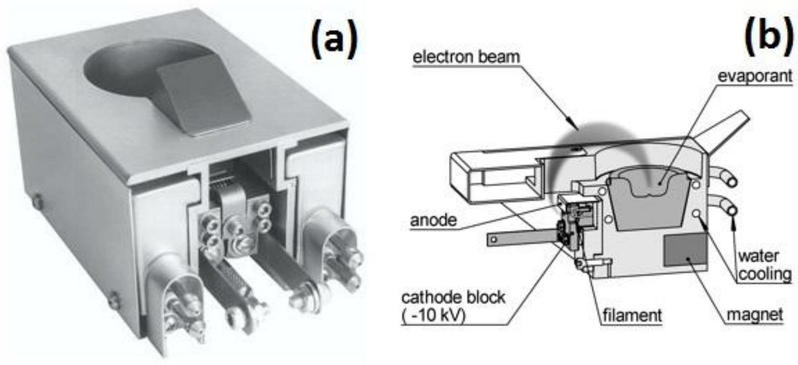

Fig. 2.4: (a) Picture of a Hanks HM^2 single-crucible e-gun; (b) schematic of spatial separation of electron generation and evaporant to avoid cross-contamination. Additionally, beam bending of 270° by permanent magnets is visualised. Taken from Thermionics advertising material.

residual gases, excess reactive gases during deposition, and gases released during initial heating of e-beam sources. A cooled shroud significantly helps to improve chamber pressure and reduces possible sources of film contamination or evaporant reaction.

2.2 Electron beam evaporation

2.2.1 Technical aspects

There are several types of evaporation sources based on the evaporation of material by thermal energy, which can be attached to UHV chambers. Resistive heating of crucibles or boats is probably the cheapest and most common evaporation method, as no technical sophistication is needed and good rate controllability is achieved. Especially for MBE thin film growth, effusion cells are widely used as evaporation sources, as they are suitable for an extensive variety of materials and provide superior source stability. In contrast to direct resistive heating of crucibles or boats, in effusion cells a crucible is indirectly heated by radiation from a filament vicinal to the crucible.

For this study, e-beam evaporation has been applied by utilising Hanks HM^2 single-crucible e-guns from Thermionics, a picture (a) and schematic (b) is shown in Fig. 2.4. E-beam evaporation is based on the thermal creation of free electrons by heating a tungsten filament and accelerating these free electrons by applying a DC-voltage of several kV on the evaporant. Electrons impinging on the evaporant do transform their kinetic energy into heat, thus heating the target directly. As the emission current can be in the range of several 100 mA, the local energy density can be in the range of a couple of kW per square millimetre, high enough to reach any melting, boiling or decomposition temperatures of condensed matter. E-beam evaporation is a direct heating method, as the electron beam directly hits the target material, whereas the crucible is cooled indirectly during evaporation minimising chemical reactions or alloying. To reduce contamination with evaporated tungsten from the filament in the e-gun, the electron beam is first focussed and then bend by 270° using permanent magnets, so the filament stays enclosed within the e-gun. Two sets of sweep-coils are located next to the crucible pocket, which allow the positioning and scans of the e-beam on the target material. As the beam spot is ideally just a few mm^2 in size, smallest fluctuations in beam intensity, especially due to fluctuations of chamber pressure, can result in strong rate fluctuations.

2.2.2 E-gun source preparation

One of the most important aspects of e-beam evaporation is to find a suitable combination of evaporant and crucible material to avoid alloying of the evaporant with the crucible and to avoid evaporant contamination. In order to find such proper combinations, binary phase diagrams of the evaporant and the suggested crucible material can give first information on possible combinations. In addition, several evaporation material or evaporation equipment suppliers (Lesker, MBE components, Thermionics, etc.) provide tables suggesting suitable evaporation methods for a desired compound with corresponding material/crucible combinations. However, binary phase diagrams and evaporation tables are usually limited to values valid in atmospheric pressure (not in UHV) and free of oxygen radicals or other reactants.

2.2.2.1 Hafnium

Tungsten is the material of choice to fabricate a vast variety of crucibles and boats, as it exhibits superior chemical inertness, sufficient stability in oxidative atmospheres (at elevated temperatures), and it has the highest melting point of all known elements. The evaporation of hafnium, a low vapour pressure refractory material with a melting temperature of 2,231 °C and a boiling point of 4,330 °C under ambient conditions (in vacuum lower), is not accessible by evaporation techniques based on resistive heating. Although the melting point of tungsten lies with 3,422 °C (ambient conditions) well above the melting point of hafnium, hafnium cannot be evaporated in a resistively heated tungsten boat as hafnium and tungsten are subject to alloying at elevated temperatures. Once metal hafnium starts to melt, the melt wets the tungsten crucible, provided the temperature of the crucible is similar or even higher than the temperature of the melt (which would be the case for resistive heating). As alloying is usually an exothermic reaction, the chance is high that the crucible will fail as it can get eaten up by the melt very fast once reaching the temperature at which alloying between hafnium and tungsten takes place. However, alloying will certainly lead to the contamination of the source material with crucible material. The corresponding binary phase diagram of Hf and W is shown in Fig. 2.5, depicting that hafnium and tungsten are congruently melting and do form a low melting point eutectic for low hafnium concentrations.[141] However, tungsten exhibits a very high melting temperature, so if the crucible is kept sufficiently cold (below 2,000 K), alloying can be avoided.

Therefore, metal hafnium (¼” x ¼” ingots, 99.9% purity except for Zr, MaTecK) was evaporated in self-made tungsten 10 cc crucibles, using e-beam evaporation. The local evaporation spot was kept as small as possible and thermal contact of the target material ingots to the crucible was minimised to avoid alloying with the tungsten crucible. The hafnium metal ingots were assorted in the tungsten crucible and melted in such a way that the melted portion of hafnium was not touching the crucible walls in no case. Source cleanliness was ensured by SIMS studies, as (i) the pristine supplied hafnium ingots and (ii) small crystals of deposited metal hafnium from the crucible side walls were checked for any impurities other than Zr. In all cases neither traces of tungsten nor any other significant contaminations were identified within the resolution limits. Special attention has been paid to magnetic impurities (Fe, Ni, Co), as for the doping studies (see section 6) hafnium oxide thin films, free of any

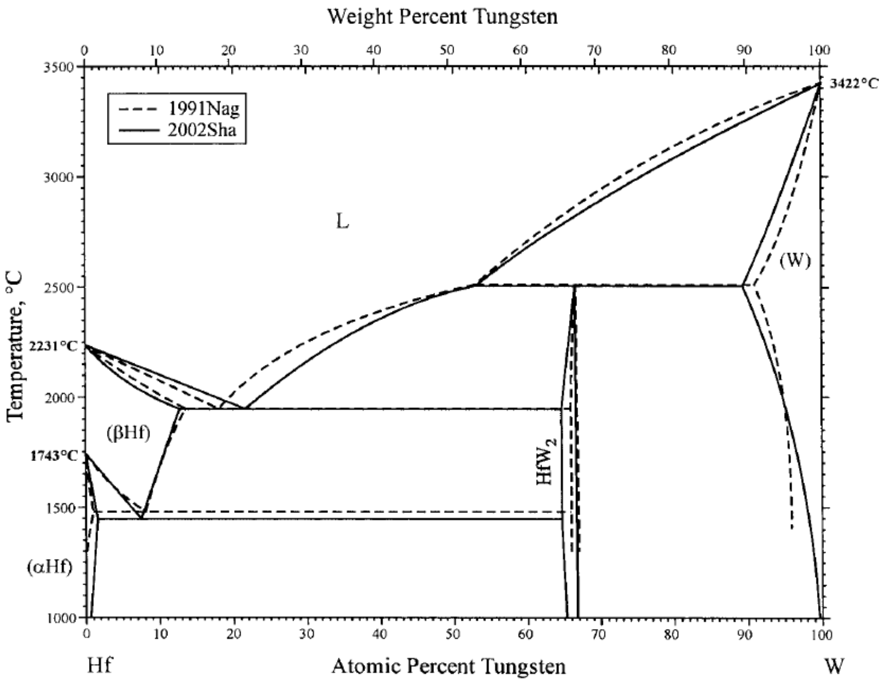

Fig. 2.5: Binary phase diagram of Hf-W, taken from ref. [141].

magnetic impurities, had to be grown. Figure 2.6 (a) shows a photograph of the melted Hf source utilised for this study (by courtesy of Gabi Haindl).

2.2.2.2 Nickel

For e-beam evaporation of Ni comparable aspects have to be taken into account as for the evaporation of Hf. At first, a suitable combination of evaporant and crucible material has to be identified, which has to be validated for the thin film growth conditions (in vacuum with oxygen radicals). When checking the binary phase diagram for Ni and W (not shown), both metals are congruently melting forming no low melting point eutectic. Evaporation tables name tungsten to be the crucible material of choice for the evaporation of Ni in vacuum, however, only very little information on how oxygen radicals influence alloying of Ni and W is available.

Therefore, metal Ni (¼” x ¼” pellets, 99.995% purity, Lesker) was evaporated in crucibles made of Fabmate. Fabmate is sintered graphite, hence consists of pure carbon. The surface of Fabmate crucibles is much smoother compared with the surface of pristine graphite crucibles, thus reducing the possibility for chemical reaction between evaporant and crucible by reducing crucible surface area. Another advantage of Fabmate is the fact that even when the evaporant is contaminated with carbon, the presence of oxygen radicals ensures the oxidation of any carbon atoms to carbon mono-/dioxide before getting incorporated into the film. A drawback of Fabmate is the material’s brittleness, the capability of accommodating stress & strain is poor and its thermal expansion during heating/cooling of the evaporant does not match to that of metals. The Fabmate liner has been put into a copper susceptor to avoid issues arising due to crucible cracking, which prevents the e-beam pocket from any possible damage due to crucible cracking. Figure 2.6 (b) depicts the Ni source used for this study (by courtesy of Gabi Haindl).

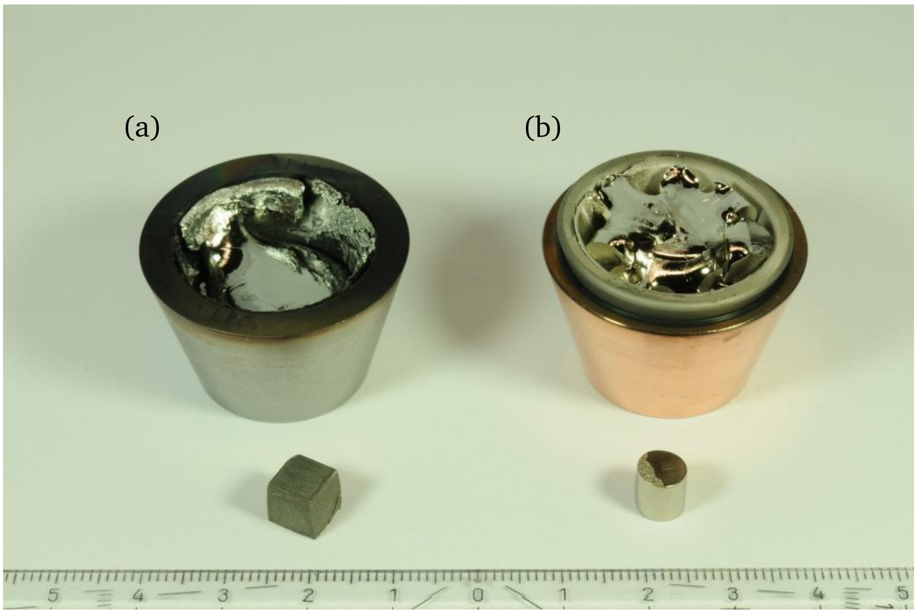

Fig. 2.6: (a) melted hafnium source in a tungsten crucible, in front a ¼" x ¼" pellet of metal Hf, (b) melted Ni source in a Fabmate crucible sitting in a copper susceptor, in front a ¼" x ¼" pellet of metal Ni.

Another aspect to be mentioned is the effect of ferromagnetic materials on e-beam characteristics, as melted ferromagnetic materials (Ni, Fe, Co) that are cooled down slowly yield to considerably large single crystals in the crucible. These large single crystals have large Weiß domains, which could align parallel during source solidification according to the magnetic field evoked by the permanent magnets surrounding the e-gun pocket. The resulting magnetic field from the source material for temperatures below T_c can alter the electron beam dramatically. Unwanted beam deflection is reduced by keeping the melted portion of the ferromagnetic source as small as possible.

2.2.3 Film doping

Very often thin films are doped *in situ* with certain materials, either to influence physical film properties or to generate new film characteristics. In the case of HfO_2, doping is mainly used for two different purposes, (i) the stabilisation of crystalline high-κ phases (cubic, tetragonal, orthorhombic), and (ii) doping with Fe, Ni, or Co to induce room temperature ferromagnetism. In the case of transition metal doping for room temperature ferromagnetism, doping rates are usually in the range of some atom per cent. In the case of HfO_2 doped with 4 atom per cent Nickel, a growth rate of 0.7 Å/s of metal Hf requires a doping rate of Nickel of 0.0084 Å/s. The successful stabilisation of rates in this low range can be quite challenging when it comes to e-beam evaporation. As described in the earlier sections, (i) e-guns operated in UHV conditions can be used to melt refractory metals as they reach temperatures well above 4,500 °C, (ii) are fast-responding when connected to a rate thickness controller with feedback-loop, and (iii) exhibit precise rate control. However, a challenge of e-beam evaporation is certainly rate stability, which is very much dependent on growth chamber pressure. As described in section 2.4, the introduction of oxygen into the growth chamber can lead to rate instabilities, which can be in the range of the targeted doping rates or higher. It is not possible to sufficiently stabilise metal evaporation rates (Hf or Ni) of 0.0048 Å/s when oxygen radicals are supplied simultaneously. However, the higher the evaporation rate of an e-beam source is (under oxygen radicals), the better source stability and the more independently the evaporation rate can be adjusted from changes in chamber pressure.

How can we achieve *in situ* transition metal doping of HfO_2? Apparently a nearby solution is the combination of e-beam evaporation of Hf and effusion cell evaporation of Ni. In many cases effusion cells are the method of choice for metal evaporation with a need for precise rate controllability at low rates, especially for the growth of inorganic semiconductors. Rate calibration is achieved by standard *ex situ* thickness calibration, whereas the source usually runs under vacuum conditions (no oxygen) and rate control is achieved by precise temperature controllers. Source temperature can be directly translated into evaporation rate, temperature-vs.-rate plots allow to operate effusion cells without *in situ* rate monitoring tools. When it comes to RMBE, these aspects are not valid anymore, as effusion cells would not run under constant UHV conditions. A change in chamber pressure (due to a change of the oxygen flow rate) would significantly influence the effective effusion cell rate (effective means the rate measured at substrate level). This aspect prompts the need for continuous *in situ* rate control of the dopant, which itself excludes the utilisation of effusion cells in combination with QCMs. Due to the rather focussed atomic beam flux of the effusion cell compared to the radially symmetric (cosine-shaped) beam flux of an e-beam source, effusion cells are not accessible via QCM rate control. Alternatively one could increase both rates of e-beam evaporated Hf and Ni up to rates which could be sufficiently stabilised, but maintaining same Hf to Ni ratio. This would lead to very high rates for the Hf flux of more than 7 Å/s with a given Ni-rate of 0.1 Å/s, corresponding to a doping concentration of ~4%. Such high evaporation rates would in consequence influence film formation in a negative way.

The solution applied for this study is to use e-beam evaporation for both metals, Hf and Ni, in combination with a screening of the Ni flux. This is accomplished by inserting a stainless-steel screen between source and substrate allowing to reduce the effective flux at substrate level by a factor of 10, thus allowing running the Ni source at rates in the range of 0.1 Å/s when targeting doping rates of ~4 atom per cent. This widens the range of realisable doping rates significantly and allows to conduct doping experiments with doping rates from values of more than 50 atom per cent down to a few atom per cent. Beam uniformity is granted, as (i) the screen is placed close to the source and far away from the substrate. In addition, continuous substrate holder rotation ensures homogeneous deposit on the substrate from all sources.

2.3 Oxidation

The growth of complex oxides demands for oxygen sources with high oxidation power, good controllability, but still allowing low deposition pressures. In RMBE, oxygen is provided mainly in four different aggregates, (i) molecular oxygen (O_2), (ii) activated oxygen (O^*), (iii) ozone (O_3), and (iv) ionic oxygen (O^{x-}), sorted by increasing oxidation power. As deposition pressures have to be kept as low as possible, the nearby solution would be to choose the aggregate with highest oxidation power, since the higher the oxidation power is, the lower the necessary gas flow into the chamber and, thus, the lower the deposition pressure. The incorporation of oxygen ions in thin films usually has negative implications. Additionally, radical oxygen presents precise flow control by means of adjusting the molecular oxygen flow rate

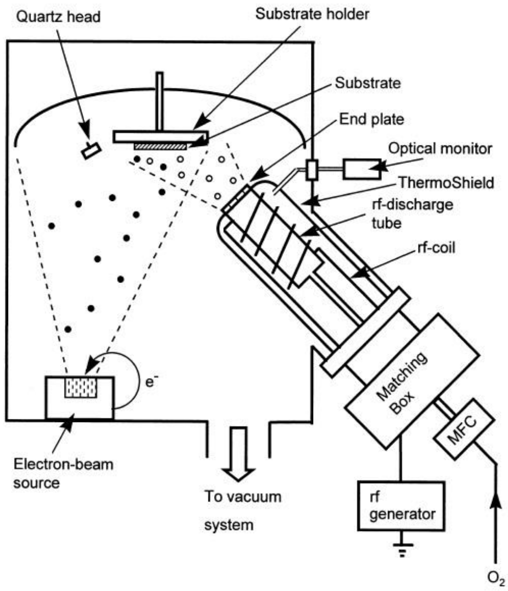

Fig. 2.7: Scheme of a radical source attached to a deposition chamber highlighting spatial arrangement of discharge tube, rf-coil, and aperture (end plate). Taken from ref. [142].

and/or adjusting the rf-power, and is less dangerous in handling compared to ozone. That is why it is very often the aggregate of choice for oxide thin film growth.[142-144]

The grade of technical sophistication for oxygen radical creation and precise controllability is limited: to create oxygen radicals, an MFC-controlled stream of molecular oxygen is passed through a quartz discharge tube (resonant cavity) with an aperture (plate with holes of defined diameter and distance) to direct the radical beam towards the substrate. The discharge tube can be made of various materials, such as, alumina, boron nitride, or quartz, to name the prominent ones. An rf-coil powered by an rf-generator operating at 13.56 MHz is inductively coupled to the gas within the resonant cavity, allowing an electrical discharge and thus igniting a plasma, see Fig. 2.7 and ref. [145, 146]. Within the plasma, oxygen molecules are cracked (activated) into oxygen radicals, the higher the rf-power applied to the cavity, the higher the cracking efficiency is. In contrast, for a given rf-power the cracking efficiency has a maximum for one specific molecular oxygen flow rate, further increase of the flow rate leads to a decrease in cracking efficiency. In effect, the oxidation power can be changed by varying the rf-power applied to the cavity and/or by varying the oxygen flow supplied to the discharge tube. As the ignited plasma is relatively low in energy, the cracked radicals are passing the aperture with low kinetic energy. An activated oxygen beam is formed and is pointing to the substrate surface; created ions can be deflected away from the substrate by applying a grid voltage on two parallel metal plates located close to the aperture. An auto-tune unit connected to the radical source allows tuning the resistive impedance of the cavity to match with the output resistance of the rf-generator automatically. A photo cell attached to the radical source pointing at the plasma discharge within the cavity allows running the source in a ‘constant plasma intensity’ mode, as it is equipped with a band filter for selective monitoring of the most intense oxygen plasma emission line at 464.9 nm.[147] As change in chamber pressure during run affects the plasma discharge, the photo cell arrangement allows accommodating such changes and maintaining constant oxygen plasma intensity.

For this study, an HD 25 radical source from Oxford Applied Research has been used, whereas the molecular oxygen flow rate (gas purity 99.995%) was regulated by means of an

MFC from MKS with a maximum flow rate of 5 sccm. In order to grow films with molecular oxygen instead of radicals, a stainless-steel nozzle is attached to the deposition chamber pointing towards the substrate and connected to the mass flow controller. The discharge tube of the radical source is made of quartz, which has proven to be the best material being stable in oxygen radicals. Apertures of standard discharge tubes for HD 25 radical sources are designed for comparably high gas flow rates (greater 2 sccm). When it comes to flow rates below 2.0 sccm, even down to 0.1 sccm, the plasma becomes unstable for standard apertures. Therefore, a custom-made quartz aperture has been attached to the discharge tube allowing for stabilisation of the oxygen plasma at very low gas flow rates. Due to the reduced diameter of the aperture holes, plasma stability and cracking efficiency are considerably increased in comparison with standard apertures. Low gas flow rates are necessary to establish growth conditions with very low oxidation power.

2.4 Rate monitoring

2.4.1 Technical aspects

Precise rate monitoring and rate control are vital for the co-evaporation of multiple sources, especially for e-beam evaporation. In the case of resistive heating of crucibles or boats, which are lesser affected by the chamber pressure, usually no rate monitoring or rate control is needed. The rate is determined mainly by source temperature. Sources are calibrated once, *in situ* by QCM or *ex situ* by, e.g., XRR, and are then operated at one given temperature representing one specific rate. In contrast, evaporation methods sensitively reacting to small changes in background pressure need rate monitoring and feedback-looped rate control to achieve defined rates during deposition. This holds especially for RMBE, as a reactant is introduced into the chamber with various flows resulting in considerable variations in deposition pressures. For e-beam evaporation with high evaporation flux, the chamber pressure has considerable influence on rate stability and extreme care and knowledge of the source behaviour is essential for achieving reliable rate stability. In addition, in MBE evaporation rates are often changed during deposition when, e.g., RHEED observations suggest such a change in evaporation rate.

For MBE, mainly three rate monitoring techniques are established, as there are quartz crystal microbalances (QCMs), electron emission impact spectroscopy (EIES), and atomic absorption spectroscopy (AAS). A detailed overview of state-of-the-art rate monitoring techniques is given in ref. [148]. As for this study only QCMs were used for *in situ* rate monitoring and rate control, the following description is limited to the basic principles of a QCM. The QCM consists of a piezoelectric quartz crystal sandwiched between a pair of electrodes, a monitor for rate and thickness measurement and a controller to automate the process.[149] If an oscillator is connected to both electrodes sandwiching the crystal and an alternating (AC) voltage is applied, the quartz crystal starts to oscillate at its resonance frequency due to the piezoelectric effect. As material is deposited on the crystal, the oscillation frequency changes, this correlates to the amount of added mass/film thickness, T_f. Equation 2.4.1 is known as the QCM thickness equation, where the AT-cut crystal constant is $N_q = 1.668\text{x}10^{13}$ Hz/m^{-10} and the density of quartz, D_q, equals 2.648 g/cm^3. D_m is the monitored material density, z the z-Factor, F_q the starting frequency and F_c the ending frequency after deposition. The z-Factor is used to match the acoustic impedance of the deposited material Z_m to that of the base quartz material ($Z_q = 8.83$) of the sensor crystal, according to z-Factor = z_q/z_m. z-Factors for most common materials can be found in literature supplied with a QCM system.

$$T_f = \frac{N_q D_q}{\pi D_m F_c z} \tan^{-1}\left[z \tan\frac{\pi(F_q - F_c)}{F_q}\right] \qquad \text{Eq. 2.1}$$

As a QCM sensor head cannot be mounted at the exact position of the substrate, the monitored thickness differs from real film thickness at substrate level. The tooling factor allows to calibrate monitored thickness in QCM to real film thickness at substrate level, either *in situ* by using a calibration crystal at substrate level, or *ex situ* by depositing a thin film whose thickness is determined by X-ray reflectivity. The change of mass or the increasing film thickness in time can be interpreted as a deposition rate, so the output of the rate and thickness monitor is used to control the input power of the e-beam sources and thus, their evaporation rates. Advantages of QCMs are their easiness in use and the broad monitorable materials variety. From the QCM principle it is obvious that crystal life is limited, as increasing mass decreases the oscillation frequency and at a certain accumulated mass the QCM fails. Regular QCM quartz crystal exchange is necessary; multiple sensor heads offer easy *in situ* QCM exchange avoiding the interruption of the growth procedure in case that the QCM fails during deposition. A disadvantage is the lack of materials selectivity, i.e., one crystal sensor cannot be used to control more than one source simultaneously. Therefore, each source needs one separate set of quartz crystal, oscillator, and monitor. A spatial separation of sources and corresponding QCMs is vital to reduce cross-talk between two QCMs. Collimators attached to the QCMs pointing towards one source only and shielding other sources can be helpful. The nonlinearity in frequency change with deposited mass onto the crystal, even if only one single material is deposited, leads to an increasing error in the monitored rate. This effect can be compensated by newer rate and thickness controllers, as they provide so-called auto-z options, which adapt the z-value as a function of increasing deposit on the QCM.

For this study, QCMs with single *AT*-cut crystals were used, mounted on a water cooled QCM head (MaxTecK) with custom-made collimators. They were located directly above the e-gun pockets. Rate and thicknesses were monitored by means of a rate thickness controller (Cygnus, Inficon) with a rate detection resolution of 0.001 Å/s. In addition, the rate thickness controller was used for fast responding, feedback-looped, and PID-optimised input power control of the e-guns.

2.4.2 Source calibration

Prior to film growth, a thickness calibration has to be conducted for all deposition sources, first *in situ* and then *ex situ*. For *in situ* calibration, the cooling shroud is filled with LN_2 and the calibration QCM is inserted at substrate level. The deposition controller, to which the calibration QCM and the corresponding source QCM are connected, has to be programmed according to the selected material specifications (density and z-value). The *in situ* calibration should be carried out at evaporation rates similar to later deposition rates, so growth conditions (growth pressure) are simulated as precisely as possible. The tooling factor has to be adjusted to accommodate for the difference in monitored evaporation rates at substrate level and at source QCM level.

After *in situ* calibration, *ex situ* calibration is executed by depositing a thin film of around 50 nm thickness, which is studied using XRR. The *ex situ* thickness determination allows to correlate monitored metal evaporation rates via QCMs with real oxide thin film thicknesses. This correlation factor allows targeting specific oxide film thicknesses using the monitored metal hafnium evaporation rate, vital when conducting thickness sensitive experiments. It is recommended to repeat *in situ* and *ex situ* calibration regularly, as the growth conditions may drift as a function of time. This drift can be due to a change in filling of the sources, different chamber pressure due to changed outgassing characteristics, or different chamber surface temperatures.

2.5 Growth monitoring

Besides monitoring thickness, deposition rate, chamber pressure, and substrate temperature, it is of high importance to get *in situ* information on film growth in terms of crystallinity, crystal structure, and film orientation. RHEED is commonly the method of choice covering the mentioned aspects. Complete RHEED systems are commercially available and relatively easy to integrate into existing UHV deposition systems. Nowadays, even high-pressure RHEED systems are available, which can be mounted on deposition systems utilising high background pressures (up to couple of millibars). This is achieved by separating the filaments with small apertures to the growth chamber, forming a separate compartment. This compartment is differentially pumped by a separate pumping system, establishing a dynamic pressure gradient from deposition chamber to filament compartment.

The principle of RHEED is the creation, acceleration, and focussing of electrons forming an electron beam incident on a substrate/film under a glancing angle. As RHEED is based on an electron beam striking the substrate under a glancing angle, RHEED can be used for *in situ* growth monitoring, which is a great advantage of RHEED over other surface sensitive spectroscopic techniques. The highly energetic electrons impinging on substrate/film surface allow diffraction with the crystal lattice under glancing incidence, providing information on the in-plane lattice parameters. The diffracted electrons can be imaged by a phosphor screen spatially opposing the RHEED gun, which is usually equipped with a CCD camera. Typical electron energies start at 10 keV and can range up to more than 50 keV providing access to a relatively large number of reciprocal lattice points due to a large Ewald sphere.

As RHEED is highly surface sensitive due to the low penetration depth of the electron beam, it provides information only of the very few top monolayers. This surface sensitivity gives a real-time feedback on the on-going crystal growth, and allows studying the change of growth conditions during run. Figure 2.8 demonstrates the origin of RHEED streaks, which indicates a well crystalline and smooth film growth on the substrate. Due to the relatively large Ewald sphere, not only one point in reciprocal space but a series along (in this case) h is brought into diffraction. From the distance x between two streaks, the wavelength λ of the e-beam, and the distance between sample and phosphor screen, L, the corresponding in-plane d-spacing can be calculated following $d_{hkl} = \lambda \cdot L/x$. Besides the determination of d-spacings by streak distances, changes in RHEED intensity of one RHEED streak can give information on

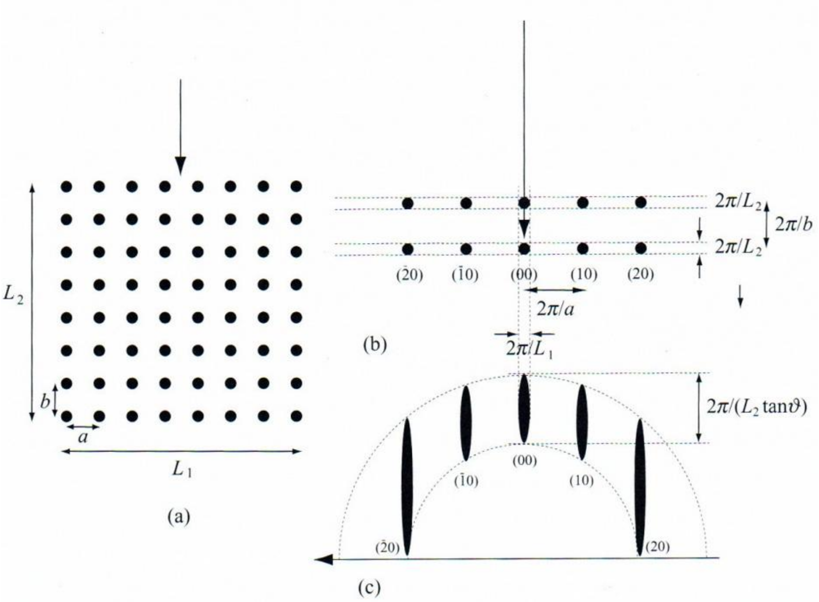

Fig. 2.8: Schematic of the origin of RHEED streaks. (a) Crystal lattice with dimensions L_1 and L_2, corresponding lattice constants a and b and incident primary electron beam (arrow); (b) corresponding reciprocal lattice for (a); (c) the RHEED construction for (b), streak length depends on the glancing angle of incidence ϑ. Taken from ref. [151].

film growth mode and film thickness. In the case of Frank-van-der-Merwe growth mode (layer-by-layer growth), surface roughness changes as a function of the completion of one monolayer. Considering a fully completed monolayer (maximum RHEED intensity), additional atoms adsorbed on film surface increase film roughness (RHEED intensity decreases). The decrease in intensity stops at a coverage of about 50% of adsorbed atoms needed to form one monolayer (minimum RHEED intensity). With further increasing amount of adsorbed atoms, RHEED intensity increases again, until the next maximum for full coverage is reached. In consequence, one RHEED oscillation may represent one monolayer. This qualifies RHEED for rate monitoring and, thus, compositional control.[150] The amplitude of RHEED oscillations is highly sensitive to the incident angle of the electron beam with respect to the substrate. This sensitivity could lead to the situation that no RHEED oscillations are observed, although clean layer-by-layer growth takes place.

A more elaborate discussion of the theoretical background on the principles of RHEED and its unique capabilities can be found in textbooks, see ref. [151, 152]. For the present study, a differentially pumped RHEED from Vieetech (e-gun VE-052S, controller VP-052S) with a phosphor screen, CCD camera, and ksa 400 analysis software (*k*-Space Associates) has been utilised. Acceleration voltages were kept between 25 to 30 keV at emission currents of around 60 μA.

2.6 Growth procedure

Once source thickness calibrations are finished, the sample has been pasted on a substrate holder and transferred into the growth chamber, and the cooling shroud has been filled with LN_2, growth procedure starts with substrate heating. Substrates are heated in two steps, first up to 300 °C with 100 °C per minute and a dwell time of five minutes to allow degassing of solvents and other adsorbed species during exposure to atmosphere. Second, deposition temperature, T_s, is ramped with 100 °C per minute. In case that T_s is lower than 300 °C (degassing temperature), the substrate is cooled down after degassing. In the case of oxide substrates it is preferred to introduce oxygen during heating to (i) clean the surface and (ii) prevent sample reduction due to vacuum annealing. Once T_s is reached, the main shutter is closed, the radical source is started and adjusted to the desired rf-power & gas flow, and the e-guns are started subsequently. Slow heating of the target material reduces rate fluctuations. After all sources have been started, a settling time of ∼10 minutes is given allowing a stabilisation of the evaporation rates and allowing the system to reach thermodynamic equilibrium. A settling time at growth conditions is essential to obey reproducible film growth, as hafnium metal is highly reducing and reacts with the provided oxygen radicals resulting in chamber pressure fluctuations when changing the hafnium flux or the oxygen flow rate.

After film thickness has reached targeted thickness, the shutter is closed and the film has to be cooled down according to a specific cooling procedure. In the case of oxide thin films, the cooling procedure determines film surface termination, which is important when growing films with oxygen deficiency. Therefore, for oxygen deficient films it is useful allowing the sample to cool below 100 °C in UHV to avoid surface oxidation. This is achieved by first switching off the radical source and stopping the gas flow prior to switching off the hafnium source, so the evaporated metal hafnium reacts with excess oxygen in the growth chamber. Before removing the cooled sample from the load lock chamber, partial venting of the load lock chamber with nitrogen leads to the formation of an adsorbed nitrogen layer on the sample surface. The adsorbed nitrogen hinders direct oxidation of the sample surface after exposing it to air, ensuring that silver pads deposited on the film directly after removing the sample from the load lock chamber are in contact with reduced hafnia. When growing stoichiometric thin films of hafnium oxide, the hafnium flux has to be terminated first and then the film has to be cooled down below 100 °C under continuous oxygen flow to avoid any kinds of UHV annealing effects at elevated temperatures.

3 Characterisation techniques

This section presents main characterisation techniques which have been applied for this study. Each section gives a brief insight into theoretical background, followed by the description of why and how this technique was adopted for this study. However, not all characterisation techniques are described, and each description is kept short. For each technique, references for basic literature are given.

3.1 X-ray measurements

Generally the interaction of condensed matter with X-ray radiation is the basis of numerous spectroscopic methods. For thin film growth, one of the first (usually *ex situ*) characterisation tools of choice are X-ray diffraction and X-ray reflectivity. This section focuses on the description of the specific measurement setups and procedures with their advantages, disadvantages, and challenges, all specific to measurements carried out for this study. For extensive theoretical background, please see ref. [153-157].

X-ray diffraction

X-ray diffraction describes the physical process of interaction of short wavelength radiation with the electronic structure of periodic lattices in a condensed solid. Besides absorption according to Lambert Beer's law [$I = I_0 \exp(-\mu d)$], where I is the radiation intensity after passing the solid by a distance d, μ the linear absorption coefficient, and I_0 the primary intensity, diffraction describes the modulation of the incident wave vector $\vec{k}$ by the crystal lattice. An incident beam striking an electron modulates its energetic state due to the interaction of the electromagnetic potentials. This interaction evokes the irradiation of a beam with same impulse but different direction, $\overrightarrow{k'}$, modulated by the reciprocal space vector $\vec{G}$. The absolute value of $\left|(\overrightarrow{k'})\right|$ is maximum when $\overrightarrow{k'} = \vec{k} - \overrightarrow{k'} = \vec{G}$ is fulfilled, only then diffraction occurs, see Fig. 3.1 (a). The incident beam is represented by $\vec{k}$, its direction depends on the incident beam angle θ in real space, whereas the absolute value $\left|(\overrightarrow{k'})\right|$ is determined by the radiation wavelength λ. A circle with radius $\vec{k}$ is drawn around C to check for diffraction at specific incident angles θ, as illustrated in Fig. 3.1 (b). All points in reciprocal space are representing different sets of lattice planes (reflections); all reciprocal points which are cut by the Ewald

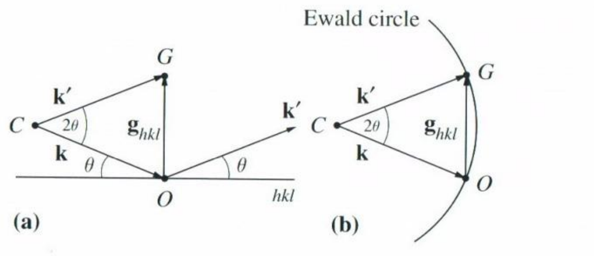

Fig. 3.1: (a) Visualisation of incident beam *k*, diffracted beam *k'*, and reciprocal space vector g_{hkl} , (b) Schematic of the Ewald sphere, constructed around *C* cutting the origin *O* and *G* in reciprocal space. Taken from ref. [155].

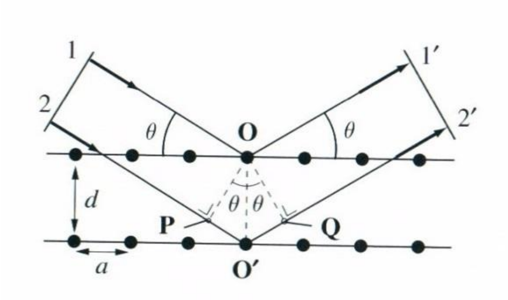

Fig. 3.2: Schematic of two beams incident on two parallel lattice plains separated by d. Constructive interference of diffracted beams 1' and 2' occurs when $\overline{PO'Q}$ equals $n\lambda$. Taken from ref. [155].

sphere allow for diffraction and thus can be identified in the diffraction pattern. Rotating the Ewald sphere by 360° around C describes a limiting sphere, which includes all reflections which can be brought into diffraction with a given wavelength λ. The formalism connecting the incident angle, θ, the X-ray wavelength, λ, the diffraction order, n, and the lattice constant, d is known as Bragg's equation, see eq. 3.1 and Fig. 3.2. Constructive interference of diffracted beams 1' and 2' takes place when $\overline{PO'Q}$ equals $n\lambda$.

$$2d_{hkl}\sin\theta = n\lambda \qquad \text{Eq. 3.1}$$

Diffraction can only take place in the case of condensed solids with periodic lattices having a long-range order. Solids with short range ordering or no ordering at all are not sensitive to diffraction but can be subject to diffuse scattering. Bragg's law is the fundamental basis describing X-ray diffraction, allowing for the determination of lattice constants of crystalline films. A change in lattice constant or a change in crystal symmetry can occur due to a change in film stoichiometry, thus X-ray studies are often used for thin film growth optimisation. Principally 2θ–θ measurements can be performed in three different arrangements, (i) out-of-plane for the investigation of lattice planes parallel to film surface, (ii) in-plane for lattice planes perpendicular to film surface, and (iii) mixed out-of-plane and in-plane for lattice planes being neither parallel nor perpendicular to sample surface. Only the observation of two linearly independent reflections allows a complete determination of crystal structure and film orientation with respect to the substrate. In addition to lattice constant determination, rocking curves (ω–scans) allow predictions on the grade of crystal orientation for polycrystalline films, film mosaicity, and dislocation density for textured films. The lower the FWHM of the Bragg reflection of a ω–scan is, the higher film mosaicity. The higher the broad portion of a ω–scan is, the higher the dislocation density in the film. When the dislocation density reaches a critical value, the Bragg reflection vanishes visualising film relaxation by the formation of grain boundaries.

For this study, symmetrical out-of-plane and in-plane 2θ–θ measurements were performed using a Rigaku SmartLab X-ray diffractometer with CuK_α-radiation. Figure 3.3 shows a scheme of the utilised diffractometer, naming most degrees of freedom available for measurement and sample manipulation. For all measurements parallel beam geometry was chosen, realised by an X-ray mirror for beam parallelisation and primary monochromatisation. For further monochromatisation and, thus, increasing resolution, a secondary graphite monochromator in flat mode including K_β–slit has been mounted prior to the scintillation counter on the secondary optics arm. For high-resolution measurements, a primary Ge(220) channel-cut monochromator has been utilised instead of the secondary graphite monochromator. As

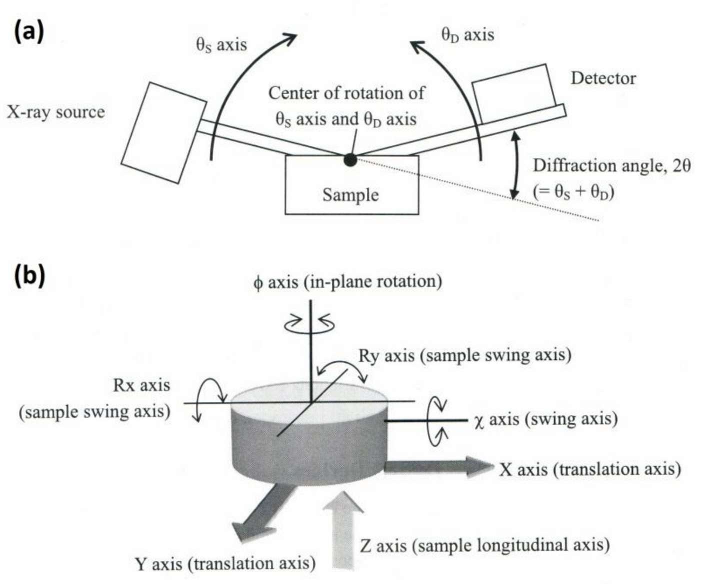

Fig. 3.3: (a) Principle of the Rigaku SmartLab θ–θ goniometer arrangement, (b) degrees of freedom for sample manipulation. Taken from Rigaku educational material.

the utilised diffractometer is based on a hanging five-circle θ–θ goniometer, no sample fixation is needed for most 2θ–θ measurements.

For X-ray measurements of thin films, sample alignment is crucial. Considering a (00*l*)-oriented single crystalline substrate with an epitaxial, (00*l*)-oriented film on top, the sample has to be aligned precisely with respect to the goniometer centre. All single crystalline substrates do have a certain miscut, although it might be very small. A miscut denotes to a non-zero angle between sample surface normal and lattice plane normal. In the case of a (00*l*) oriented film on a (00*l*)-oriented substrate, this miscut results in lattice plane normals of substrate and film, which are not exactly perpendicular to the horizontal goniometer centre plane. As a perfectly aligned measurement setup (without sample) is usually configured to measure symmetrically to the vertical goniometer centre plane, no reflections for lattice plane normals being *not* perpendicular to the horizontal goniometer plane are observable. The sample has to be aligned in such a way that the lattice plane normal of the single crystal substrate or of the film is exactly perpendicular to the horizontal goniometer centre plane. To do so, it is not sufficient to align according to the sample surface via the direct beam half-cut alignment procedure. For lattice plane normal alignment, subsequent ω–scans, z-scans, and for large area samples χ–scans are performed, while the diffraction angle is kept constant. In the case of a (00*l*)-oriented substrate, 2θ is usually set to the corresponding (00*l*) substrate reflection with highest intensity. Alignment with respect to the strongest film reflection instead of the substrate reflection is necessary for highly oriented and well crystalline films that grow tilted with respect to the substrate lattice planes. In the case of textured hafnium oxide thin films on *c*-cut sapphire, alignment with respect to the substrate was performed, whereas for the in-plane measurements alignment with respect to the film reflection was executed.

In-plane sample alignment differs to out-of-plane sample alignment by adding subsequent R_x and R_y scans of the substrate reflection after the standard out-of-plane alignment to set the out-of-plane lattice plane normal parallel to the phi rotation axis of the goniometer. In-plane measurements, which represent $2\theta\chi$-phi scans perpendicular to the sample surface, require a

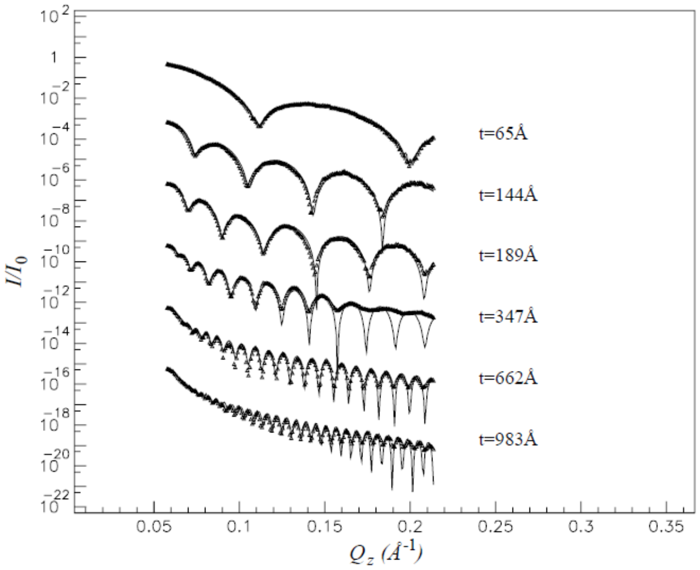

Fig. 3.4: Exemplary X-ray reflectivity patterns for various thin Molybdenum films; solid lines are data fits. Note that the intensity oscillation period decreases linearly with increasing film thickness. Taken from ref. [158].

precise alignment of the out-of-plane lattice plane normal parallel to the phi axis, as otherwise phi scans would lead to a precision of the out-of-plane lattice plane normal around the phi axis. In such cases the chance of missing in-plane reflections is very high.

X-ray reflectivity

X-ray reflectivity is the method of choice to quickly and accurately determine thin film thicknesses in the Angstrom range up to more than 200 nm, depending on film quality. Besides film thickness, comprehensive X-ray reflectivity studies can give information on film surface roughness, interface roughness, and film density. This holds for multilayers of thin films, provided that the interfaces are smooth enough and that the corresponding refractive indices differ sufficiently.

The principle of X-ray reflectivity is the reflection of incident X-rays below the critical angle ϑ_c. Due to the difference in optical path of beams reflected at sample surface and film interface, interference can take place in a similar way as known for Hygens' principle. The consequence is the occurrence of intensity oscillations (fringes) in the reflectivity pattern. Amplitude scales with interface roughness, period with film thickness, and damping with surface roughness. The total reflection angle itself is a function of the material's optical density. The higher the electron density, the higher the optical density of condensed matter for X-rays, the larger the total reflection angle is. Figure 3.4 shows exemplarily a reflectivity pattern taken from ref. [158].

For obtaining reliable reflectivity data, proper sample alignment is crucial. In the case of reflectivity measurements, the alignment is carried out with respect to the surface normal in contrast to the alignment with respect to the lattice plane normal. To do so, subsequent ω–scans and z-scans are performed at a fixed 2θ, which is chosen to be well below the total reflection angle. This ensures the parallel alignment of the sample surface and thus the film to

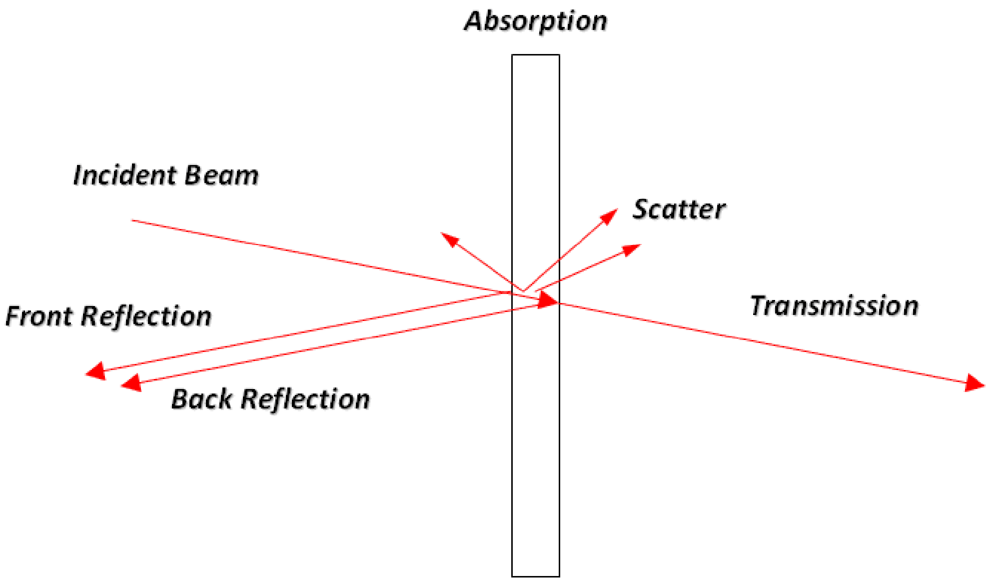

Fig. 3.5: Schematic of the processes occurring in an optical absorption experiment. Taken from Perkin Elmer advertising material.

the goniometer centre plane. Reflectivity pattern evaluation is usually carried out by simulating and fitting reflectivity curves utilising commercially available software, e.g., GXRR from Rigaku or RefSim from P. Zaumseil. From the fitting parameters, film thickness, film density, interface roughness, and surface roughness can be extracted. In the case of interfacial layer formation with interdiffusion (no sharp interface) or thin films with density gradients, simulation and fitting can be challenging. However, film thickness can be extracted from reflectivity patterns without simulating and fitting, just by diffraction-corrected Fourier-transformation of the observed intensity oscillations.

3.2 Optical absorption spectroscopy

Optical absorption spectroscopy is a characterisation method based on the absorption of radiation by the irradiated sample. For this study, optical absorption spectroscopy has been applied in transmission geometry using a PERKIN ELMER Lambda 900 photospectrometer. Figure 3.5 depicts a schematic of occurring processes in an optical absorption experiment. Primary radiation wavelength was varied from 175 up to 2,000 nm using a tungsten-halogen lamp and a deuterium lamp for sample irradiation, and a holographic grating monochromator to tune the wavelength. The sample chamber was flushed continuously with nitrogen to reduce strong absorption and emissions in the UV-range due to interaction with molecular oxygen and water vapour (below 200 nm). The absorbed radiation A follows the equation $A = 1 - T - R$, where T denotes to the transmitted and R to the reflected portions. This measurement setup prompts for the need of measuring either in a dual beam configuration utilising an internal standard, or by obtaining a calibration curve with an external standard, as the reflected portion usually cannot be accurately determined. In the present study, an external standard (bare substrate) has been used allowing obtaining a calibration curve prior to sample measurement. As the transmitted portion does usually not fulfil Lamberts' rule, an integrating sphere is located directly behind the sample allowing the collection of all transmitted light, regardless of its direction, thus enabling corrected intensity integration. In the case of hafnium oxide thin films, the interaction of radiation (175 – 2,000 nm) with the thin film is based on the excitation of electrons from occupied states into vacant states allowing probing the optical band gap. The radiation attenuation I/I_0 can be described by the following equation,

$$\frac{I}{I_0} = \frac{(1-R)^2 exp(-\alpha t)}{1-R^2 exp(-2\alpha t)} \qquad \text{Eq. 3.2}$$

where I is the transmitted intensity, I_0 the primary intensity, α the absorption coefficient, and t the irradiated material thickness.[159] The optical band gap can be determined by plotting the square of the absorption coefficient, α,^{2} vs. the radiation energy, E, following the relation $\alpha \propto \sqrt{E - E_g}$ where $E = h\nu = hc/\lambda$ (Planck's constant $h = 4.136 \text{ x } 10^{-15}$ eVs).[160] By extrapolating the linear portion of the α^2 vs. radiation energy plot, the optical band gap can be determined assuming direct band gap, parabolic valence & conduction bands. Since the wavelength of the applied radiation is in the same range as film thickness, and due to phononic excitations, usually transmission oscillations (interferences, fringes) can be observed. When the transmitted portion becomes significantly low, measurement accuracy decreases as the signal to noise ratio decreases drastically. The examined film thicknesses should be accounted to sufficient transparency for a good signal to noise ratio to avoid too little transmission.

3.3 Resistivity and Hall measurements

Electrical resistivity is a measure for the magnitude of an applied voltage to a specimen in order to pass a defined current, whereas the Hall effect, discovered in 1879 by Edwin H. Hall, describes the appearance of a small voltage across a current-carrying specimen in an applied magnetic field. This voltage is proportional to the passed current density, the magnetic flux, the charge carrier concentration, and the charge carrier mobility. For theoretical background on electrical resistivity and Hall effect, please see ref. [161, 162].

As film resistivity and Hall coefficient do deliver very basic and important information on electrical film properties, several measurement setups had to be designed and adopted to allow thin film measurements with various currents, at various temperatures, and under various magnetic fields. The goal was to ease up sample preparation prior to measurement, sample processing, and ensuring sufficient measurement accuracy. Designing sample measurement setups for low current – low voltage measurements under magnetic field and for low temperature measurements, a lot of aspects have to be addressed. These aspects cover, e.g., low thermal conductivity of the utilised electrical wires, wire pair twisting to minimise inductance by magnetic field change, and good thermal contacting of the sample. A good overview about techniques for electrical measurements at low temperature is given by J. W. Ekin, see ref. [163].

The four-probe or Kelvin technique in combination with van der Pauw geometry is the method of choice for obtaining accurate (Hall) voltages. Van der Pauw geometry describes the arrangement of contacts as shown in Fig. 3.6 (a) (by courtesy of Gabi Haindl) in order to obtain resistivity values of flat samples, provided, (i) the contacts are in the circumference of the sample, (ii) the contacts are sufficiently small, (iii) the sample is homogeneous in thickness, and (iv) the surface of the sample does not have isolated holes.[164, 165] Compared to two-probe

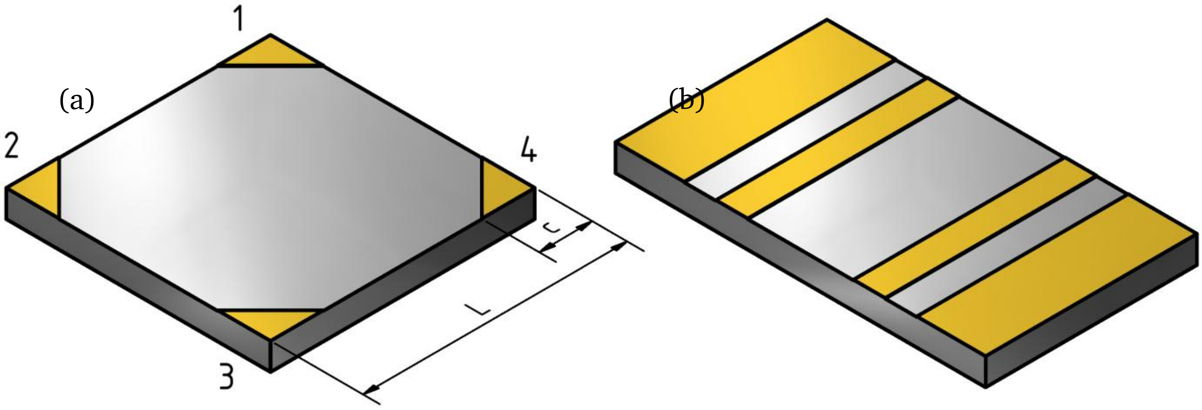

Fig. 3.6: (a) schematic of a 5 x 5 mm² sample (L = 5 mm) with counter-clockwise numbered electrical contacts on top (c = 1 mm) in van der Pauw geometry, (b) 7 x 7 mm² sample with silver pads in bar geometry.

techniques, the four-probe technique separates contacts needed for passing a current through a specimen from contacts needed for measuring voltages. This eliminates measurement errors due to probe resistance, spreading resistance under each probe, and contact resistance. When using a high impedance voltmeter, the current needed for measuring the voltage is extreme low, thus the voltage drops mainly across the sample. This is of special importance for Hall voltages, which can be in the range of some nanovolts in the case of thin films.

Fig. 3.7 (by courtesy of Gabi Haindl) shows three sample holders which have been designed for this study, (a) for 5 x 5 mm² samples, (b) for 7 x 4 mm² samples; both can be inserted into a Cryostat with temperature and magnetic field control, and (c) for 5 x 5 mm² samples to be inserted into a MPMS from Quantum Design. Prior to measurement silver pads have been thermally evaporated on the sample top using stainless-steel laser-cut masks to ensure proper contacting. Two measurement (silver pad) geometries were used, van der Pauw for 5 x 5 mm² samples (see Fig. 3.6 (a)) and bar geometry for 7 x 4 mm² samples (see Fig. 3.6 (b), by courtesy of Gabi Haindl). Sample contacting was achieved by means of custom-made push pins (non-magnetic, gold coated, through-piston configuration), which allow (i) accommodation of thickness dilatation during sample heating and cooling, (ii) non-destructive contacting, and (iii) easy sample mounting. Low voltage noise measurements down to a few tens of nV could be realised, influences of the magnetic field to the measurement circuit were minimised. A Keithley 6221 DC and AC Current Source, and a Keithley 2182A Nanovoltmeter were utilised for resistivity and Hall measurements. Both instruments were connected to a Keithley 7001 Switch System with a 7065 Hall Effect Card. The measurement setup push pins were wired to the Hall Effect Card via Triax cables to reduce losses and external voltage pick-up (due to alternating stray electric and magnetic fields) as much as possible. The switch system allows alternating all four sample contacts to any in- or output from the current source and nanovoltmeter during measurement. Measurement currents were in the μV range, whereas obtained voltages ranged from nanovolts up to millivolts. Temperature and magnetic field control were ensured by the control software of the corresponding devices (Cryostat, MPMS).

The subsequent measurement of the Hall voltage and the electrical resistance (for later determination of the sheet resistance) utilising van der Pauw geometry allows to calculate the Hall coefficient, R_H (cm³/C), the charge carrier concentration, n_s/p_s (cm^{-3}) for electrons and holes, respectively, and the charge carrier mobility, μ (cm²/Vs). To do so, one has to obtain in total eight voltages for sheet resistivity determination (V_1 to V_8) by passing a current through the sample using a pair of neighbouring contacts ($I_{1\rightarrow 2}$, see scheme in Fig. 3.6 (a), by courtesy

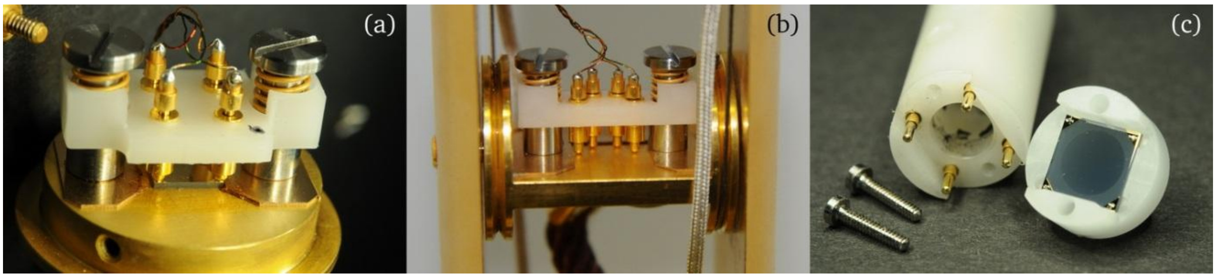

Fig. 3.7: Custom-designed sample holders for resistivity and Hall-measurements. (a) For 5 x 5 mm² for cryostat insertion; (b) for 7 x 4 mm², sample tilting up to 90°, for cryostat insertion; (c) for 5 x 5 mm², for MPMS insertion.

of Gabi Haindl) and measuring the voltage using the corresponding pair of contacts ($V_{4\rightarrow 3}$). Reversing polarity for each pair ($I_{2\rightarrow 1}$, $V_{3\rightarrow 4}$), and alternating current/voltage pairs ($I_{4\rightarrow 3}$, $V_{1\rightarrow 2}$; $I_{3\rightarrow 4}$, $V_{2\rightarrow 1}$; $I_{2\rightarrow 3}$, $V_{1\rightarrow 4}$; $I_{3\rightarrow 2}$, $V_{4\rightarrow 1}$) result in eight different voltages. The determination of two quality factors, Q_A and Q_B, by $Q_A=(V_2-V_1)/(V_4-V_3)$ and $Q_B=(V_6-V_5)/(V_8-V_7)$ allows to check for sample homogeneity. Q_A and Q_B should not differ by more than three per cent, otherwise the measured sample is inhomogeneous in between contacts or the measurement geometry is not symmetric due to misalignment of the mask during contact pad evaporation. From the obtained voltages, two sheet resistances, ρ_A and ρ_B, can be derived following Eq. 3.3 and 3.4,

$$\rho_A = \frac{\pi f_A t}{ln(2)}\left\{\frac{V_2+V_4-V_1-V_3}{4I}\right\} \qquad \text{Eq. 3.3}$$

$$\rho_B = \frac{\pi f_B t}{ln(2)}\left\{\frac{V_6+V_8-V_5-V_7}{4I}\right\} \qquad \text{Eq. 3.4}$$

where t denotes to film thickness and f_A and f_B are geometrical factors. These factors are set to one in both cases, as the difference in pad geometry is minimal due to the CAD-based laser cutting of the corresponding masks. The final sheet resistance ρ is determined by averaging between ρ_A and ρ_B. The Hall coefficient is determined according to Eq. 3.5, where m is the slope obtained from a linear fit to a plot of the measured Hall voltage vs. the magnetic field. The carrier concentration is given by $n_s/p_s = 1/(q\cdot R_H)$ where q is the elementary charge ($1.602\cdot 10^{-19}$ C), whereas the mobility is derived by Eq. 3.6.

$$R_H = 10^8 \frac{t}{I} m \qquad \text{Eq. 3.5}$$

$$\mu = \frac{1}{q n_s p_s \rho} \qquad \text{Eq. 3.6}$$

Although extreme care was taken in designing the measurement setup to allow as accurate measurements as possible, various sources of error may occur, which are described in detail by Look.[166] Summarising his findings, the resistivity correction factor $\Delta\rho/\rho$ for square structures in van der Pauw geometry is roughly proportional to $(c/L)^2$ (see Fig. 3.6 (a), by courtesy of Gabi Haindl), whereas the Hall correction factor $\Delta R_H/R_H$ is proportional to (c/L). In the present study $c = 1.0$ mm and $L = 5$ mm, leading to $\Delta\rho/\rho = 4\%$, and $\Delta R_H/R_H = 20\%$. The importance of correct contact geometry, contact symmetry, and location of contacts for Hall measurements has been investigated by Bierwagen *et al.*, demonstrating that it is necessary to place symmetric van der Pauw contacts on sample corners, instead of placing them in the inner sample.[167]

Alternatively, a fourth setup for pure resistivity determination was used, which allows to contact 5 x 5 mm² and 7 x 4 mm² samples with silver pads in bar geometry (see Fig. 3.6 (b), by courtesy of Gabi Haindl). This measurement setup is placed on top of a copper measurement stick, which can be inserted into a liquid helium dewar. Temperature measurement is achieved by means of a calibrated silicon diode (lakeshore DT-670D-SD), whereas temperature is varied by the insertion depth of the measurement stick into the liquid helium dewar. For this setup it was not possible to switch arbitrarily source and voltmeter in- and outputs between all four contacts. However, the reverse current method has been applied to cancel thermo-electrical effects due to different materials contacted in series at different temperatures. Eq. 3.7 summarises how film resistivity is determined as a function of the measured voltages obtained for both polarities, U_1 and U_2, the applied current, I, film cross section, A, and the distance between the inner two contacts, l. For the current setup, $l = 2$ mm.

$$\rho = \frac{\left|\frac{(U_1+U_2)}{2}\right| \cdot A}{I \cdot l} \qquad \text{Eq. 3.7}$$

3.4 Secondary ion mass spectrometry

A more detailed theoretical description of secondary ion mass spectrometry and its applications can be found in ref. [168-170]. SIMS is a highly sensitive tool for qualitative analysis of solid specimen by sputtering its surface with ions and analysing the secondary ions ejected due to energy and momentum transfer. Primary ions are in the energy range of 1 – 25 keV. The utilised Cameca ims5f SIMS utilises two different sources for primary ions, O^- ions created in a Duoplasmatron (used for detection of electronegative elements), and Cs^+ ions from a caesium ion source (used for detection of electropositive elements). The primary ions incident on sample surface eject neutral particles which can get charged, dependent on the primary ion charge. The intensity of the ejected secondary ion beam $I_{^{n}A}$ of the isotope ^{n}A can be described by eq. 3.4.1, with the primary ion intensity, I_P, the sputter rate, S, the positive or negative probability of ionisation, $a_A^{\pm}$, the atomic concentration of the element in the sputtered volume fraction, A, the isotopic abundance, $f_{^{n}A}$, and the transmission of the mass spectrometer, η.

$$I_{^{n}A} = I_P \, S \, a_A^{\pm} \, c_A \, f_{^{n}A} \, \eta \qquad \text{Eq. 3.7}$$

Ejected secondary ions are collected and accelerated into a mass spectrometer by a small grid voltage. The mass spectrometer consists of an electrostatic and magnetic filter, which allows to fraction the secondary ions as a function of the product of mass and charge (resolution $m/\Delta m$ up to 25,000). Detection is achieved by means of a channel plate for two-dimensional element distribution images, or by an electron multiplier with subsequent Faraday cup for single element detection, as depicted in Fig. 3.8. SIMS can be operated in two modes: static mode for pure surface analysis without disturbance of the specimen, and dynamic mode for depth profiling utilising the sputtering effect of the primary ions. It is a highly surface sensitive analysis tool, since secondary ions are ejected only from the top three monolayers (lateral resolution is in the sub-micron range). However, lattice disturbance due to mixing effects during sputtering reduces depth resolution, preferential sputtering effects can lead to the accumulation of certain elements in the sputtered area suggesting false elemental depth profiles. For qualitative analysis down to the ppb-range, SIMS is the method of choice. Quantitative analysis is much more challenging due to matrix effects, although they are considered

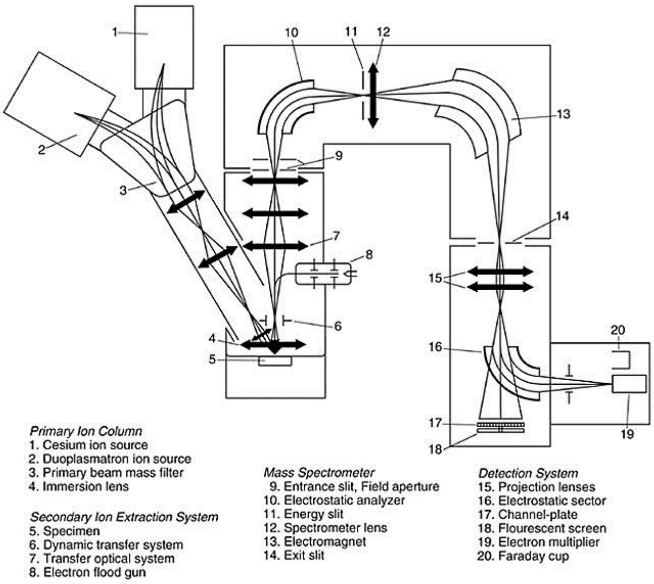

Fig. 3.8: Scheme of a Cameca ims5f SIMS. Taken from Cameca advertising material.

using relative sensitivity factors obtained from reference samples. This brings us to the limitations of SIMS, as for many specimen no reference samples are available. In this case, SIMS allows only relative concentration comparisons between samples with similar matrices. However, the combination of SIMS with an absolute spectroscopic method, e.g., Rutherford backscattering spectroscopy, allows quantitative elemental concentration analysis, as in this case RBS provides absolute elemental concentrations of the used standards. As evident from its operation principle, samples have to be UHV-proof and conductive to avoid charging effects. Hafnium oxide thin films on sapphire substrates, which are insulating in the case of stoichiometric composition, can only be analysed utilising a fine gold mesh put on sample surface to avoid the formation of charge clouds.

3.5 Atomic force microscopy

Atomic force microscopy is a versatile tool for easy and non-destructive surface investigation, giving real three-dimensional information on sample topography. The main advantages of AFM are its topographical resolution allowing imaging, measuring, and manipulating solid matter down to atomic scale, its easiness in sample preparation (works under atmospheric conditions), its insensitivity to sample conductance, and its relative technical simplicity. Newer systems allow to measure electric and magnetic potential of surfaces, it is even possible to probe local conductivities by passing currents through the cantilever.[171] A good general overview about applied AFM can be found in ref. [172].

Basic principle is to bring a Si or SiN-based cantilever (probe) with a sharp tip on top in contact with matter and to move the probe across the sample surface by piezoelectric actuators. Piezoelectric transducers allow extreme precise movements of either sample (indirect scanning) or cantilever (direct scanning) with accuracies in the sub-nm range. When scanning the probe across the sample surface, the cantilever is moved vertically with respect to the sample according to surface topology or due to interaction with interatomic forces of any nature. For AFM, two measurement modes are distinguished, contact mode and non-contact

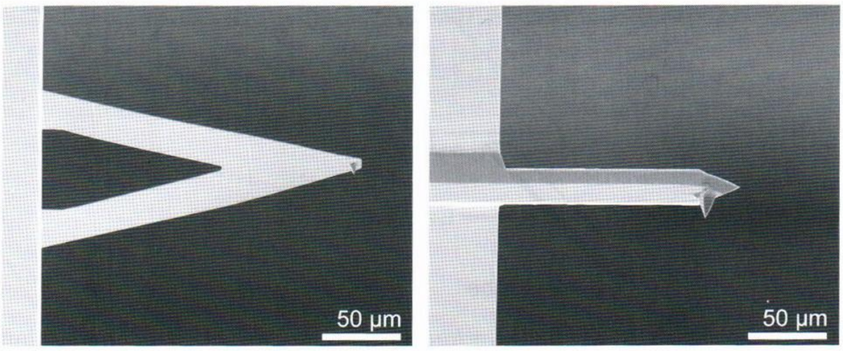

Fig. 3.9: Examples for AFM tips. Left: typical v-shaped contact-mode cantilever. Right: Rectangular, non-contact mode cantilver for oscillation-based techniques. Taken from ref. [172].

mode. Both techniques require different cantilever design, Fig. 3.9 shows a typical V-shaped contact-mode cantilever (left) and a rectangular non-contact mode (oscillation mode) cantilever made of silicon, which is much stiffer but more likely to break (right). In contact mode, the cantilever is literally touching sample surface, while a force transducer keeps the force necessary to contact the sample constant during scanning time by moving the cantilever towards or away from sample surface. Measuring the cantilever movement can be realised by optical lever sensors, which utilise a laser beam pointing on the back side of the lever. When the lever moves, the reflected laser beam changes its spot position on a small area detector. As the distance cantilever-detector is large, a small movement of the cantilever results in a well-measureable movement of the laser reflection on the area detector. In non-contact mode, the cantilever oscillates near its resonance frequency or the first higher harmonic in a short distance (some nm) above the sample surface. Long range forces like ionic forces or van-der-Waals forces damp the oscillation frequency, which can be interpreted as a change in surface topography. As common to all microscopic techniques, image artefacts may occur, especially for very smooth sample surfaces. Stripe shaped parallel features obtained for such surfaces can be caused by poor tips, any sources of noise affecting the measurement, or surface charge effects when measuring in non-contact mode. Image verification by re-measuring the same surface area under different scanning vectors, e.g., from left – right to top – bottom, is vital for extracting reliable surface roughnesses. For this study, an AFM MFP-3D Stand Alone AFM (Asylum Research) has been used.

3.6 Transmission electron microscopy

Transmission electron microscopy is among the most important microscopical tools to investigate thin crystalline films in terms of crystallinity, crystal structure, grain size and shape, film/grain interface characteristics (shape, thickness, composition, etc.), epitaxial relation, and so forth. Transmission electron microscopes are technically highly sophisticated, very expensive, and correct data collection and interpretation can be very challenging and prompts for experienced experts operating TEMs and analysing TEM data. As a detailed description of the principles of TEM is beyond the scope of this study, please see ref. [173]. For this study, an FEI CM20 TEM with a LaB_6 cathode, EDX detector, and cooled double tilting stage has been used. In the following, a brief overview of the utilised TEM techniques for this study is given.

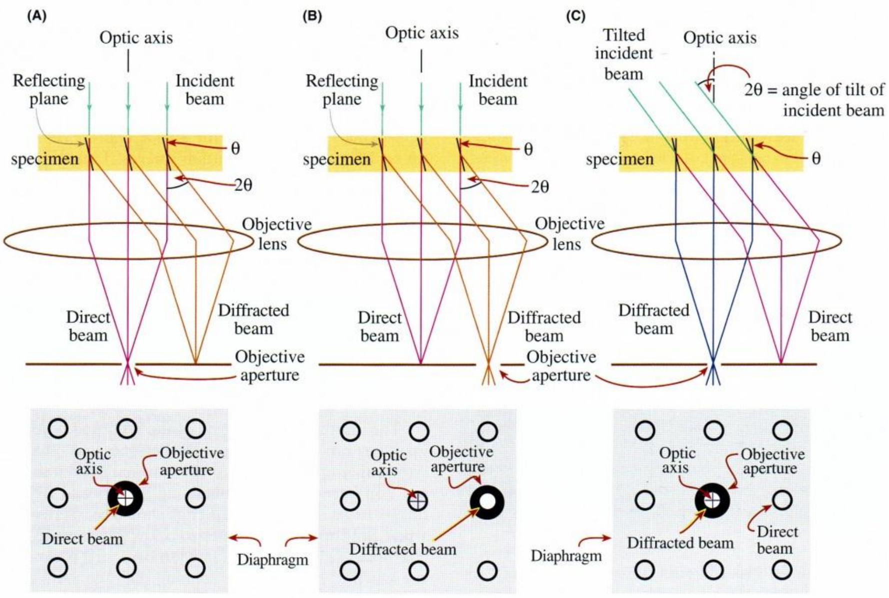

Fig. 3.10: Three main imaging modes of TEM, (a) bright-field (BF) images, (b) displaced-aperture dark-field (DF) images, and (c) centred dark-field images. Below the corresponding diffraction patterns which would be obtained on a phosphor screen below the objective aperture. Taken from ref. [173].

The principal of TEM is the irradiation of a specimen by electrons in transmission geometry and the later detection of transmitted or diffracted electrons by (nowadays) CCD arrays. There are mainly three different imaging modes, as displayed in Fig. 3.10, (a) bright-field (BF) images are collected from the direct electron beam, (b) displaced-aperture dark-field (DF) images are collected by an off-axis scattered beam, and (c) centred dark-field images are obtained for a tilted incident beam, so that the diffracted beam passes the aperture on-axis. Corresponding areas of the diffraction pattern, which could be displayed on a phosphor screen below the objective aperture, are shown below the ray schemes of Fig. 3.10.

For this study, Fourier-transformed phase contrast images have been obtained by collecting several beams (see Fig. 3.10, in which only one beam is collected), which form a phase contrast image after Fourier transformation, allowing the collection of images with atomic resolution. Phase contrast TEM is often named HRTEM, as its resolution is higher than what is obtained for images taken under BF or DF. From atomically resolved images, atomic spacings of individual grains and atomic symmetry can be derived, which in the case of $HfO_{2\pm x}$ thin films can give information on whether atomic distances change as a function oxygen deficiency. BF panoramic images with lower resolution allow determining the ratio of crystalline to amorphous matter, grain shape, grain size and orientation, and the determination of the crystal structure of individual grains.

3.7 Superconducting quantum interference device

Nowadays, magnetic properties of thin film samples are often obtained by utilising a magnetic property measurement system (MPMS) equipped with a superconducting quantum interference device (SQUID). A SQUID magnetometer allows to measure extreme low changes in magnetic flux, if being well configured, down to one single flux quantum. There are in principle two types of SQUIDs available, rf- and dc-SQUIDs. Rf-SQUIDs consist of a superconducting loop with one Josephson junction, whereas dc-SQUIDs consist of a superconducting

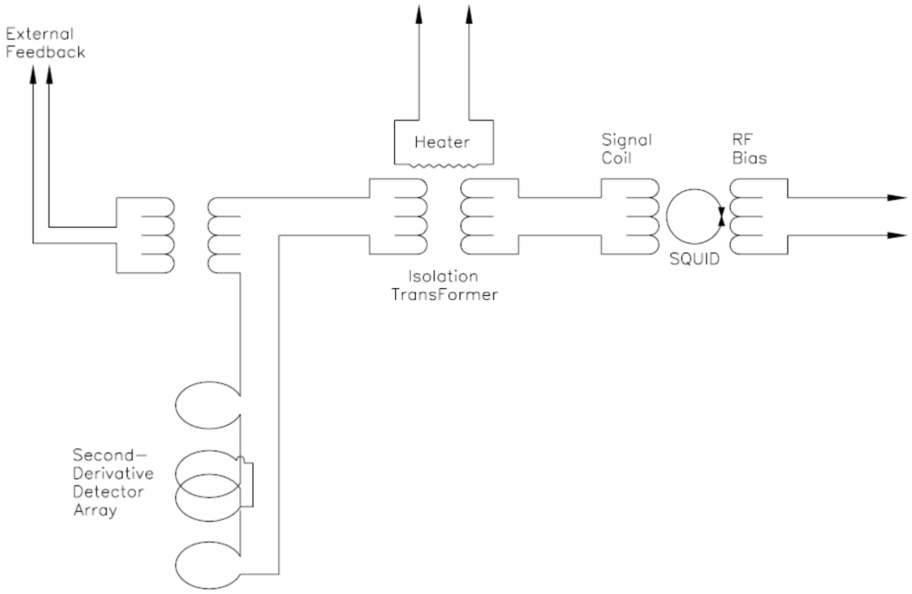

Fig. 3.11: Schematic of signal coupling from pick-up coils to SQUID by an isolation transformer to match inductances of pick-up coils and SQUID. Taken from Quantum Design MPMS manuals.

loop with two Josephson junctions. As for this study a dc-SQUID-based MPMS from Quantum Design was used, the following description is limited to the operation principle of a dc-SQUID device.

When passing a constant current I through the SQUID which is lower than the critical current, I_c, no voltage drop can be measured across the SQUID, as the Cooper pairs are tunnelling through the Josephson junctions. When increasing I above I_c, a voltage starts dropping across the SQUID, as the current is not solely transported by Cooper pairs but by an additional, single-electron driven current. Introducing an external magnetic field to the SQUID, screening currents start flowing inducing a magnetic flux opposing the applied external flux. The screening currents alter the voltage drop across the SQUID, making it acting as a flux-to-voltage converter. Since the magnetic flux is quantised, the voltage across the SQUID oscillates as a function of the external magnetic flux. The oscillation period of this voltage is equivalent to a change in the magnetic field in the order of one flux quantum.

Technically, SQUIDs are usually not used to measure the change in magnetic flux directly, as they are highly sensitive to any magnetic and electric noise. Physically, SQUIDs are mounted very often in a box made of superconducting material which is held at temperatures below T_c to shield the SQUID against noise sources as much as possible, as superconductors do act as ideal diamagnets below T_c. The only connections into this box are coils of superconducting wire for SQUID biasing (signal read-out) and SQUID signal coupling, see Fig. 3.11. Signal coupling describes the coupling of an external voltage to the SQUID, which can be induced, for example, in an external loop of a superconducting wire. Figure 3.11 shows the principle of a measurement setup of the MPMS utilised for this study, containing a second derivative detector array forming this external loop(s). The second derivative detector array consists of two first order gradiometer coils of superconducting wire, which lead, if being well-balanced, to a zero voltage drop between the coils when having applied a homogeneous magnetic flux B_z in z-direction. A non-zero voltage is obtained when having a field gradient $\partial B_z/\partial z$ along z by, e.g., moving a sample through the pick-up coils. The detector array is mounted vertically (in parallel to the z-direction) within a superconducting magnet, so that

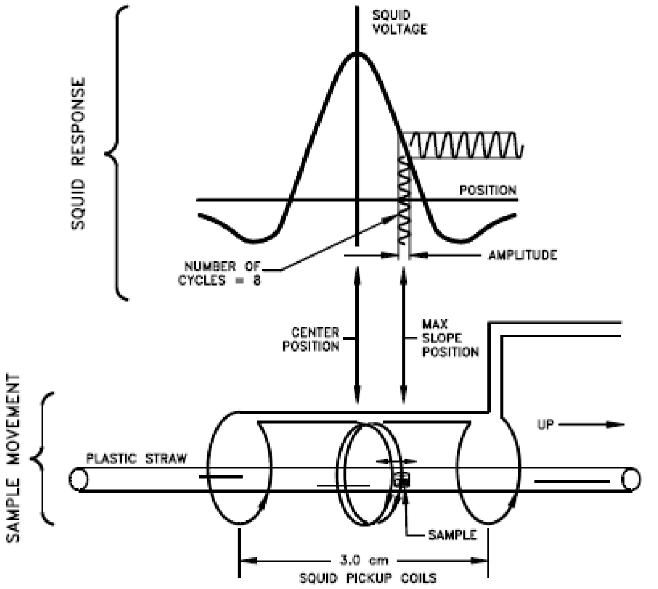

Fig. 3.12: Schematic of how the SQUID signal corresponds to sample movement in a MPMS from Quantum Design, utilising the Reciprocating Sample Option (RSO). Taken from Quantum Design MPMS manuals.

the magnetic flux generated by the magnet is as homogeneous as possible within the array, and the second order gradiometer becomes relatively insensitive to field drifts, even for high field changes. If now the magnetic flux is changed by moving a sample through the detection array, a voltage is induced and coupled by a flux transformer to the input inductance located next to the SQUID. Due to the change in magnetic flux in the SQUID, screening currents are induced. The biasing current in the SQUID is optimised to achieve highest amplitude and thus sensitivity of the resulting oscillating voltage dropping across the SQUID. The obtained voltage is fitted by a non-linear, least-square fitting routine provided by the measurement software, which correlates sample movement speed, sample position, and SQUID voltage to determine the magnetic moment of the measured sample. Please note that with vertically mounted gradiometers, so-called longitudinal SQUIDs, only M_z of the sample (the projection of $\vec{M}$ on the z-axis) is accessible. For the determination of the magnetisation vector $\vec{M}$, a combination between longitudinal and transversal SQUID with horizontally mounted gradiometers is needed.

The current MPMS setup is equipped with a reciprocating sample option (RSO), allowing for highly sensitive measurements with resolutions of $5\text{x}10^{-9}$ emu (emu = electromagnetic unit; 1 Am^2 = 10^3emu) in the case of extreme low external noise. When utilising the RSO-option, the sample, which is mounted in a homogeneous plastic straw, is moved sinusodially through the centre of the second order gradiometer. The sinusoidal movement allows combining the SQUID voltage measurement setup with lock-in techniques, which in turn reduces contributions of external noise to the measurement signal. Figure 3.12 shows a scheme of how sample movement and SQUID voltage correlate in the case of a RSO head. The displayed voltage vs. position plot denotes to an ideal magnetic dipole, since it shows perfect symmetry to the ordinate.

Such perfectly symmetrical signals are only obtained in very few cases, as they imply perfectly homogeneous samples with only one centre of magnetic moment. As an example, many samples do have at least two different phases (e.g., substrate and thin film), which have different magnetic properties (e.g., ferromagnetic and diamagnetic). In the case of undoped

HfO_2 on *c*-cut sapphire substrates, both, film and substrate have diamagnetic characteristics that lead to a symmetric SQUID response. In the case of heavily Ni-doped HfO_2 on sapphire, the film shows ferromagnetic properties whereas the substrate stays diamagnetic. Replacing the ferromagnetic film and the diamagnetic substrate by two infinitely small point masses, the chance that their centres of magnetic moments projected on the z-axis are coinciding is very rare. Two centres of magnetic moment in z of different nature lead to a superposition of two measurement signals, which leads to a non-symmetric SQUID-signal, thus 'distorting' the observed SQUID voltage. As usually neither the exact phase volume fractions, nor the magnetic moment per volume fraction, nor the centres of the magnetic moments with respect to z are known, it is challenging to properly evaluate the obtained measurement data in such cases. This effect is prominent especially for powder samples containing a mixture of diamagnetic and ferromagnetic/paramagnetic phases. Ways to prevent 'distorted' signals are either to keep the sample as small as possible (in the case of powders pressing a pellet and using only a small fraction of such a pellet) or to change the applied magnetic field in such a way that the contribution of one phase to the overall magnetic moment is minimised and the other is maximised. Another way to reduce the effects of possible signal distortions is to intentionally separate the centres of magnetic moment from the thin film and the substrates by mounting the sample horizontally into the plastic straw, so that the magnetic field is incident perpendicular to sample surface. If now choosing the magnitude of the applied external field in a proper way, both centres can be identified separately and thus the measurement can be designed in such a way that only film contributions are obtained.

The current MPMS has a field capability of ± 7 Tesla, whereas the temperature can be varied from liquid helium temperature ($\sim$4.2 K) up to 350 K in a continuous mode, whereas temperatures from 1.8 to 4.2 K can be sustained only for a limited time period. Sample size is limited to maximum 8 mm in diameter, as the inner diameter of the sample bore is 8.5 mm. A good description of MPMS functionality, basic equations, and measurement principles can be found in ref. [174, 175], MPMS manuals, application notes, and user's guidelines from Quantum Design.

4 Growth of HfO_2 thin films

4.1 Introduction

As described in the introductory sections of this thesis, hafnium oxide thin films have been grown by various deposition methods. Most studies on HfO_2 are focussed on device related topics, therefore, most commonly used growth techniques are ALD and CVD. These growth techniques can be scaled up to industrial level rather easily compared to RMBE. When it comes to the growth of HfO_2 by RMBE, there are principally two different approaches of how thin films can be grown.

- First approach is the evaporation from a stoichiometric HfO_2 target with an electron beam and later condensing the evaporant on a suitable substrate. HfO_2 targets are usually synthesised via solid-state synthesis routes. The advantage of this approach is the relative simplicity of the evaporation process, as only one source has to be controlled. Additionally, no reactive gases have to be introduced into the growth chamber, resulting in lower deposition pressures compared to, e.g., PLD and sputtering. Note, lower growth pressures allow lower substrate temperatures. One downside is the limited possibility to influence film stoichiometry, as mostly target composition determines film composition. However, stoichiometry can be varied in a small range by means of substrate temperature, and the provision of additional gases during deposition.
- The second approach is to form HfO_2 thin films from its constituent elements, hafnium and oxygen, realised by e-beam evaporation of metal Hf and the external supply of oxygen. For the oxygen flux, mainly three possibilities exist; molecular oxygen (O_2) provided directly via an oxygen nozzle, ozone (O_3) generated by ozone generators and introduced via nozzles, and radical oxygen (O^*) generated by radical sources. All different types of oxygen sources do have unique features and drawbacks, as discussed in section 2.2.2; for the present study oxygen radicals were used. In principle, providing separate hafnium and oxygen fluxes with individual flux control has the advantage of growing films with tailored stoichiometry in a broad range. Principally one can vary the Hf to oxygen ratio from infinity (pure Hf) to ½ (HfO_2) during growth, however, certainly not for all hafnium to oxygen ratios stable hafnium oxide thin films form. The disadvantage of this approach is the presence of an additional gas in the growth chamber, increasing chamber pressure during deposition (up to 10^{-4} mbar) depending on the oxidation conditions.

In this study, HfO_2 thin films were fabricated by RMBE using e-beam evaporation of Hf metal and *in situ* oxidation by radical oxygen. Prior to the investigation of the effect of oxygen deficiency in hafnium oxide thin films, growth conditions for stoichiometric, high-quality HfO_2 thin films were established first. Key growth parameters were identified and their impact on film quality in terms of film crystallinity, orientation, electrical & optical properties, and magnetic properties were studied carefully. This section ends with an overview of selected physical properties of the grown HfO_2 thin films suitable to verify film stoichiometry.

4.2 Substrates and substrate preparation

The following section describes aspects related to substrate choice, which are not only valid for the growth of stoichiometric hafnium oxide, but also for the growth of oxygen deficient hafnia, described in detail in section 5. As discussed earlier in section 1.3.1, HfO_2 is known to stabilise in its monoclinic phase under ambient conditions with $a \neq b \neq c$, $\alpha = \gamma = 90°$ and $\beta \neq 90°$. According to ICDD data for m-HfO_2 (pdf-card 00-034-0104), $a = 5.285$ Å, $b = 5.182$ Å, $c = 5.116$ Å, $\beta = 99.259°$. There is a vast variety of substrates available and already tested for the growth of HfO_2 thin films. As this study was not focused on the effect of different substrates on crystal structure, film orientation, interfacial layer formation, etc., the studies were mainly focused on sapphire single crystal substrates. However, the following paragraphs discuss silicon, sapphire, and yttria stabilised zirconia (YSZ) as possible substrates for $HfO_2/HfO_{2\pm x}$ thin film growth.

4.2.1 Silicon

For hafnium oxide to be used as a gate dielectric in semiconductor industry, the substrate of choice is undoubtedly silicon. Silicon substrates are the basis of the well-known Si/SiO_2 FET system, and, are available in various sizes and orientations in high quality at affordable prices. Besides, common CMOS processing is based on silicon wafers; from wafer handling, stripping, deposition methods, device design, device testing, and so forth, everything is optimised for silicon wafers. Changing the substrate type involves the development of processing and production procedures of semiconductor devices, which imply large financial investments and research efforts. Hafnium oxide tends to form a SiO_2-rich interfacial layer with stripped silicon substrates. Interfacial layer formation between hafnia and Si is a result of either oxidising conditions during growth,[176] or of intentional growth.[74, 177, 178] The formation of interfacial layers usually goes hand in hand with the reduction of the attainable capacitance in the case of HfO_2-based FETs, and an increase of the number of defects, which in turn decrease charge carrier concentration and mobility. All these aspects do affect device performance adversely and extensive research efforts were necessary to minimise their imprint on later device performance. An advantage of amorphous SiO_2 interfacial layers on top of Si is the tendency of HfO_2 to grow with an amorphous structure on SiO_2 at CMOS processing temperatures. Amorphous films are preferred to polycrystalline films, as grain boundaries lead to increased device leakage currents. Alternative substrates to Silicon are Germanium for possible applications of HfO_2 in MOSFETs for high-speed electronics,[179] GaN for applications in high-speed, high-temperature, and high-power applications,[180] and InP for MOS capacitors[181] and MOSFET applications.[182] When it comes to epitaxial growth of HfO_2 on Si (111) substrates, which is the commonly used orientation for the industrial growth of Si-based microelectronics, the 7x7 reconstruction of stripped Si under vacuum does not provide a surface termination allowing epitaxial growth of HfO_2. In this study, silicon substrates were not used, as (i) no proper substrate stripping facilities were accessible, and (ii) this study was not focussed on the study of electronic device properties. The growth of HfO_2 on amorphous SiO_2 was considered to have disadvantages in terms of interfacial reactions compared to, e.g., sapphire substrates.

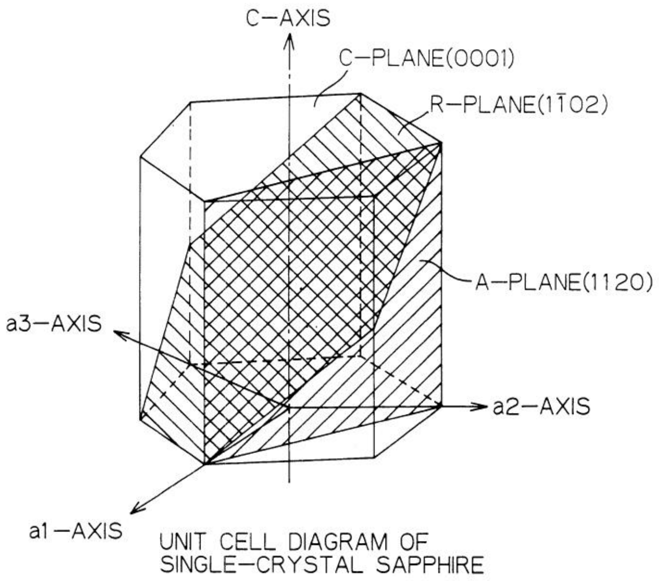

Fig. 4.1: Scheme of a sapphire single crystal visualising the different commercially available crystal orientations.

4.2.2 Sapphire

The main focus of this study was to study the effect of various oxygen contents in hafnium oxide thin films on their structural, optical, and electrical properties in general rather than to study possible impacts on applications as a high-κ gate dielectric. Interfacial reactions have to be avoided as much as possible ensuring that the studied physical properties are intrinsic to the change of oxygen content in HfO_2. Additionally, crystalline hafnia can usually be grown only at elevated temperatures, which in turn favours possible chemical or physical reactions between thin film and substrate. As mentioned in section 1.3.3, possible d^0-ferromagnetism has been observed in HfO_{2-x} thin films. In order to investigate this effect, a substrate with a well-known magnetisation is needed. A good candidate accounting for the mentioned aspects is single crystalline aluminium oxide (Al_2O_3). Sapphire substrates are chemically inert compared to silicon substrates, which allow higher deposition temperatures, without physical or chemical reaction. Al_2O_3 has even been used as a capping layer for $HfO_2/SiO_2/Si$ stacks in order to prevent the growth of the SiO_2 interfacial layer with post deposition annealing steps under oxygen atmosphere, as Al_2O_3 exhibits very low oxygen diffusion.[183] There are reports on the growth of the pseudo binary alloy $HfAl_xO_y$, possibly yielding to values in k higher than observed for pure HfO_2.[184] At elevated temperatures above 900 °C films tend to recrystallize by the segregation of oxygen deficient clusters of m-HfO_{2-x}. However, most $HfAl_xO_y$ films are amorphous; the formation of crystalline $HfAl_xO_y$ ternary phases has only been reported for ALD-grown films annealed at 900 °C.[185]

Sapphire provides very clean crystal surfaces for potentially epitaxial growth of HfO_2. Single crystalline sapphire substrates are commercially available in various orientations, which are *c*-cut (0001), *a*-cut (1120), *m*-cut (10-10), and *r*-cut (1-102), see Fig. 4.1. Checking for possible epitaxial relations of m-HfO_2 on sapphire substrates, *r*-cut sapphire could be among the promising candidates for epitaxial thin film growth, as the atomic distances of the *r*-cut sapphire surface are 5.12 and 4.76 Å.[186]

For this study, single side polished 5 x 5 mm² and 7 x 4 mm² substrates, and double side polished 7 x 7 mm² substrates were cut from 2” wafers (CrysTeck) and 51 mm² plates, respectively. Corresponding substrate thicknesses were usually 0.43 and 0.5 mm. The cut substrates were thoroughly cleaned before use to remove any contaminations caused by the cutting process. The following procedure was adopted for all self-cut substrates:

1. 2 times 15 min. cleaning with acetone in ultrasonic cleaner
2. 15 min. cleaning with $H_2SO_4 : H_2O_2 = 1 : 1$ in ultrasonic cleaner
3. 2 times 15 min. cleaning with deionised water in ultrasonic cleaner
4. annealing in air/oxygen at 1050 °C for 12 hours.

After cleaning, substrates have been annealed in order to obtain superior surface quality.[187] Extreme care in substrate handling has been taken to avoid contaminations of any kind. All available crystal orientations have been tested for the growth of hafnium oxide thin films.

4.2.3 Yttria stabilised zirconia

YSZ is a well-known substrate in semiconductor and high-T_c thin film growth. Under ambient conditions it crystallises in a cubic structure with a lattice constant of 5.12 Å. Single crystals are available with various orientations, mainly (100), (110), and (111). For this study, (111)-oriented YSZ (CrysTeck) was used for testing potential epitaxial growth of HfO_2, as it has a lattice constant very close to that of m-HfO_2. It is chemically and physically stable even at high substrate temperatures, and shows good chemical compatibility with hafnia.

4.3 Influence of growth parameters for HfO_2 thin films grown on *c*–cut sapphire

The following sections describe the thin film growth of HfO_2 on *c*-cut sapphire by separately investigating the influence of the key deposition parameters, such as, substrate temperature, oxygen flow rate through the radical source, and rf-power applied to the radical source on film crystallinity, crystal structure, and surface topography. The Hf metal evaporation rate was held constant at 0.7 A/s, which is a moderate and well controllable rate for Hf evaporation via e-beam evaporation.

4.3.1 Deposition temperature

A series of 50 nm thick hafnium oxide thin films has been grown on *c*-cut sapphire substrates. The substrate temperature, T_s, was varied from 400 to 800 °C in steps of 100 °C while keeping other deposition parameters constant (200 W rf-power applied to the radical source and 1.5 sccm oxygen flow rate). Note that the indicated temperatures are set temperatures (temperatures obtained by a thermocouple located above the sample holder). In all cases, hafnium oxide stabilised in the monoclinic phase with high texture but with different thin film orientation with respect to the substrate. The change in film orientation has been quantified by monitoring the strongest reflections of m-HfO_2, (-111) and (002), as a function of substrate temperature as shown in Fig. 4.2. The higher the substrate temperature during growth, the

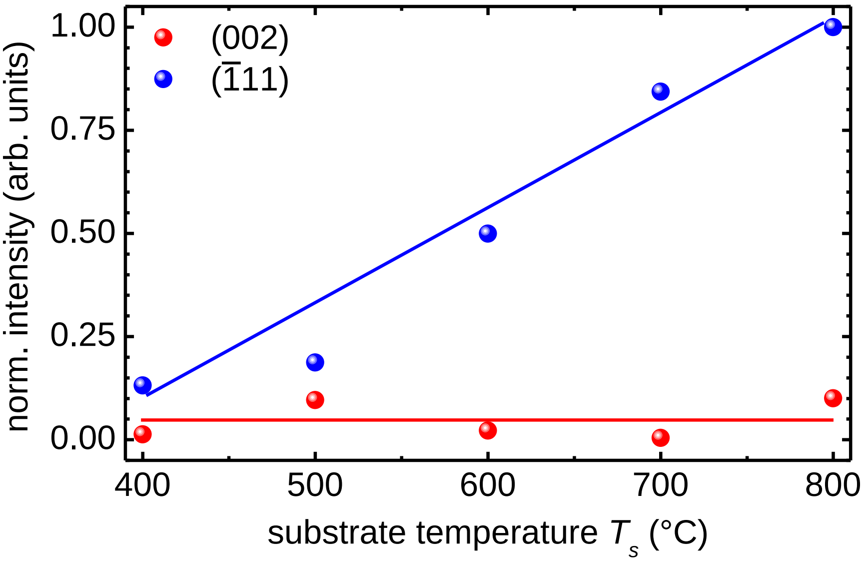

Fig. 4.2: Normalised intensities of the (-111) and (002) reflections of 50 nm thick hafnia thin films as a function of substrate temperature (0.7 Å/s Hf rate, 1.5 sccm oxygen flow rate, 200 W rf-power). Solid lines are guides to the eye. The intensity of the (-111) reflection continuously increases with increasing substrate temperature, whereas the intensity of the (002) reflection does not change systematically.

higher becomes the intensity of the (-111) reflection, whereas the intensity of the (002) reflection does not change systematically. As expected, for low growth temperatures (T_s = 400 °C) film crystallinity is poor yielding to low intensities of the (-111) and (002) reflections. With increasing temperature crystallinity improves, obvious from the increase of X-ray intensities for both reflections at 500 °C. Around 700 °C the X-ray intensity of the (002) reflection is almost vanishing leading to nearly single oriented, highly textured HfO_2 thin films. At temperatures above 700 °C, the (00*l*) orientation is reoccurring. No significant shift in the 2θ angle as a function of substrate temperature of both, the (-111) and (002) reflection, could be noticed. The rocking curves of both reflections have values for the full width at half maximum (FWHM) in the range of 8°, in-plane measurements reveal disorder in the *a*-*b*-plane.

In summary, the resulting films are of polycrystalline nature, *c*-axis (-111)-oriented (textured), but not epitaxial. The increasing intensity and decreasing FWHM of the (-111) reflections with temperature show that increasing temperature leads to increasing crystallinity, crystal size, and preferred (-111) orientation, which is in good agreement with findings from Bharathi *et al.*[188] As reported in literature, for growth temperatures below 400 °C HfO_2 is usually amorphous, whereas at higher temperatures crystallites start to form leading to mixed films of amorphous and polycrystalline fractions.[36, 189, 190] In the case of bulk HfO_2, a transition from the monoclinic phase to the tetragonal phase is reported for elevated temperatures,[39] which could not be observed for our thin films grown at temperatures up to 800 °C. No reflections of other crystallographic morphologies, such as *o*-HfO_2, *t*-HfO_2, and *c*-HfO_2 could be observed.[182, 191, 192] Higher growth temperatures were not investigated, as (i) the formation of mixed compounds of $Al_xHf_yO_z$ due to substrate-film interaction is possible (which would change the focus of this study), (ii) films seem to stabilise in mixed orientation, and (iii) oxygen exchange with the substrate, as reported for the case of Si substrates, may occur.

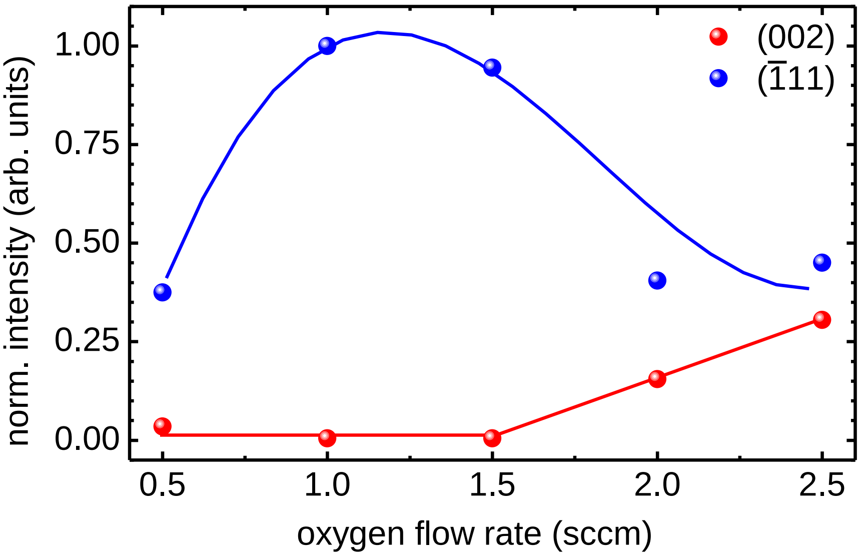

Fig. 4.3: Normalised intensities of the (-111) and (002) reflections of 50 nm thick hafnia thin films as a function of oxygen flow rate during growth (0.7 Å/s Hf rate, T_s = 700 °C, 200 W rf-power). Solid lines are guides to the eye. The (-111) reflection shows a maximum in intensity in the regime of 1.0 to 1.5 sccm, whereas the (002) reflection is not observed.

4.3.2 Oxygen flow rate

The oxygen flow rate was varied from 0.5 to 2.5 sccm of molecular oxygen supplied to the radical source, covering a wide range of oxidation conditions during growth. As already observed for the variation of substrate temperature, at all oxygen flow rates hafnia stabilised in monoclinic phase, highly textured, but with two orientations, namely (-111) and (002). Figure 4.3 shows the dependence of the normalised intensities of both orientations as a function of the oxygen flow rate. The X-ray intensity of the (-111) reflection is highest in the range of 1.0 to 1.5 sccm, where the (002) reflection does not occur and films remain purely (-111) oriented. For low oxygen flow rates, the clearly dominating orientation is (-111). For higher flow rates, there is an increasing amount of (002) oriented crystallites. It is remarkable that although the oxygen content in hafnia has been varied in a wide range, the monoclinic structure sustains and does not collapse, neither due to oxygen deficiency nor due to excess oxygen. Even when reducing the oxygen content further (flow rates below 0.5 sccm), neither metallic hafnium could be observed, nor a collapse of the crystal structure of m-HfO_2 occurred. Metallic hafnium started to form only when molecular oxygen with a much lower oxidation potential than oxygen radicals was supplied during growth at flow rates of about 0.2 sccm. All investigated films showed monoclinic symmetry; no traces of c-HfO_2, o-HfO_2, or t-HfO_2 could be identified within the resolution of the X-ray diffractometer. Oxygen flow rate studies on the growth of hafnium oxide thin films and their influence on crystal structure and film orientation have been carried out earlier, but these studies were more focussed on device properties than on crystallinity and film orientation.[51, 193]

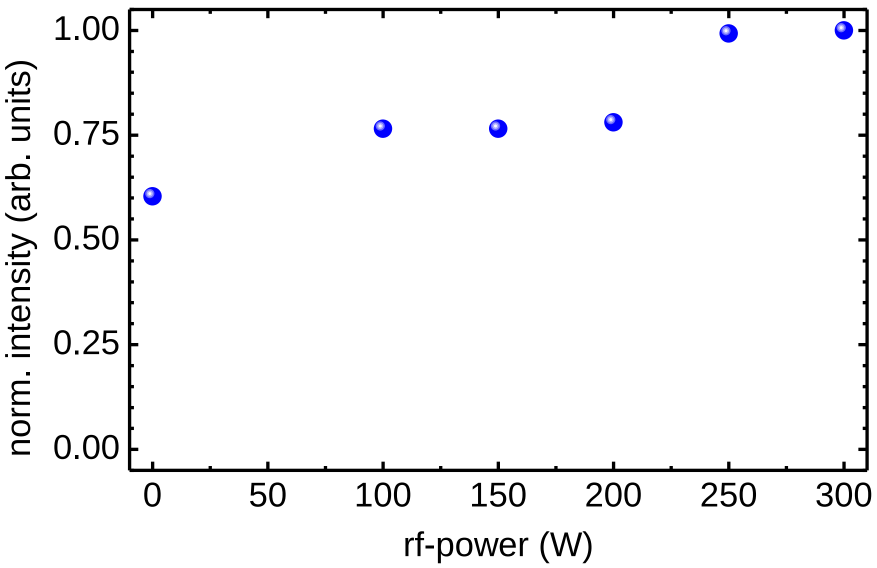

Fig. 4.4: Normalised intensities of the (-111) reflection of 50 nm thick hafnia thin films as a function of rf-power applied to the radical source (0.7 Å/s Hf rate, T_s = 700 °C, 1.0 sccm oxygen flow rate). The intensity of the (-111) reflection increases steadily with rf-power, being highest for 300 W. The (002) orientation of *m*-HfO_2 is suppressed for all different rf-powers.

4.3.4 Effect of rf-power

The higher the applied rf-power is, the stronger the plasma intensity monitored via the attached photocell and the higher the cracking efficiency at a given oxygen flow rate. The rf-power was varied between 0 and 300 W while other deposition parameters were kept constant (0.7 Å/s Hf rate, T_s = 700 °C, 1.0 sccm oxygen flow rate). Very high plasma intensities are observed for high rf-power (e.g., 300 W), which corresponds to very high oxidation conditions. Figure 4.4 depicts the normalised intensity of the (-111) reflection as a function of rf-power applied to the radical source. The intensity of the (-111) reflection increases steadily with increasing rf-power and is highest for 300 W. None of the films showed significant portions of (002) orientation of *m*-HfO_2. In the regime of 100 to 200 W rf-power no change in X-ray intensity of the (-111) reflection could be observed. No significant improve in film quality or change in orientation for rf-power greater than 200 W is observed, whereas the wear of the discharge tube increases rapidly with increasing rf-power. That is why the maximum rf-power applied to the radical source was limited to 300 W. However, high rf-power and high oxygen flow rates (denoting to very high oxidation conditions) yield to a change in film orientation, as described later in section 5.2.

It can be seen from Fig. 4.4 that molecular oxygen is sufficient to form thin films of hafnia, but with lower crystal quality, as evident from X-ray intensity. Lower crystal quality of HfO_2 thin films grown under molecular oxygen compared to HfO_2 grown under oxygen radicals is confirmed by RHEED, as for films grown under molecular oxygen RHEED shows more spots and rings than streaks. Although the growth of hafnia using molecular oxygen is possible, lower growth pressures (lower oxygen partial pressures during growth) while maintaining comparable oxidation conditions can only be realised by using radicals instead of molecular species. Furthermore, an oxygen radical source allows for a much more precise control of the oxidation conditions during growth. From the above study it is clear that with utilising rf-activated oxygen one can grow high-quality thin films of hafnium oxide.

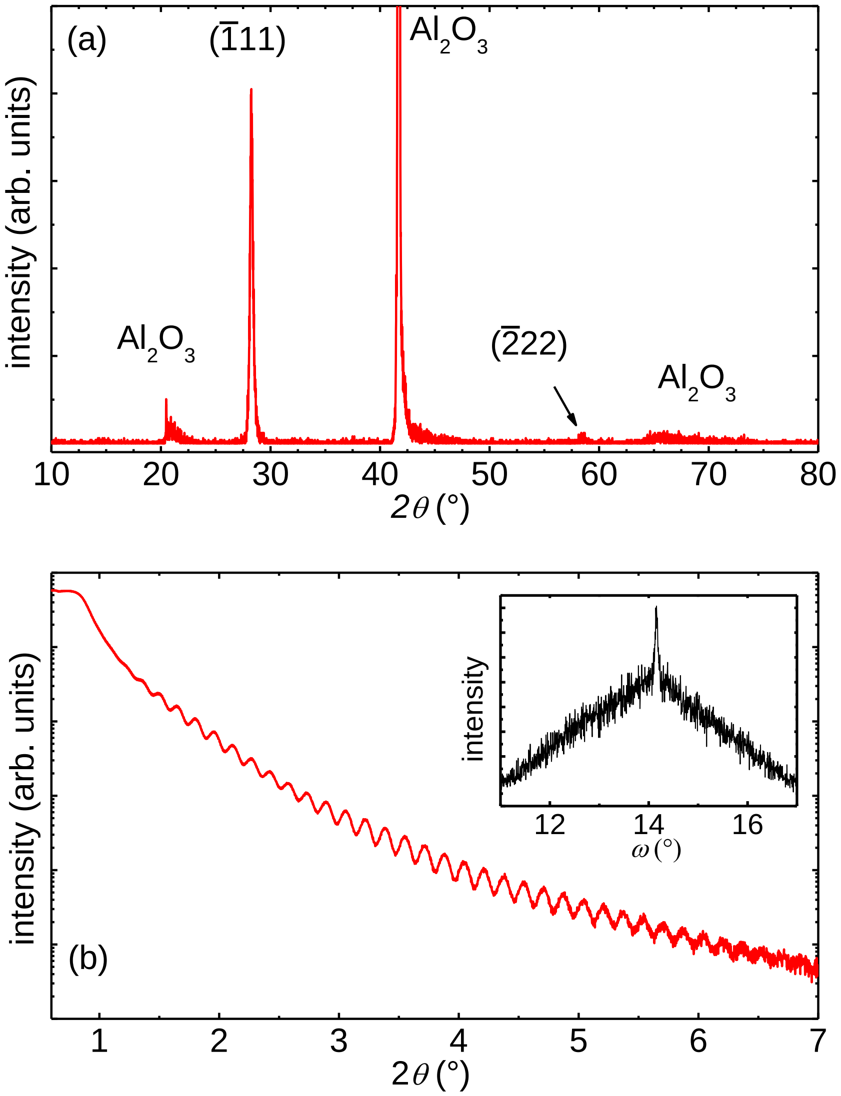

Fig. 4.5: (a) 2θ–θ scan for a 50 nm thick hafnium oxide thin film on *c*-cut sapphire grown under optimal growth conditions, *m*-HfO_2 films are single (-111)-oriented (b), corresponding XRR pattern indicating low film and interface roughness. Inset: Rocking curve of the (-111) reflection.

4.3.5 Optimal growth conditions of HfO_2 on *c*–cut sapphire

Fig. 4.5 (a) shows a 2θ–θ scan of a nominally 50 nm thick HfO_2 thin film grown on *c*-cut sapphire under optimised growth conditions with respect to Hf rate (0.7 Å/s), substrate temperature (700 °C), oxygen flow rate (1.0 sccm), and rf-power applied to the radical source (200 W). Under these optimised growth conditions, single (-111)-oriented films of *m*-HfO_2 are obtained. The X-ray reflectivity pattern given in Fig. 4.5 (b) indicates low surface and interface roughness, as undamped X-ray intensity oscillations are observed up to higher angles of more than 6° in 2θ. From the period of oscillation in Fig. 4.5 (b), a film thickness of 52.4 nm is extracted, which is in good agreement with the calculated nominal film thickness of 50 nm. Low surface roughness is further confirmed by AFM measurements, giving a surface roughness of less than 0.22 nm in RMS (measurement area 1 μm^2) as shown in Fig. 4.6. Similar low surface roughness usually cannot be obtained without post deposition annealing treatments in

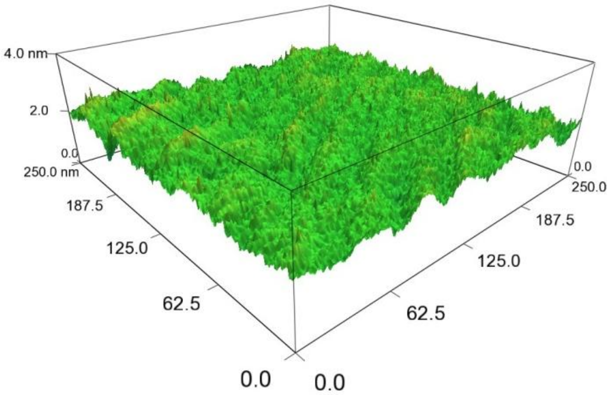

Fig. 4.6: AFM image of a 50 nm thick hafnium oxide film grown under optimised conditions with a surface roughness of 0.22 nm RMS in a measured area of 1 μm² indicating high surface quality.

the case of ALD or MOMBE-grown films. Even films thinner than 50 nm are reported to exhibit a roughness of 1.0 nm in RMS for measured areas of 1 x 1 μm² (ref. [51, 194]) and 10 x 10 μm² (ref. [195]). In the case of RMBE-grown hafnia, post deposition annealing processes are evidently not essential in order to obtain high quality thin films of HfO_2.

The inset of Fig. 4.5 shows the corresponding rocking curve to the (-111) reflection of monoclinic hafnia. It shows a sharp Bragg peak with a FWHM below 0.1°, further confirming the highly oriented nature of the film. The broad portion of the rocking curve represents diffuse scattering due to dislocations accumulated in the film.[196] These dislocations may occur due to epitaxial strain in the film. The thicker the deposited films are, the lower the intensity of the Bragg reflection of the rocking curve compared to the broad portion evoked by dislocations. This implies that with increasing film thickness, first, dislocation density increases until the film relaxes by the formation of grain boundaries (annihilation of dislocations), reducing the strain inside the film. For relaxed films, only broad rocking curves with FWHM above 1° are observed, nevertheless films stay highly textured in Al_2O_3 [000*l*] direction (perpendicular to *c*-cut sapphire substrate surface).

One way to identify and isolate strain effects from grain size effects in x-ray out-of-plane diffraction patterns (not rocking curves) is the well-known Williamson-Hall plot, in which $B\cos\theta$ is plotted as a function of $\sin\theta$ for all observed reflections and fitted with a linear function. In case of strain effects, the slope of the fitted straight line differs from zero, whereas line broadening due to size effects does lead to a slope of zero. As for the present study only two reflections for thin *m*-HfO_2 films have been observed over the studied 2θ range, (-111) and (-222), no Williamson-Hall plot has been performed.

4.4 Growth of HfO_2 on *r*–cut, *a*–cut, *m*–cut sapphire and YSZ(111)

For most growth parameter investigations performed for HfO_2 on *c*-cut sapphire described in the previous sections, the growth on *r*-cut sapphire substrates has also been investigated. The hafnium oxide thin films on *r*-cut sapphire were (00*l*)-oriented, but did not show any epitaxial growth as observed for *c*-cut sapphire. This is confirmed by X-ray studies, showing only weak or vanishing intensities of the (002) reflection of *m*-HfO_2. RHEED observations indicate island formation occurring much earlier during growth than observed for *c*-cut sapphire. As the variation in the growth parameters substrate temperature, oxygen flow rate, and rf-power applied to the radical source did not significantly improve crystal quality, the growth of hafnia on *r*-cut sapphire was not followed up any further, except for annealing experiments (see section 4.5.3).

Other orientations of sapphire single crystals (*m*-cut and *a*-cut) have been tested for epitaxial growth of HfO_2. Low Hf growth rates (0.2 to 0.5 Å/s) at extreme low oxygen flow rates (0.12 sccm) and 250 W of rf-power have been investigated, leading to single (-111)-oriented films on *a*-cut sapphire, but with lower crystal quality compared to films grown on *c*-cut sapphire with similar conditions. For the mentioned growth conditions, the formation of crystalline hafnium oxide on *m*-cut sapphire and on (111)-oriented YSZ has not been observed. Please note that for the growth study of hafnium oxide thin films on substrates other than *c*-cut sapphire, similar growth conditions to those for *c*-cut sapphire have been applied. As the scope of this study was not to intensively investigate the growth of hafnia thin films on various substrates, no growth optimisation has been performed for substrates other than *c*-cut sapphire. Due to the significantly lower thin film quality compared to films on *c*-cut sapphire (using similar growth conditions), further studies of the growth of hafnia thin films on other substrates were not followed up.

4.5 Epitaxial thin films of hafnium oxide on *c*–cut sapphire

As described in section 4.3.5, HfO_2 grows highly oriented on *c*-cut sapphire substrates under optimal growth conditions. For thicker films, crystal quality decreases (film mosaicity increases), as evident from the decreasing intensity of the Bragg reflection of the rocking curve and the increasing portion of diffuse scattering due to increasing dislocation density. However, during growth of hafnium oxide thin films under optimal growth conditions clear streaky RHEED patterns have been observed during initial film growth indicating smooth and possibly epitaxial films. In order to increase critical film thickness (film thickness after which film relaxation occurs) and to study possible epitaxy of HfO_2 on *c*-cut sapphire, films have been grown on *c*-cut and *r*-cut sapphire with reduced Hf deposition rates, reduced oxygen flow rates, constant substrate temperature (~700 °C), and various rf-powers applied to the radical source.

By reducing the Hf growth rate below 0.7 Å/s, the mobility of the adsorbed Hf-atoms on the substrate/film surface is increased, as lesser atoms arrive at the substrate/film surface in time. Reducing the Hf rate allows to reduce the oxygen flow rate, as lesser oxygen is now needed to form hafnium oxide with similar stoichiometry. Lower oxygen flow rates significantly reduce chamber pressures during growth (up to three orders of magnitude), which in turn further increase the mobility of the adsorbed atoms on the substrate/film. An increase in mobility of the adsorbed atoms could favour layer-by-layer growth and, thus, increase critical (epitaxial) film thickness.

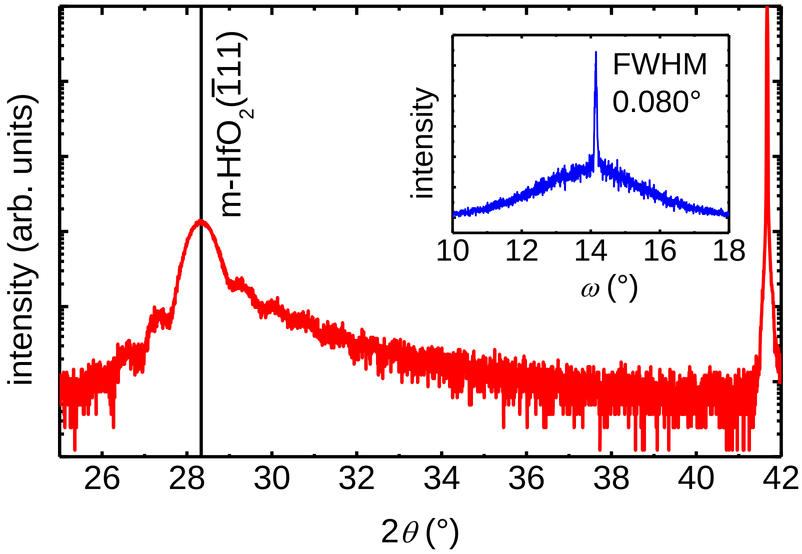

Fig. 4.7: 2θ–θ scan of a 13 nm thick (-111)-oriented hafnium oxide thin film grown on *c*-cut sapphire (0.2 Å/s Hf rate, 0.2 sccm oxygen flow rate, 140 W rf-power, 700 °C substrate temperature). Laue oscillations indicate low interface roughness and high crystallinity. Inset: Corresponding rocking curve of the (-111) reflection of *m*-HfO_2.

4.5.1 (-111)-oriented films of hafnia

4.5.1.1 X-ray out-of-plane measurements

Fig. 4.7 shows a 2θ–θ scan of a 13 nm thick hafnium oxide thin film grown on *c*-cut sapphire with 0.2 Å/s Hf rate, 0.2 sccm oxygen flow rate, 140 W rf-power, and 700 °C substrate temperature (sample H12144d). Under these growth conditions hafnium oxide stabilises in its monoclinic crystal structure with (-111) out-of-plane orientation. The observation of Laue oscillations indicate high film quality with low interface roughness, which is further confirmed by the low FWHM of the corresponding rocking curve of 0.080°, shown as an inset of Fig. 4.7. In comparison to the rocking curve of the film grown under optimal growth conditions (see inset of Fig. 4.5), the intensity of the Bragg peak is higher, whereas the broad contribution due to dislocations is lower. This is explained by the decreased film thickness of 13 nm compared to 50 nm, as for lower film thicknesses the number of dislocations and their contribution is smaller. The asymmetric Laue oscillations towards higher values of 2θ indicate a gradient to lower *d*-values of the corresponding lattice constant within film thickness.[197] Due to the phase problem in X-ray diffraction, it cannot be stated in which direction *d* decreases (towards substrate or towards surface). A gradient in *d* could occur due to (i) epitaxial strain or (ii) due to a change in *d* as a function of oxygen vacancy concentration. In the latter case it would imply a gradient in oxygen vacancies within film thickness, which is unlikely as the growth conditions and, thus, the oxidation conditions have not significantly changed during deposition. However, a gradient within reduced hafnium oxide thin films is also supported by XRR analysis, as fitting attempts of the XRR data suggested a non-linear density gradient across the film. Additionally, film relaxation studies (see section 4.5.1.3) further confirm a gradient in *d* and suggest that the *d*-value is lower at the film – substrate interface and relaxes towards film surface.

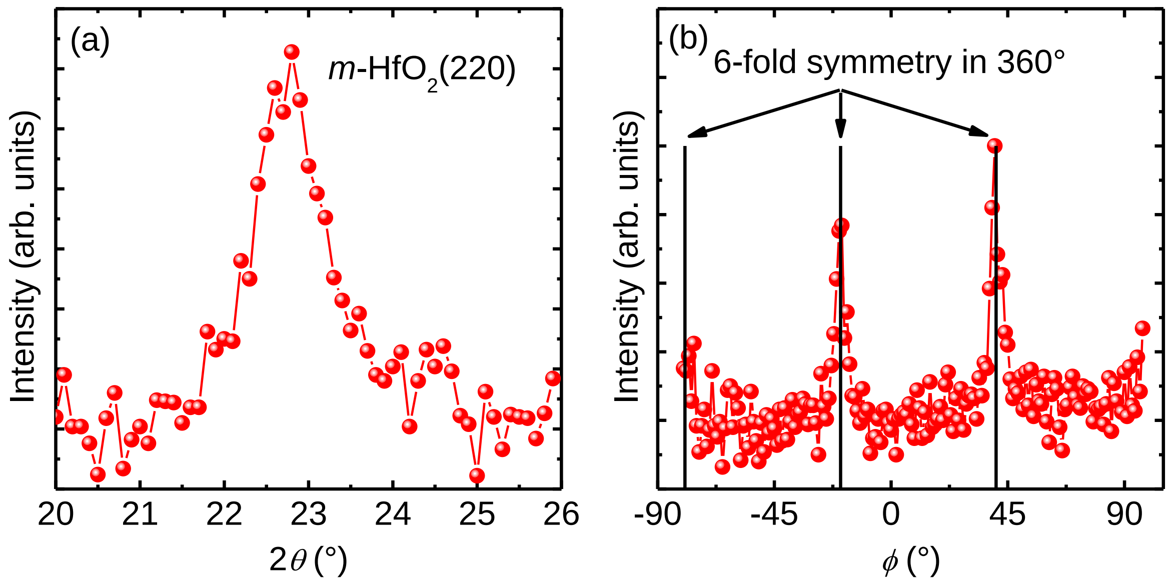

Fig. 4.8: (a) In-plane scan of the (220) reflection of *m*-HfO_2 on *c*-cut sapphire of sample H12144d studied in section 4.5.1.1, (b) corresponding phi-scan suggesting 6-fold symmetry. Note that the measurements have been conducted with Mo radiation.

4.5.1.2 Gracing incidence in-plane x-ray measurements

To check for film epitaxy of sample H12144d investigated in section 4.5.1.1, gracing incidence in-plane measurements have been conducted in collaboration with Prof. Donner, Department for Structure Research, TU Darmstadt. For (-111)-out-of-plane-oriented *m*-HfO_2, the (220) reflection is expected to be found by gracing incidence in-plane measurements in case of film epitaxy. As the angle between the (-111) and the (220) lattice plane normal is calculated to be 87.2552°, in-plane measurements were performed with a 2.7448° tilted substrate with respect to the goniometer centre plane. In addition, the sample was aligned in phi with respect to Al_2O_3 [1-100], as the (220) reflection of *m*-HfO_2 was expected to be found along Al_2O_3 [1-100]. Figure 4.8 (a) shows the gracing incidence in-plane scan of the (220) reflection of *m*-HfO_2 (measured with Mo radiation) after sample alignment. A *d*-spacing of 1.80 Å is derived from $\lambda = 0.71$ Å and a diffraction angle of $2\theta = 22.76°$, which is in good agreement with 1.84 Å known for the (220) reflection of *m*-HfO_2 from ICDD data (pdf 00-034-0104). The observation of the (220) in-plane reflection of *m*-HfO_2 confirms epitaxial film growth, the epitaxial relations are *m*-HfO_2(-111)||Al_2O_3(0006) for out-of-plane and *m*-HfO_2[220]||Al_2O_3[1-100] for in-plane.

The corresponding phi scan of the (220) in-plane reflection suggests 6-fold symmetry. In fact, as *m*-HfO_2 only exhibits 2-fold symmetry in [-111], the observed 6-fold symmetry can be interpreted as a three times 2-fold symmetry. Each domain is rotated by 60° and registered on *c*-cut sapphire, corresponding to the hexagonal symmetry of the substrate. Figure 4.9 shows a simulation of reciprocal space ((*h k* 0)-plane) with in-plane reflections observable for *c*-cut sapphire in (000*l*) out-of-plane direction and epitaxial *m*-HfO_2. Please note that for the shown reflections of *m*-HfO_2 *l* is greater than zero, whereas displayed is the projection of the Ewald sphere on the (*h k* 0) plane of *c*-cut sapphire is displayed in Fig. 4.9. The 3 times 2-fold symmetry is visualised in Figure 4.9 (a), (b), and (c) accordingly.

Please note that in the case of monoclinic hafnium oxide the (-111) axis shows only two-fold symmetry in contrast to a (111) axis of a cubic crystallographic system. Monoclinic systems are often interpreted as 'distorted' cubic systems, as in many cases neither lattice constants nor β (the angle which is greater than 90°) of the monoclinic system do deviate much from an 'undistorted' cubic system. Although the lattice constants of m-HfO_2 do not show significant difference among each other (a = 5.285 Å, b = 5.182 Å, c = 5.116 Å), β differs with 99.259° significantly from 90°. This difference of more than 9° leads to the previously mentioned and observed angle of 87.2552° between the (-111) and (220) lattice planes instead of 90° for cubic systems. The non-equality of the (-111) and (111) reflection for m-HfO_2 is further evident from x-ray studies revealing d-spacings of 3.1471 Å and 2.8234 Å for the (-111) and (111) reflections of m-HfO_2, respectively.

After finding the epitaxial relation of m-HfO_2 on c-cut sapphire and its simulation in reciprocal space, the development of a real space model was targeted in order to get a better understanding of how (in detail) monoclinic hafnia registers on a c-cut sapphire surface. Vast simulations using VESTA have been performed, but it was not possible to develop a meaningful real structure due to (i) a lack of knowledge about the exact interface of hafnia and sapphire and (i) the monoclinic nature of the film. In order to further clarify this point, the measurement of crystal truncation rods of several symmetric and asymmetric reflections of m-HfO2 could be measured with synchrotron radiation to get clear information on the electron density at the film – substrate interface. Utilising this information allows modelling the crystal terminations and reconstructions of alumina and m-HfO_2 and, thus, the development of a real space growth model. As the development of a real space growth model of m-HfO_2 on c-cut sapphire was not the focus of this study, no crystal truncation rods were measured.

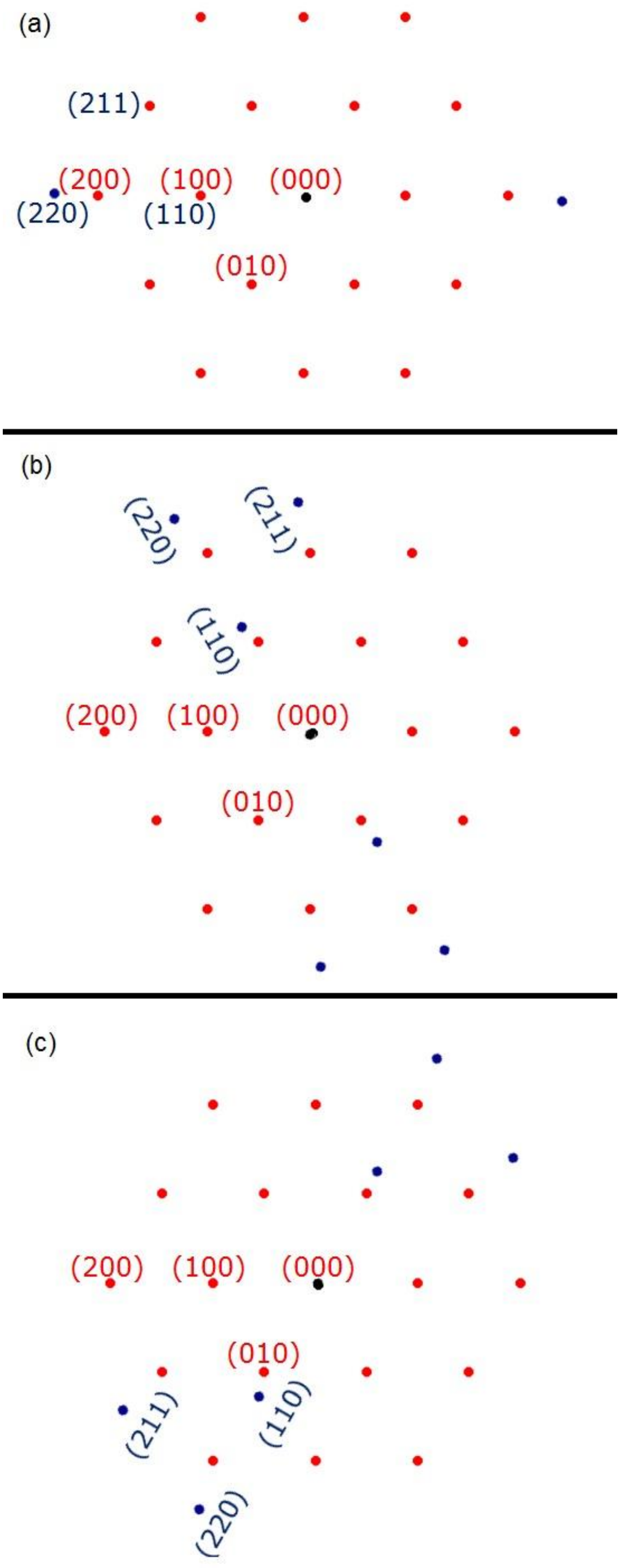

Fig. 4.9: Simulation of the reciprocal space for *m*-HfO_2(-111)||Al_2O_3(0006) out-of-plane and *m*-HfO_2[220]||Al_2O_3[1-100] in-plane. Red dots represent reflections of Al_2O_3, blue dots of HfO_2, shown is the (h k 0) plane of Al_2O_3. The 3 times 2-fold symmetry is depicted by the three different domains of *m*-HfO_2, (a) to (c), each rotated by 60°.

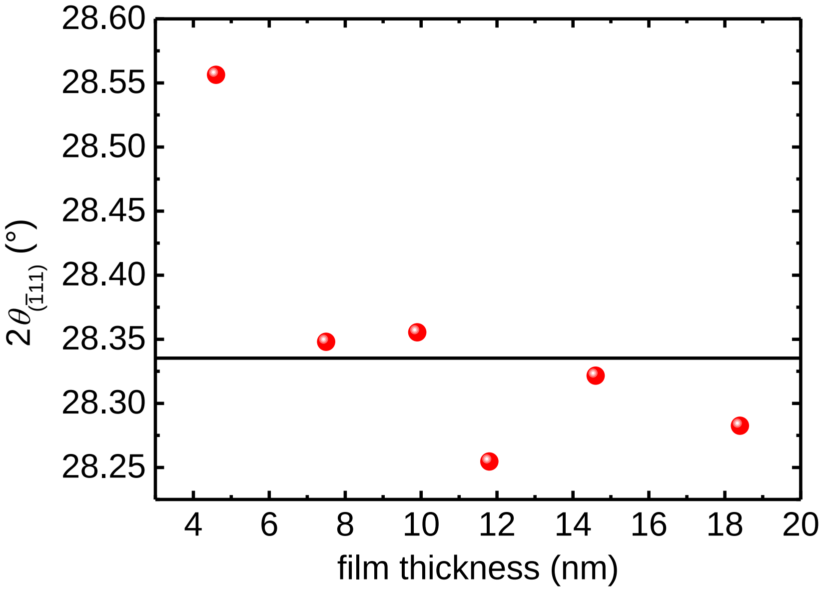

Fig. 4.10: Variation of 2θ of the (-111) reflection of *m*-HfO_2 as a function of film thickness. The solid horizontal line indicates $2\theta = 28.335°$ known for relaxed *m*-HfO_2 according to ICDD data (pdf 00-034-0104).

4.5.1.3 Film relaxation studies

As evident from the previous sections the epitaxial relation of *m*-HfO_2 on *c*-cut sapphire has been determined from out-of-plane and in-plane x-ray measurements using the (-111) and (002) reflection, respectively. In order to resolve possible epitaxial strain, usually reciprocal space maps are performed displaying the intensity of one film and one adjacent substrate reflection as a function of q_z and $q_{x/y}$. In the present case it was not possible to obtain reciprocal space maps of similar kind in reasonable time, as neither out-of-plane film reflections nor in-plane film reflections are close to corresponding substrate reflections. In addition, Nelson-Riley plots allow reducing the error in determining the corresponding *d*-spacing of an x-ray reflection, provided higher homologues are observable in the x-ray pattern. In the present study only the first higher order of the (-111) reflection has been observed, that is why no Nelson-Riley plot has been performed for lattice plane distance determination.

Nevertheless, in order to check for epitaxial strain, a film relaxation study has been performed that principally allows to investigate the out-of-plane and in-plane *d*-spacing as a function of film thickness. Therefore, thin films of hafnium oxide were grown on *c*-cut sapphire at 0.7 Å/s Hf rate, 1.0 sccm oxygen flow rate, 200 W rf-power, and 700 °C substrate set temperature; targeted film thicknesses ranged from 5 to 20 nm. Unfortunately the intensity for the (220) in-plane reflection of *m*-HfO_2 has been too low to be evaluated in a meaningful way for film thicknesses below ~10 nm. As evident from Fig. 4.8, films of 13 nm thickness already yield to averaged *d*-values known for relaxed *m*-HfO_2, hence, no evidence for in-plane strain is found via x-ray studies for film thicknesses above ~10 nm. However, the (-111) out-of-plane reflection of m-HfO_2 shows a shift towards higher 2θ for extreme thin films of ~5 nm in thickness, which could indicate either the presence of epitaxial strain or the formation of a different crystalline phase during the initial growth period on *c*-cut sapphire. The variation in 2θ of the (-111) reflection of *m*-HfO_2 on *c*-cut sapphire is displayed in Fig. 4.10 as a function of film thickness. Seemingly a film thickness around 10 nm represents a critical film thickness for full film relaxation.

4.5.1.4 RHEED imaging

RHEED patterns were continuously obtained during film growth, as RHEED gives real-time feedback of the thin film surface. All shown RHEED patterns have been obtained with 25 kV acceleration voltages of the electron beam. Figure 4.10 (b) and (d) show RHEED images of a 10 nm thick, (-111)-oriented hafnium oxide thin film grown on *c*-cut sapphire, observed in different azimuthal directions, Al_2O_3 [11-20] and Al_2O_3 [1-100], as shown in Fig. 4.11 (a) and (c).[198] Both azimuthal directions are symmetrical to a sample rotation of 60°, as expected from the in-plane analysis for epitaxial (-111) oriented films, see previous section. The rotation symmetry of 60° corresponds to the three times 2-fold symmetry of (-111)-oriented epitaxial hafnia on *c*-cut sapphire. The observed RHEED streaks indicate a smooth film with low surface roughness, in agreement with AFM and X-ray reflectivity measurements (section 4.3.5). In Fig. 4.11 (b), shallow lines in between bright streaks start to appear at film thicknesses in the range of 50 nm. The appearance of additional lines in RHEED at half distance (corresponding to a doubling in *d*) could be explained by (i) the formation of a superstructure during film growth or (ii) multiple diffraction due to high energies of the electron beam.

Integrating the RHEED intensity within the white rectangle, as exemplarily shown in Fig. 4.11 (a) and plotting it as a function of camera pixels, allow accurate determination of the distance between two RHEED streaks. From the distance between two RHEED streaks of two azimuthal directions, Al_2O_3 [11-20] and Al_2O_3 [1-100] (see Fig. 4.11 (a) and (c)), a RHEED camera constant of 133 (Å times pixel) has been calculated using the known *d*-spacings of the (110) and the (100) reflections of alumina (pdf 01-070-7346). In the case of Al_2O_3 [1-100] azimuthal direction (Fig. 4.11 (d)), the *d*-spacing is calculated to be 3.59 Å, which is in good agreement with the *d*-spacing of (110) lattice planes in *m*-HfO_2 of 3.68 Å (pdf 00-034-0104). When rotating the sample by an angle of 30°, the (211) reflection of *m*-HfO_2 may appear in RHEED, corresponding to a *d*-spacing of 2.01°. However, the calculated *d*-spacing in Al_2O_3 [11-20] azimuthal direction (Fig. 4.11 (b)) yields to 3.17 Å, which does not correspond to any expected in-plane reflection of *m*-HfO_2. Nevertheless, the observed *d*-spacing of 3.17 Å corresponds well with the *d*-spacing known for (-111) planes observed out-of-plane (3.147 Å). The observation of *d*-spacings corresponding to out-of-plane reflections can be attributed to multiple diffraction.

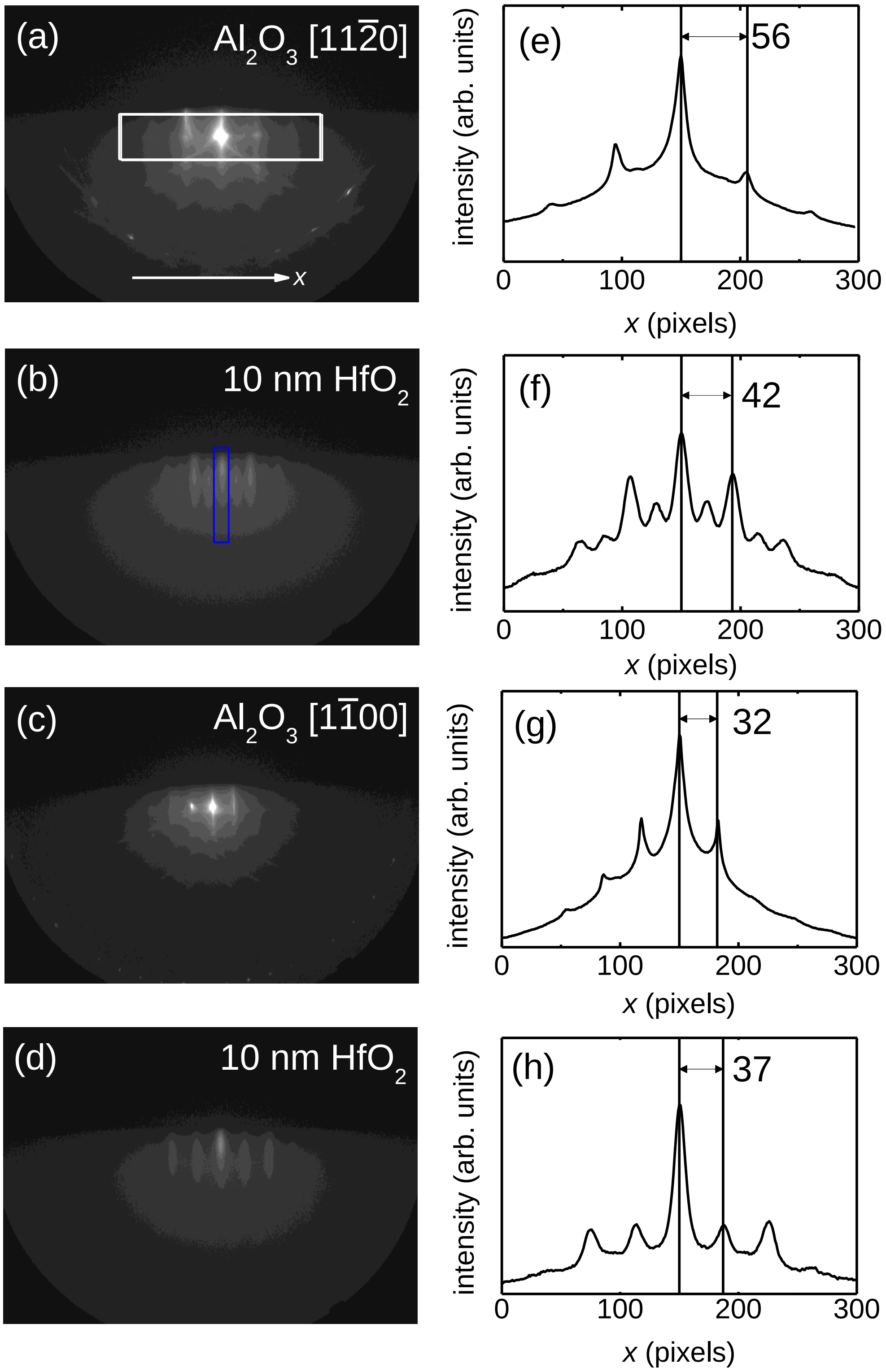

Fig. 4.11: (b) and (d) RHEED images of a 10 nm thick hafnium oxide thin film grown on *c*-cut sapphire, observed in different azimuthal direction (a) and (c) of Al_2O_3; (e) – (h) corresponding RHEED intensity analysis. The white rectangle in (a) indicates exemplarily the integrated area for obtaining the intensity integration shown in (e) to (h), whereas the blue rectangle in (d) indicates exemplarily the integrated area for obtaining RHEED oscillations.

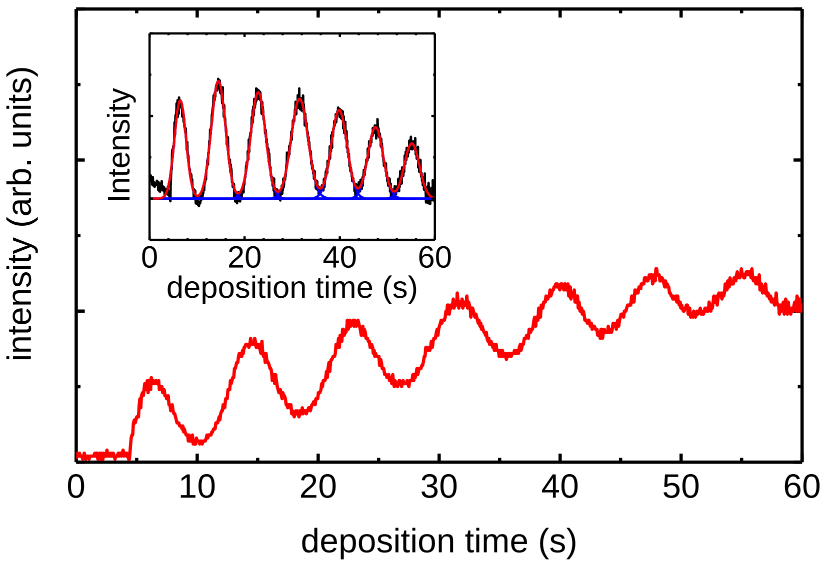

Fig. 4.12: RHEED oscillations observed for hafnia grown on *c*-cut sapphire under 0.3 Å/s Hf rate, 0.5 sccm oxygen flow rate, 250 W rf-power, and ~820 °C substrate temperature observed in Al_2O_3 [11-20] azimuthal direction. Inset: Same data but with subtracted background, blue lines are separate peak fits, red line represents the cumulative fit.

4.5.1.5 RHEED oscillations

Characteristic for layer-by-layer homo- or heteroepitaxial growth is the observation of RHEED oscillations during growth, leading to usually single crystalline thin films. In the case of HfO_2 on *c*-cut sapphire, RHEED oscillations correspond to heteroepitaxial growth. Figure 4.11 shows the integrated intensity of the central reflection of epitaxial hafnium oxide on *c*-cut sapphire in Al_2O_3 [11-20] azimuthal direction grown under 0.3 Å/s Hf rate, 0.5 sccm oxygen flow rate, 250 W rf-power, and ~820 °C substrate temperature. The integrated area used to obtain RHEED oscillations is exemplarily indicated by the blue rectangle shown in Fig. 4.11 (b). Clearly RHEED oscillations are identifiable in Fig. 4.12. Note that substrate temperature was increased by ~120 °C compared to the optimal substrate temperature, as described in section 4.3.1. Fitting the obtained growth oscillations (see inset of Fig. 4.12) allows to derive an oscillation period of 8.18 s. The *ex situ* calibrated growth rate of HfO_2 is calculated to 0.40 Å/s by the following relations.

monitored *in situ* Hf thickness : measured *ex situ* HfO_2 thickness = 1 : 1.32

→Hf rate : HfO_2 rate = 0.3 Å/s : 0.3x1.32 Å/s

Multiplying the calibrated HfO_2 growth rate of 0.40 Å/s with the oscillation period of 8.18 s, which denotes to one monolayer of (-111)-oriented HfO_2, yields to a layer thickness of 3.27 Å. This is in good agreement with the calculated (-111) lattice plane distance of *m*-HfO_2 of 3.13 Å, see Fig. 1.3. As the intensity of the growth oscillations damped with increasing film thickness, substrate temperature has been increased during growth in order to recover the initial RHEED oscillation amplitude. The matching of calibrated HfO_2 rate with the growth rate derived from the oscillation period and the (-111) lattice plane distance denotes clean epitaxial film growth for the initial layers.

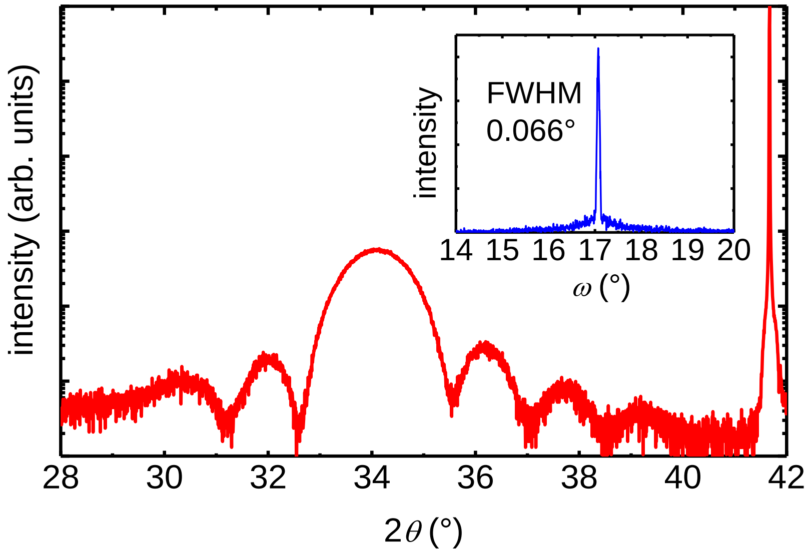

Fig. 4.13: 2θ–θ scan of a 5.5 nm thick, (200)-oriented hafnium oxide thin film grown on *c*-cut sapphire (Hf rate 0.1 Å/s, 1.0 sccm oxygen flow rate, 200 W rf-power, 700 °C substrate temperature). Laue oscillations indicate low surface & interface roughness and high crystallinity. Inset: Corresponding rocking curve of the (200) reflection of *m*-HfO_2.

4.5.2 (200)-oriented films of hafnia

Fig. 4.13 shows a 2θ–θ scan of a 5.5 nm thick hafnium oxide thin film grown on *c*-cut sapphire with 0.1 Å/s Hf rate, 1.0 sccm oxygen flow rate, 700 °C substrate temperature, and 200 W rf-power applied to the radical source. In contrast to the (-111)-oriented films grown on *c*-cut sapphire (see Fig. 4.7), the film grown under the mentioned growth conditions yields to single (200)-oriented films. This could be explained by the decreased Hf rate and the increased oxygen flow rate compared to the (-111)-oriented films, which will lead to stronger oxidation conditions during growth. A detailed description on how film orientation changes as a function of oxygen content is presented in section 5.

However, the obtained reflection maximum is at 34.098°, which is 0.259° lower in 2θ compared to the (200) reflection of *m*-HfO_2 from ICDD (00-034-0104). The difference in 2θ could either be explained by epitaxial strain leading to an increase in *d*, or by the stabilisation of another crystalline phase of hafnium oxide, such as orthorhombic, tetragonal, or cubic HfO_2. As all mentioned crystalline morphologies of HfO_2 do have minimum one reflection in the range of the observed reflection in Fig. 4.13, and only one reflection (and its higher order) could be observed over the full 2θ–θ range, it is not possible to definitely assign the observed reflection to one particular crystal morphology of HfO_2. As thicker and, thus, relaxed films grown under similar conditions show clear (00*l*) orientation, the observed reflection shown in Fig. 4.13 is assigned to *m*-HfO_2. However, the presence of Laue oscillations indicates high crystal quality and low surface & interface roughness. A FWHM of 0.066° of the corresponding rocking curve, given as an inset of Fig. 4.13, is another indication of high-quality and low mosaicity thin films. As already mentioned in section 4.5.1, it is challenging to perform in-plane measurements in reasonable time scales with sufficient statistics for film thicknesses below ~10 nm. As the determination of the epitaxial relation for (00*l*)-oriented films was not among the key targets of this study, no relaxation studies and in-plane measurements at thicker films were performed.

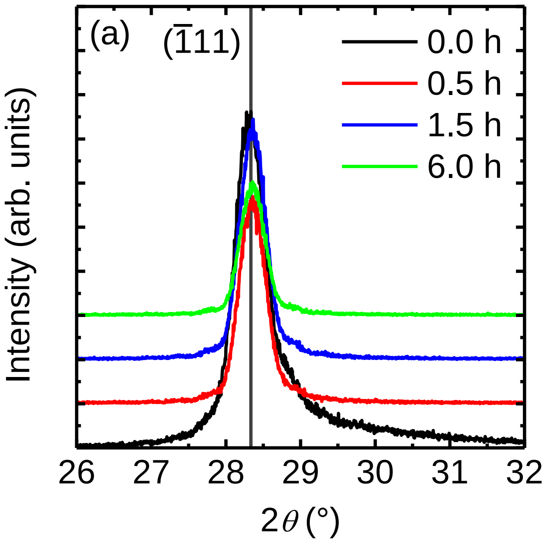

Fig. 4.14: (a) Zoom of the 2θ–θ scans of HfO_2 on *c*-cut sapphire (growth conditions see text) at different annealing stages. The (-111) reflection of *m*-HfO_2 becomes sharper and intensity decreases with increasing annealing time. (b) Corresponding rocking curves, indicating vanishing epitaxy and formation of two broad reflections with increased annealing time.

4.5.3 Annealing experiments

As an alternative to the lowering of the deposition rates, post deposition annealing experiments have been conducted in order to improve crystallinity of hafnium oxide thin films on *c*-cut and *r*-cut sapphire. The idea was to allow recrystallisation and crystal growth of as-deposited films via the supply of thermal energy, which is common practice for ALD/CVD-grown thin films of HfO_2. Two samples of hafnium oxide thin films on *c*-cut and *r*-cut sapphire grown under 0.1 Å/s Hf rate, 0.5 sccm oxygen flow rate, 200 W rf-power, and ~700 °C substrate temperature have been annealed in air at 1000 °C in a muffle furnace. Annealing time has been increased from initially 30 minutes to 90 minutes and 360 minutes. Samples have been inserted in a pre-heated muffle furnace at 1000 °C and have been quenched subsequently after elapsed annealing time to ambient temperature to achieve exact annealing time control. After each annealing step, samples were investigated by RHEED to check whether surface morphology changes as a function of thermal annealing.

Fig. 4.14 (a) shows the evolution of the (-111) reflection of *m*-HfO_2 on *c*-cut sapphire as a function of annealing time. The normalised intensity of the (-111) reflection decreases continuously with increasing annealing time, no shift in 2θ could be observed. Crystal quality worsens with annealing time, contrary to the initial expectations that annealing should improve crystallinity. The corresponding rocking curve in Fig. 4.14 (b) supports this result, as the narrow Bragg peak of the hafnium oxide film (black curve) vanishes after the first annealing step. The broad portion of the rocking curve, which is corresponding to the dislocation density, splits into two reflections, whose intensities decrease as a function of annealing time. The splitting of the rocking curve could be explained by the formation of two differently oriented textures of polycrystalline HfO_2 on *c*-cut sapphire, but with low mosaicity. The epitaxial relation is lost and the film relaxes by the formation of grain boundaries. RHEED studies after each annealing step suggest an increase in surface roughness with increasing annealing time, as more spots appear and streaks vanish. It seems to be that epitaxial films grown under the

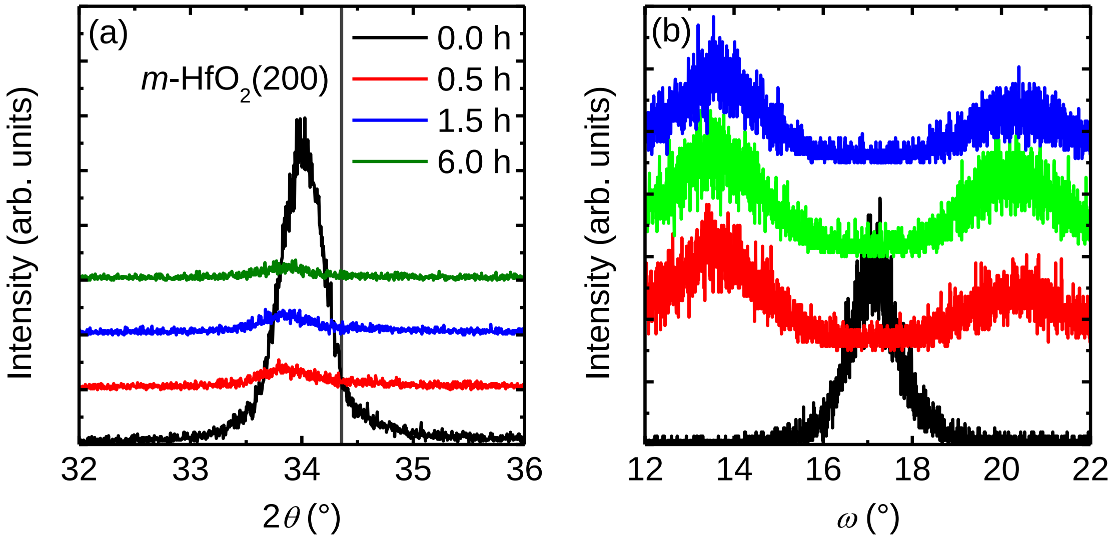

Fig. 4.15: (a) Zoom of the 2*θ*–*θ* scans of HfO_2 on *r*-cut sapphire (growth conditions see text) at different annealing stages. Intensity decreases rapidly with increasing annealing time. (b) Corresponding rocking curves, indicating a formation of two broad reflections after 30 minutes of annealing.

mentioned growth conditions are metastable and destabilise (relax) when providing thermal energy. The addition of thermal energy could foster the transformation into a thermodynamically more favourable state with lesser crystallinity and lower grade of texture. Alternatively, a chemical reaction between Al_2O_3 substrate and HfO_2 could take place. In the case of HfO_{2-x} thin films, HRTEM studies reveal significant oxygen diffusion from Al_2O_3 into HfO_{2-x}. However, such a chemical reaction could not be proven by X-ray diffraction. A much more detailed interface analysis would be needed, which was beyond the scope of this study.

Fig. 4.15 (a) shows the evolution of the (200) reflection of *m*-HfO_2 on *r*-cut sapphire as a function of annealing time. In contrast to the film on *c*-cut sapphire, X-ray intensity decreases abruptly after 30 minutes of annealing time, further annealing does not significantly change peak intensity anymore. A slight shift in 2θ towards higher *d*-values could be observed for 30 minutes of annealing time. Similar to the observations for films grown on *c*-cut sapphire under low Hf rate and comparably high oxygen flow rate as depicted in Fig. 4.13, the observed reflection is 0.348° lower in 2θ compared to the (200) reflection of *m*-HfO_2 from ICDD data (pdf 00-034-0104). Although there is a significant difference in 2θ for the observed reflection, other crystallographic phases of hafnia do not exhibit reflections which are significantly closer to the observed one. Even after thermal annealing, the peak position does not significantly shift towards the *d*-value of the *m*-HfO_2 (200) reflection known from ICDD data. The corresponding rocking curve shown in Fig. 4.15 (b) has a FWHM of more than 1.5° for the as prepared film (black curve), which suggests that the crystal quality of hafnium oxide is worse than compared to that of films grown on *c*-cut sapphire. Similar to the findings for the film on *c*-cut sapphire (see Fig. 4.14), the rocking curve splits into two maxima, whose intensities decrease as a function of annealing time.

In both cases, films on *c*-cut sapphire and *r*-cut sapphire, post deposition annealing worsens crystal quality of the films and leads to further film relaxation.

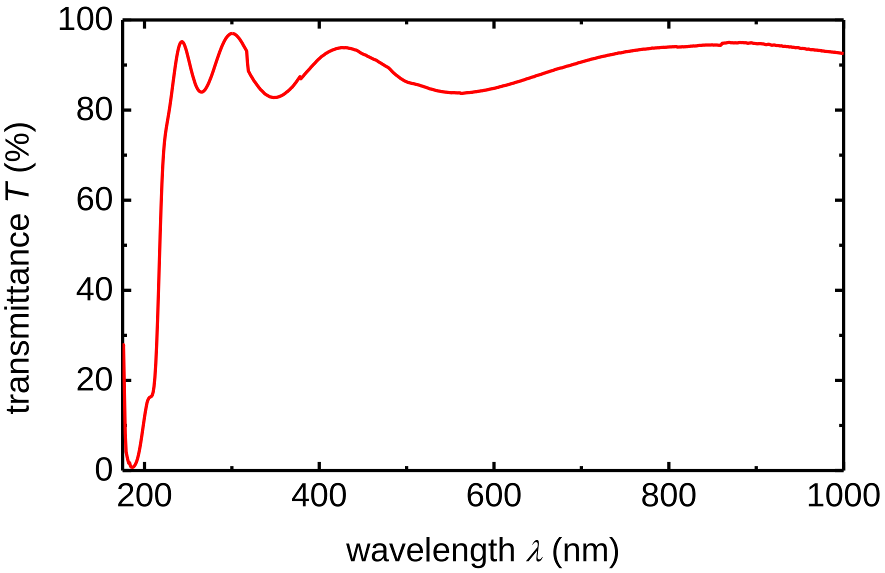

Fig. 4.16: Exemplary transmittance vs. wavelength spectrum for a 200 nm thick hafnium oxide thin film grown on *c*-cut sapphire.

4.6 Physical properties of HfO_2 thin films

This section gives an overview of optical band gap, electrical resistivity, dielectric permittivity and magnetisation of stoichiometric HfO_2 thin films grown for this study. Most of the mentioned physical properties have been investigated in detail for oxygen deficient HfO_{2-x} and results are presented in section 5.

Optical band gap

Stoichiometric HfO_2 is an insulator and a wide band gap material with a band gap of around 5.7 eV.[199] Lots of studies regarding the optical band gap of hafnium oxide have been conducted, a recent overview of the applied techniques is presented by Cheynet *et al.*[36] However, the focus of most studies is the investigation of absorption features near the absorption edge of the optical band gap and the comparison between single crystalline, polycrystalline, and amorphous thin films.[37, 200] Hullavarad *et al.* report on a 3 to 4% increase in transmission within the wavelength range of 300 to 800 nm as a function of post deposition annealing in molecular oxygen at 500 °C for PLD-grown thin films of HfO_2.[201] Note that in this study no change of the optical band gap (5.8 eV) with oxygen annealing has been reported. For this study, absorption measurements using a photospectrometer in transmission geometry have been conducted. In order to reduce absorption due to molecular oxygen and water vapour for wave lengths below 200 nm, the sample chamber has been flushed continuously with nitrogen gas. For the determination of the reflected portion, R, and the absorbed portion, A_{sub}, resulting from the sapphire substrates, background measurements with bare substrates have been performed.

Fig. 4.16 shows the transmittance of a 200 nm thick hafnium oxide thin film grown under 0.7 Å/s Hf rate, 2.0 sccm oxygen flow rate, 200 W of rf-power, and 700 °C substrate temperature. The transmittance stays at around 100% for wavelengths between 250 and 1,000 nm. Clearly interferences in transmittance are obtained due to vicinity of radiation wavelength

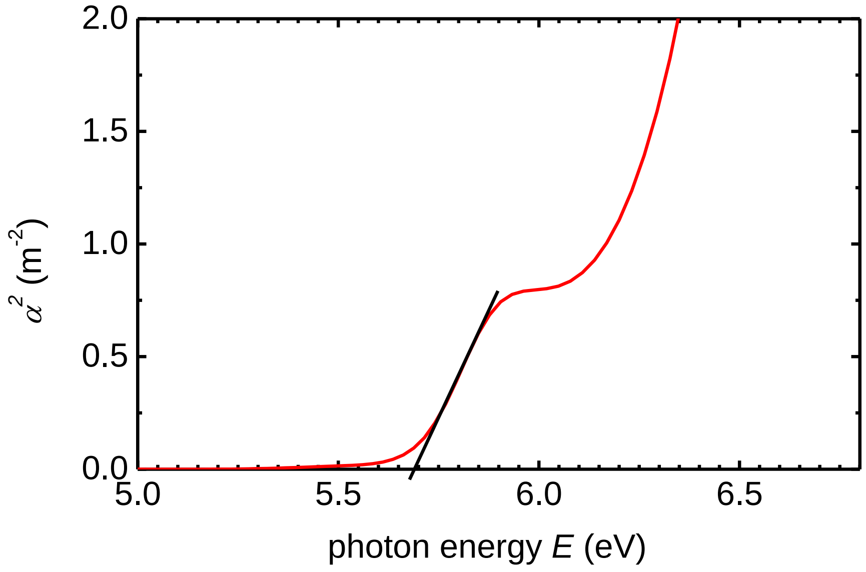

Fig. 4.17: Corresponding squared absorption coefficient α^2 vs. irradiation energy E plot to the transmittance spectrum shown in Fig. 4.16 including linear extrapolation of the absorption edge.

and film thickness. The kink observed at 375 nm is a measurement artefact, as the photospectrometer changes the monochromator at this specific wavelength. The increase in transmittance for very low wavelengths is due to re-emission from molecular oxygen residuals within the optical path. The optical band gap determination was carried out by extrapolating the linear part of the α^2 vs. radiation energy function considering direct band gap, parabolic valence, and conduction bands.[159, 160] Fig. 4.17 shows the corresponding squared absorption coefficient α^2 vs. irradiation energy E plot to the transmittance spectrum shown in Fig. 4.16 including the linear extrapolation of the observed feature. The linear extrapolation of the absorption edge yields to a optical band gap of ∼5.7 eV, denoting to stoichiometric HfO_2.

Electrical resistivity

Electrical characterisation for film resistivity determination has not been performed, as electrical resistivities of more than 10^8 $\mu\Omega$cm could not be obtained with the existing ρ–T measurement equipment (see section 3.3), whereas resistivities for stoichiometric HfO_2 are in the range of 10^{18} $\mu\Omega$cm. However, no measureable resistance has been obtained for stoichiometric HfO_2 thin films using simple two probe measurements.

Magnetisation

Magnetisation studies have been performed for films grown on *c*-cut and *r*-cut sapphire substrates. Figure 4.17 shows exemplarily magnetisation data obtained at 50 K for a 200 nm thick stoichiometric HfO_2 thin film grown on *c*-cut sapphire under optimal growth conditions (see section 4.3.5) of 0.7 Å/s Hf rate, 1.5 sccm oxygen flow rate, 200 W rf-power applied to the radical source, and 700 °C substrate temperature. Pure diamagnetic behaviour of HfO_2 is observable, as expected for stoichiometric, undoped HfO_2.

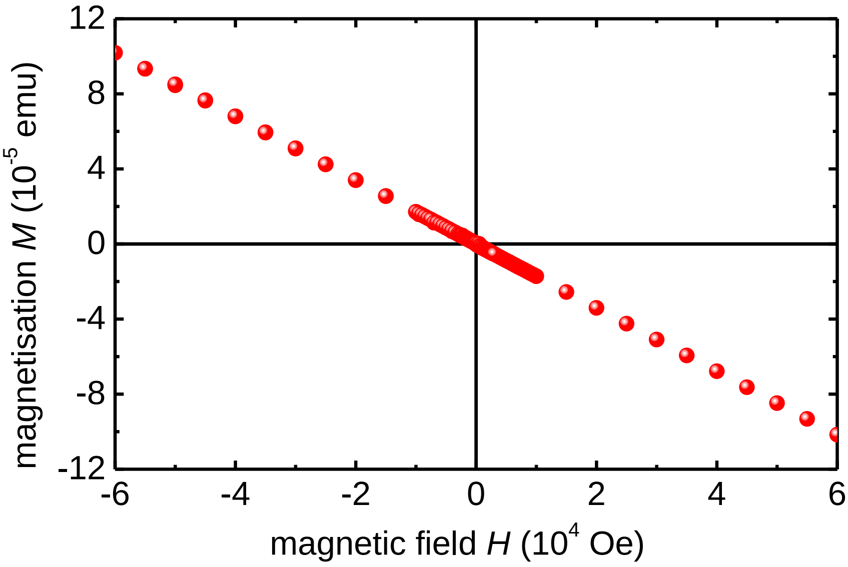

Fig. 4.18: Magnetisation data obtained at 50 K for a 200 nm thick HfO_2 thin film grown on *c*-cut sapphire under the optimal grwoth conditions mentioned in section 4.3.5. Clear diamagnetic behaviour is observed.

Dielectric permittivity

For HfO_2 used as a gate dielectric, knowledge about the electrical permittivity of the HfO_2 thin film is vital, as κ strongly influences later device performance. Apparently the determination of the dielectric permittivity of a solid thin film is rather easy, exemplary methods are ellipsometry in reflection geometry, and capacitance measurements of a MIM structure, just to name two. However, for device performance the *effective dielectric permittivity* is critical, of which the permittivity of pure HfO_2 is just one contribution. The formation of interfacial layers, oxygen gradients, and different material morphologies (crystallinity) are other key factors which need to be considered when determining the effective permittivity. As the intention of this study was not the utilisation of HfO_2 as a gate dielectric, no device related studies have been performed, and, thus, no measurements of the effective dielectric permittivity were conducted. The determination of κ for pure HfO_2 via the fabrication of a MIM structure prompts for conductive bottom and top electrodes. As the utilised substrates have been mainly sapphire, which is highly insulating, no such measurements could be made based on HfO_2 on Al_2O_3. Very often such MIM structures are established with highly doped silicon as bottom electrode and, e.g., gold or silver films deposited on top of the film as top electrodes. Attempts to grown stoichiometric HfO_2 on p^{++} Si have been conducted to get a rough estimation on the dielectric permittivity of RMBE-grown HfO_2. As no stripping facilities were available, the utilised p^{++} substrates exhibited a SiO_2 passivation layer of a few nm thickness. The presence of a defined SiO_2 interfacial layer would not be that crucial, as it could be considered in the later permittivity calculations. Deposition temperatures for these studies have been in the regime around 700 °C to make the results comparable with similar studies conducted on sapphire substrates. Such high deposition temperatures enhance interdiffusion processes between Si, SiO_2, and HfO_2, yielding to a change of the interfacial SiO_2 layer in thickness and permittivity. The presence of a SiO_2 interfacial layer, which alters as a function of deposition temperature and time, strongly influences all measured values for dielectric permittivity. Due to this effect, no meaningful values of κ could be obtained and, therefore, this direction has not been followed up any further.

Summarising the results of section 4, clean films of hafnium oxide were grown on various substrates, whereas oxygen stoichiometry has been proven by optical band gap measurements yielding to a band gap of $\sim$5.7 eV known for stoichiometric HfO_2. It was possible to grow even epitaxial films of hafnia on *c*-cut sapphire, yielding to films with very high crystal quality. Cleanliness of the obtained films in terms of ferromagnetic impurities has been demonstrated by magnetisation measurements and SIMS studies, revealing no significant traces of magnetic impurities within the measurement resolution.

5 Growth of $HfO_{2\pm x}$ thin films

5.1 Introduction

In section 4 the results of the growth of stoichiometric HfO_2 thin films, mainly on *c*-cut sapphire substrates, are presented. The subsequent results indicate that changing oxygen content in hafnia exhibits extensive changes of physical film properties. During the study of the influence of oxygen flow rate on film structure, a change in film transparency and colour has been observed. This indicates that by reducing the oxygen content in hafnium oxide thin films presumably defects (oxygen vacancies) are introduced, which are responsible for the change in optical film appearance. Consequently, after establishing optimal growth conditions for stoichiometric HfO_2 thin films, the next step was to change stoichiometry in a controlled manner and investigate its impact on film structure, orientation, and various other physical properties.

This section starts with a detailed study of how $HfO_{2\pm x}$ film orientation on *c*-cut sapphire substrates can be influenced by oxygen stoichiometry. Next, the observed change in film colour is investigated via optical photospectroscopy, highlighting the change of optical band gap as a function of oxygen content. As the change in stoichiometry of hafnia goes likely hand in hand with the introduction of oxygen and/or hafnium defects, the electrical resistivity was monitored and correlated with oxidation conditions during growth. As conductive thin films of oxygen deficient nature were fabricated, the nature and properties of charge carriers are highlighted next. Once oxygen deficiency can be introduced in a controlled manner, verified by the reproducible variation of band gap and electrical resistivity, magnetisation measurements were performed to shed light on the (often controversially) debated d^0-ferromagnetism in deficient HfO_{2-x}. In the last part of this section all gained results of this section are qualitatively summarised, and based on these results a defect band model for oxygen deficient hafnium oxide is developed.

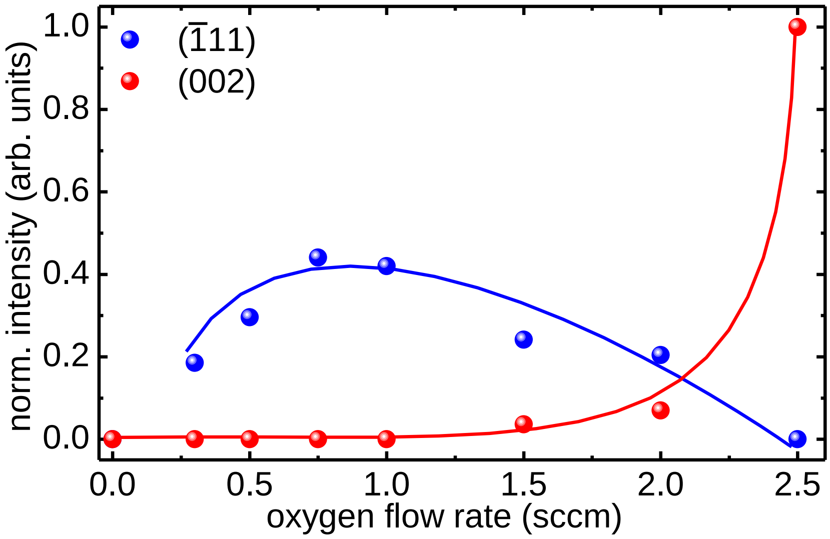

Fig. 5.1: Normalised intensities of (-111) and (002) reflections of 200 nm thick hafnia thin films as a function of oxygen flow rate (0.7Å/s Hf rate, 700 °C substrate temperature, 200 W rf-power for 0.25 to 2.0 sccm, 300 W rf-power for 2.5 sccm), solid lines are guides to the eye.

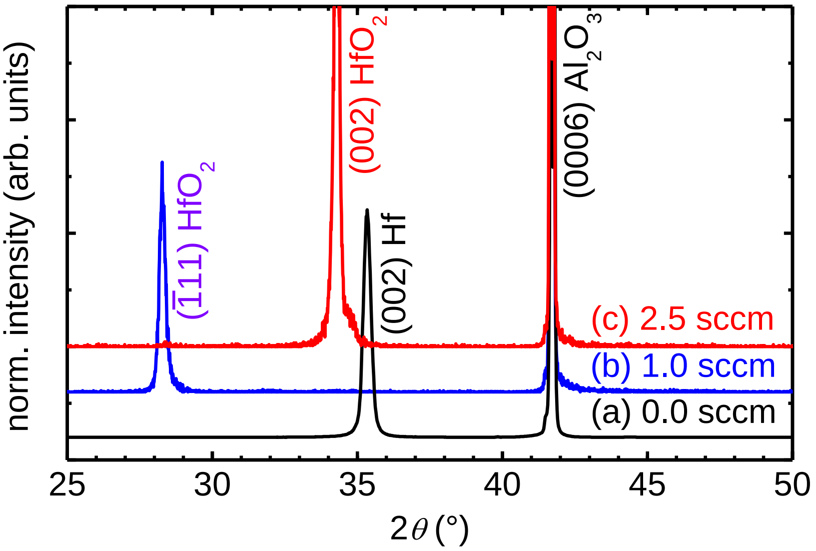

Fig. 5.2: Diffraction patterns for 200 nm thick hafnia thin films and 50 nm metal Hf demonstrating changing of film orientation as a function of oxidation conditions, (a) 0.0 sccm oxygen flow rate (metal hafnium); (b) 1.0 sccm, 200 W rf-power; (c) 2.5 sccm, 300 W rf-power. Other deposition parameters were 0.7 Å/s Hf rate and 700 °C substrate temperature.

5.2 Film orientation as a function of deficiency

Now, we focus on the influence of oxygen stoichiometry of hafnium oxide on thin film orientation on *c*-cut sapphire substrates. To do so, 200 nm thick films were grown with oxygen flow rates ranging from 0.25 to 2.5 sccm. Other deposition parameters were 0.7 Å/s Hf rate, 200 to 300 W rf-power, and 700 °C substrate temperature. All films were characterised by 2θ–θ out-of-plane measurements. Film thickness was increased compared to the studies described in section 4.3 in order to obtain more volume fraction for X-ray diffraction. Figure 5.1 shows the variation of the normalised intensities for the (-111) and (002) reflections of *m*-HfO_2 on *c*-cut sapphire substrates. The intensity of the (-111) reflection shows a maximum in the regime of 0.7 sccm oxygen flow rate, whereas the (002) reflection is absent up to a 1.0 sccm oxygen flow rate. At higher flow rates the (002) reflection starts to appear, and shows a steep increase in X-ray intensity for 2.5 sccm & 300 W rf-power. Note that for the sample grown under 2.5 sccm oxygen flow rate the rf-power applied to the radical source has been increased from 200 W to 300 W, yielding to extreme high oxidation conditions. In the regime of such high oxidation conditions, film orientation changes from (-111)-oriented hafnia to single (002)-oriented hafnia. As this study was not focussed on a systematic study of how film orientation changes with increasing oxidation conditions, only one film has been grown exemplarily in the regime of extreme high oxidation conditions. In addition, such high oxidation conditions may yield to the formation of hafnium vacancies and/or oxygen interstitials, rather than introducing oxygen vacancies, whereas the scope of this study is to introduce oxygen vacancies in HfO_{2-x} thin films.

As stated before, in the case of oxidation by oxygen radicals even for low oxidation conditions the formation of metallic hafnium was never observed. Only when utilising molecular oxygen instead of oxygen radicals, metallic hafnium forms (flow rates below 0.2 sccm). In the case of pure Hf metal evaporation without the provision of oxygen radicals or molecular oxygen (zero sccm oxygen flow rate), pure metallic hafnium stabilises in its hexagonal phase in

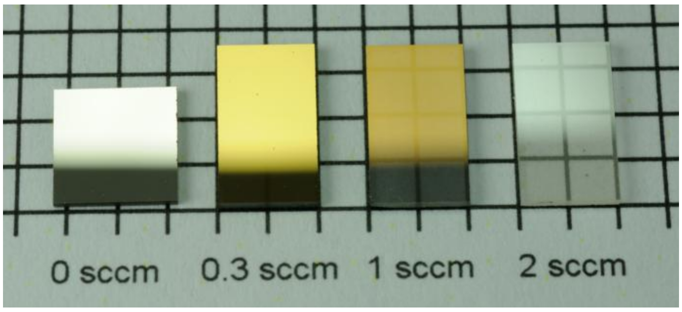

Fig. 5.3: Photograph of three $HfO_{2\pm x}$ hafnium oxide thin films on *c*-cut sapphire; 0.3 sccm oxygen flow rate for highly reduced growth conditions, 1 sccm for reduced, and 2 sccm for moderate oxidation conditions. For comparison a metallic Hf film is shown (0 sccm).

(002) orientation, see Fig. 5.2. As evident from Fig. 5.2, thin film orientation can be changed as a function of oxidation conditions, from (-111)-oriented films obtained for 0.7 – 1.0 sccm oxygen flow rate to (002)-oriented films grown under highly oxidising conditions (2.5 sccm, 300 W rf-power). In no case any other crystalline phases of hafnia could be observed, regardless of its oxygen content. Reports on the stabilisation of thermodynamically unstable phases like cubic or tetragonal HfO_2 under ambient conditions utilising high-energy ion beam assisted deposition could not be reproduced.[50, 202] In addition to *c*-cut sapphire substrates, also *r*-cut sapphire substrates were used for the investigation of film orientation as a function of oxidation conditions. Films on *r*-cut sapphire substrates showed poorer crystal quality, as evident from X-ray data.

5.3 Optical properties

5.3.1 Film appearance

When having a look at the grown 200 nm thick films, one notices a darkening and change in colour of the films as a function of decreased oxidation conditions during growth. In Fig. 5.3 three hafnium oxide thin films grown under different oxidation conditions are shown. An oxygen flow rate of 2.0 sccm leads to transparent (close to stoichiometric) thin films, 1.0 sccm leads to slightly darker and less transparent films, and 0.3 sccm leads to dark, non-transparent thin films with a golden shine. As a reference, a 50 nm thick, pure metallic hafnium film is added to Fig. 5.3 (corresponding to 0 sccm). Film darkening in hafnia as a function of oxidation conditions during growth, to our knowledge, has only been observed by Hadacek *et al.*[203] They report a slight grey appearance for films grown under UHV conditions with PLD. In comparison, for oxygen deficient $SrTiO_{3-\delta}$, a change in colour as a function of oxygen deficiency has been reported, where a glistening oxidised gem is turned into a dull blue, conductive crystal.[204] The colour change in HfO_{2-x} as a consequence of the formation of mid-gap defect bands due to oxygen vacancies allowing absorption at energies above 2 eV (620 nm) is discussed in detail in section 5.6.

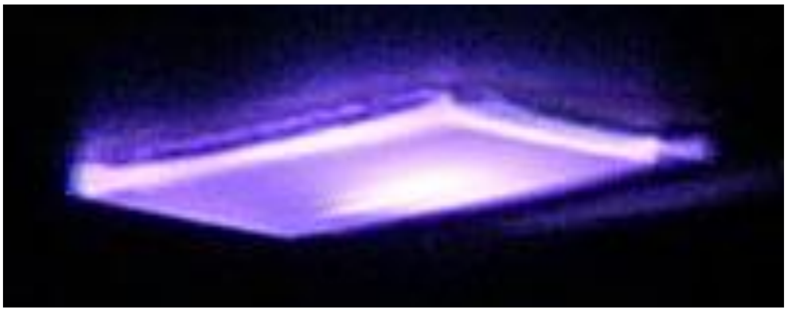

Fig. 5.4: Exemplary image of cathodoluminescence of a reduced HfO_{2-x} thin film on *r*-cut sapphire substrate irradiated by 30 keV electrons from RHEED gun. The same effect is also observed for oxygen deficient films on *c*-cut substrates.

5.3.2 Film Luminescence

An eye-catching observation of cathodoluminescence (CL) in an oxygen deficient HfO_{2-x} thin film on *r*-cut sapphire is shown in Fig. 5.4. Irradiation with 30 keV electrons from RHEED gun evokes CL in HfO_{2-x} due to the presence of oxygen vacancies. The CL intensity under RHEED electron beam irradiation scaled with the oxidation conditions during growth, from no CL for presumably stoichiometric films to a prominent lavender shine for highly reduced films. This increase in CL with increasing oxygen vacancy concentration is in good agreement with similar studies for $SrTiO_{3-x}$.[205]

5.3.3 Optical band gap

In this section we focus on the evolution of the optical band gap as a function of oxygen content in $HfO_{2\pm x}$ thin films. For deficient films of HfO_{2-x}, film thickness was reduced from 200 nm to 30 nm, because the transmitted intensity for highly reduced samples (a few per cent) is too low for reasonable transmission measurements.

Fig. 5.5 (a) to (d) shows selected transmission spectra obtained for hafnium oxide thin films grown under various oxidation conditions in the range of 175 to 400 nm. The transmitted intensity is highest for stoichiometric HfO_2 (1.5 sccm, see Fig. 5.5 (c)), for extreme high oxidation conditions (2.5 sccm, 300 W, see Fig. 5.5 (d)) or lower oxidation conditions (0.5 sccm, see Fig. 5.5 (a) and 1.0 sccm, see Fig. 5.5 (b)) the transmittance decreases. The optical band gap determination was carried out by extrapolating the linear portion(s) of the α^2 vs. radiation energy function considering direct band gap, parabolic valence, and conduction bands.[159, 160] Fig. 5.5 (e) to (h) shows the corresponding dependencies of the squared absorption coefficient, α^2, as a function of the irradiation energy, E, for the films shown in (a) to (d). For reduced growth conditions, two separate absorption features can be identified, extrapolating to 4.95 and 5.25 eV, see Fig. 5.5 (e). The presence of two features near the absorption edge has been reported earlier for sputtered hafnium oxide thin films studied as a function of the oxygen to argon ratio.[206] However, these features did not show a dependence on oxygen to argon ratio, indicating that the investigated films were not of sufficient oxygen deficient nature to give rise to a significant change of the optical band gap, E_g. In this study, a remarkable narrowing of the optical band gap of oxygen deficient HfO_{2-x} of more than 1 eV from 5.7 eV in the stoichiometric case to values as low as 4.5 eV was observed.

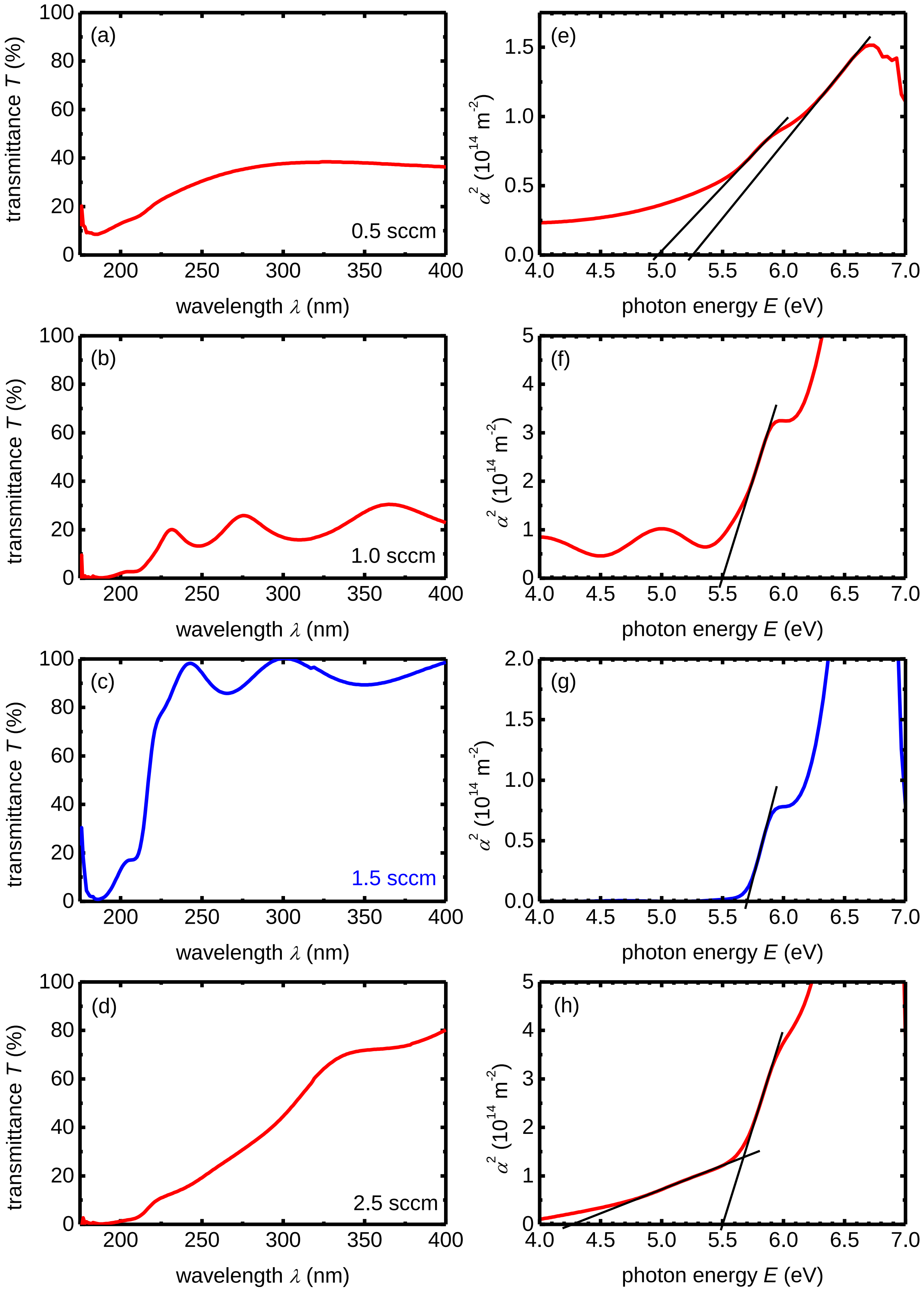

Fig. 5.5: (a) to (d) transmittance vs. wavelength spectra for hafnium oxide thin films grown under different oxidation conditions (0.5; 1.0; 1.5; 2.5 sccm), (e) to (h) corresponding squared absorption coefficient vs. irradiation energy plots including linear extrapolation of the absorption edges. Blue graphs shown in (c) and (g) represent stoichiometric HfO_2.

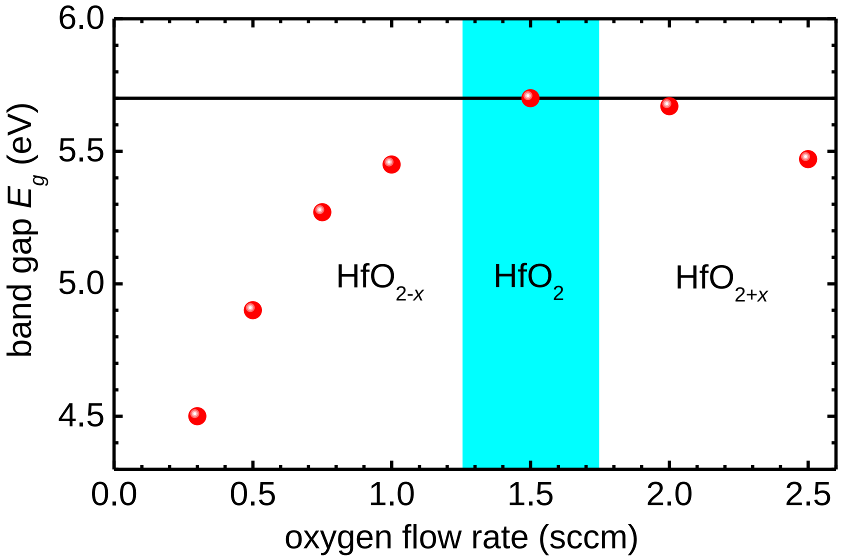

Fig. 5.6: Band gap vs. oxygen flow rate of $HfO_{2\pm x}$ thin films. The horizontal line indicates a band gap of ~5.7 eV known for stoichiometric HfO_2, whereas the shaded area represents the regime of oxygen flow rate leading to presumably stoichiometric thin films of HfO_2.

A change in optical band gap as a function of oxidation conditions in a limited range of 0.2 eV has been found for sputtered hafnium oxide,[60, 207] post deposition annealed PLD-grown hafnium oxide,[208] and titanium dioxide.[209] The described variations in optical band gap in the range of 0.2 eV suggest that it was not possible to introduce as many oxygen vacancies in HfO_{2-x} as in the case of RMBE-grown thin films. However, the trend of reduced optical band gap with decreasing oxygen content is similar to all studies. As discussed later, the optical band gap reduction is probably due to a hybridisation of in-gap defect states with the conduction band. Within the later described defect band model, the second observed feature could be attributed to a defect band formed within the optical band gap.

Fig. 5.6 shows the band gap E_g as a function of oxidation conditions represented by the oxygen flow rate supplied to the radical source. A parabolic dependence with a maximum around 5.7 eV for presumably stoichiometric HfO_2 is found. The observed decrease in band gap results either from oxygen vacancies in HfO_{2-x} or from hafnium vacancies/oxygen interstitials in HfO_{2+x}. Stoichiometric thin films of HfO_2 are not only obtained at one specific oxygen flow rate, but can be obtained in a growth regime around 1.5 sccm oxygen flow rate, as indicated by the shaded area in Fig. 5.6. These observations point to the evolution of in-gap defect bands which reduce the total band gap by hybridisation with the conduction or valence band. This scenario has been simulated for isolated defect states by density functional theory.[105, 113] The presence of defect states implies charge carriers which can be localised. The transition to extend defect states respective defect bands implies electric conductivity. The introduction of oxygen vacancies is usually associated with electron doping, as, for example, observed for $SrTiO_3$.[205]

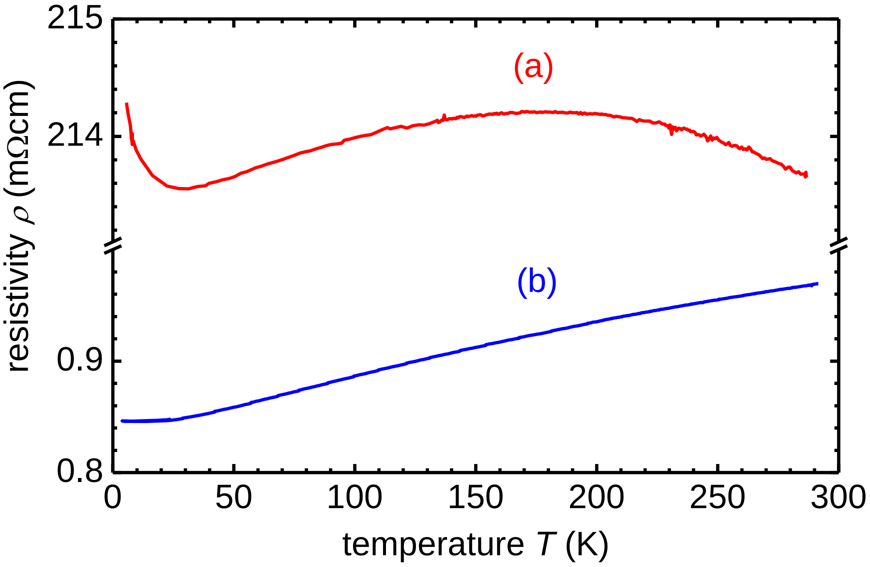

Fig. 5.7: Resistivity vs. temperature for 50 nm thick HfO_{2-x} films grown (a) under slightly reduced (0.91 sccm oxygen flow rate) and (b) under highly reduced (0.6 sccm oxygen flow rate) conditions. Other deposition parameters were 0.7 Å/s Hf rate, 200 W rf-power, and 700 °C substrate temperature.

5.4 Electrical properties

5.4.1 Film resistivity

The introduction of oxygen vacancies in HfO_{2-x} does likely create charge carriers in the investigated thin films. Stoichiometric HfO_2 is a well-known, transparent insulator with a resistivity in the range of 10^{18} $\mu\Omega$cm. In literature, the variation of resistivity vs. oxidation conditions during growth has been studied in the high-resistivity regime above 10^{15} $\mu\Omega$cm showing a decrease in resistivity for non-stoichiometric thin films.[145] Bharathi *et al.* observed resistivities in the range of 10^{9} $\mu\Omega$cm as a function of oxidation conditions for reactive sputtered films on quartz and stripped Si (100) substrates grown at temperatures up to 500 °C.[188] Their study describes a variation in conductivity of about 50% as a function of crystallite size. According to the presented absorption data and compared to this study, those samples are only slightly oxygen deficient. A formation of hafnium-based silicates due to diffusion could be an explanation for low resistivity. This would explain the missing (001) reflection for samples grown at elevated temperatures.

In the present study, films grown under lower oxidation conditions with decreased transparency and narrowed optical band gap, resistivities in the range of 10^{8} down to a couple of hundred $\mu\Omega$cm were measured. Please note that for resistivity studies pristine (un-annealed) *c*-cut sapphire substrates have been used. Figure 5.7 shows the thin film resistivity as a function of temperature for two different samples. At room temperature a resistivity in the range of 200,000 $\mu\Omega$cm is observed for slightly reduced films of hafnia (Fig. 5.7 (a)) which is almost temperature independent. At low temperatures, an upturn of the resistivity indicates a freezing of the charge carriers. Highly reduced samples show a clear metallic $\rho(T)$ behaviour (Fig. 5.7 (b)). The resistivity starts at ~1,000 $\mu\Omega$cm at room temperature and drops by around 12% to a residual resistivity of 840 $\mu\Omega$cm at 5 K. The resistivity of pure, bulk metallic hafnium is in the range of 35 $\mu\Omega$cm, well below the observed values for HfO_{2-x}.

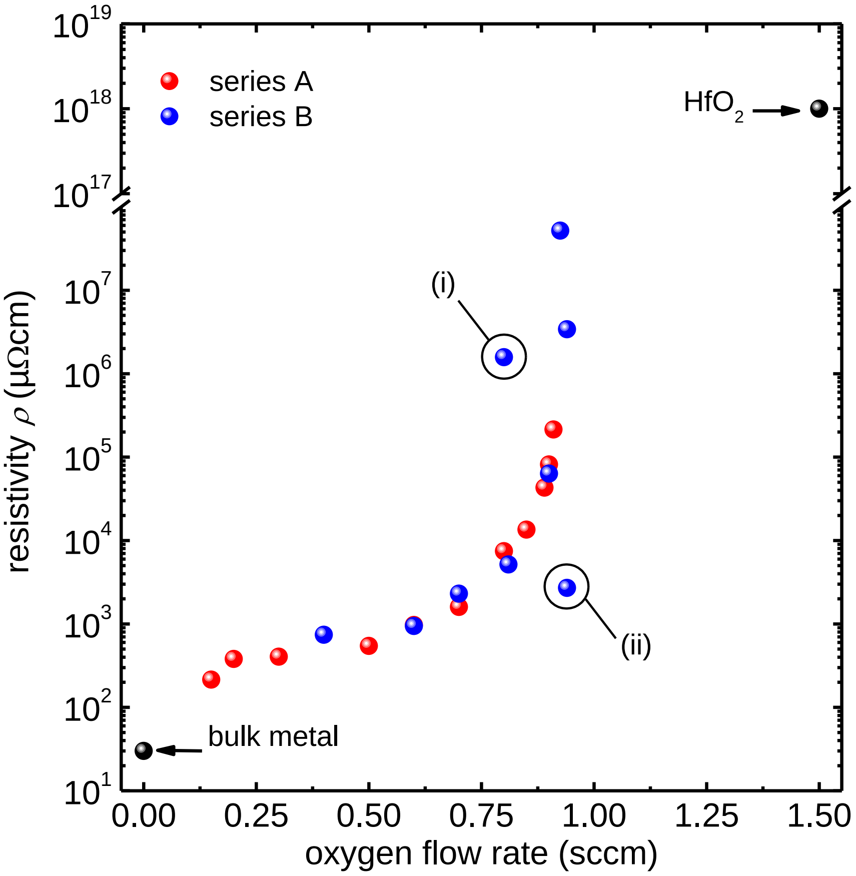

Fig. 5.8: Room temperature resistivity as a function of oxidation conditions for two growth series, A & B. Films below 0.6 sccm oxygen flow rate do show metallic ρ-T behaviour, whereas above this threshold no major change in ρ as a function of T is observed. For marked data points (i) and (ii) see text, please note the ordinate break between 10^8 and 10^{17} $\mu\Omega$cm. It is remarkable that the resistivity of hafnium oxide thin films grown by RMBE can be tuned over 17 orders of magnitude by introducing oxygen vacancies.

When having a closer look at the variation of room temperature resistivity as a function of oxidation conditions, one can observe an exponential increase of resistivity as a function of oxidation conditions, and, thus as a function of oxygen content in HfO_{2-x} thin films. This trend is shown in Fig. 5.8, literature resistivities for metal Hf (35 $\mu\Omega$cm) and stoichiometric HfO_2 (10^{18} $\mu\Omega$cm) are added for better clarity (black points). Please note the ordinate break from 10^8 to 10^{17} $\mu\Omega$cm. Although films were deposited with oxygen flow rates from 0 sccm up to 2.5 sccm, resistivity could only be measured for films grown under ~0.9 sccm oxygen flow rate or lower with the existing R-T measurement setup (denoting to maximum resistivities of 10^8 $\mu\Omega$cm). Red points in Fig. 5.8 represent data collected for thin film series A, whereas blue points represent data collected for a second thin film series, B, grown one year later than series A. Both series yield to similar ρ–T behaviour and magnitude, demonstrating the capabilities of RMBE in terms of process reproducibility. The marked data point (i) in Fig. 5.8 corresponds to a film deposited after several deposition runs without thickness re-calibration. As expected it does not match to the overall trend in resistivity as a function of oxygen flow rate. This could be explained by a drift in thickness calibration after several depositions, yielding to a drift of the monitored thickness by the rate thickness controller. A drift of the monitored thickness in turn can lead to a change in film stoichiometry at a given oxygen flow rate, as the monitored Hf metal rate differs from the actual Hf rate. This exemplarily demonstrates that regular thickness re-calibration is crucial to obtain reproducible growth conditions and, thus,

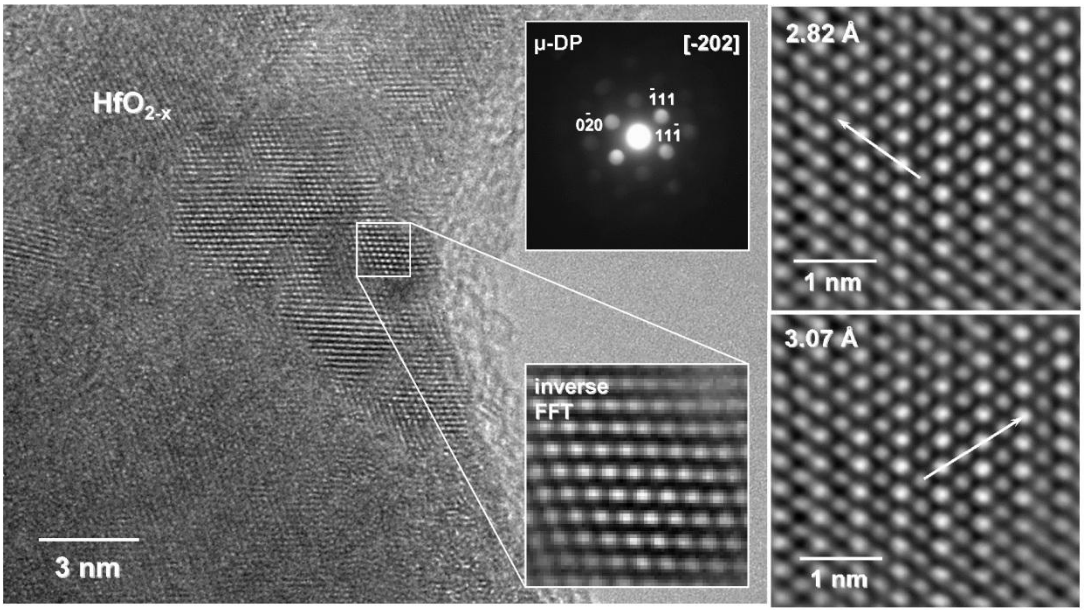

Fig. 5.9: HRTEM images of a conducting $HfO_{2\text{-}x}$ thin film. The upper inset reveals a micro-diffraction pattern confirming (i) the textured nature of the thin film and (ii) the formation of $HfO_{2\text{-}x}$ or a stable oxygen deficient phase of hafnia in contrast to metallic Hf. The enlarged inverse Fourier-transformed images shown in the lower image represent the lattice periodicity of one individual grain.

reliable resistivity data. The second marked data point (ii) in Fig. 5.8 has been obtained for a film grown on an annealed *c*-cut sapphire substrate instead of a pristine substrate. Two substrates (annealed and pristine) have been simultaneously deposited utilising substrate rotation ensuring sample homogeneity. The hafnium oxide thin film on the pristine substrate exhibits a resistivity of 3.4 x 10^6 $\mu\Omega$cm, whereas the film grown on the annealed substrate yields to 2.7 x 10^3 $\mu\Omega$cm. Substrate surface quality seems to influence film resistivity, for annealed substrates film resistivities are lower compared to pristine substrates. Utilising annealed substrates could shift the metal-insulator transition towards higher oxygen flow rates.

One scenario which could give an explanation for such a tremendous decrease in resistivity in oxygen deficient $HfO_{2\text{-}x}$ thin films of more than 14 orders of magnitude is the possible presence of metal hafnium distributed in the film forming conductive current paths. A volume fraction of more than 20% of metal hafnium would be needed, assuming a statistical distribution in an HfO_2 matrix according to percolation theory.[210] In order to investigate this further, X-ray measurements were carried out to trace for crystalline metallic hafnium. In all cases, monoclinic hafnium oxide was identifiable. No impurity or metal Hf phases could be identified. However, there is still the possibility for a distribution of amorphous metallic hafnium in a stoichiometric HfO_2 matrix which would not be observable utilising X-ray diffraction. High-resolution transmission electron microscopy has been applied in collaboration with Prof. Kleebe, Institute for Geosciences, TU Darmstadt in order to rule out this scenario. HRTEM imaging confirmed that the films consist of highly textured grains, as verified by electron micro-diffraction. A tilting series was performed checking whether the film also contains an amorphous residue, verifying that the $HfO_{2\text{-}x}$ film shown in Fig. 5.9 was fully crystalline with no amorphous secondary phase present. The analysis of the lattice periodicity, as illustrated in the enlarged inverse Fourier-filtered images, demonstrates the formation of hafnia in contrast to metallic hafnium having a hexagonal closed packed structure. The atomic spacings of 0.282 and 0.307 nm only occur in hafnia and are not present in hafnium metal. However, those distances are slightly lower than in stoichiometric hafnia (0.282 vs. 0.283 and 0.307 vs.

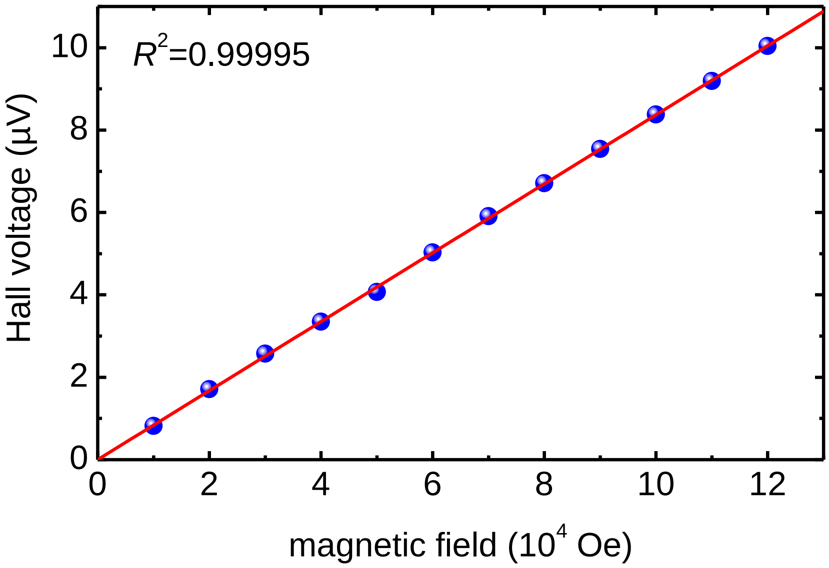

Fig. 5.10: Hall voltage obtained at 300 K as a function of the applied magnetic field of a 50 nm thick HfO_{2-x} thin film grown under 0.7 Å/s Hf rate, 0.25 sccm oxygen flow rate, 200 W rf-power, and 700 °C substrate temperature. No anomalous Hall effect can be observed.

0.314 nm), which can be correlated with either (i) the stabilisation of oxygen vacancies in *m*-HfO_{2-x}, or (ii) the formation of a stable, oxygen deficient phase of hafnia, such as Hf_2O_3. As, to our knowledge, there are no reports on Hf_2O_3 or comparable oxygen deficient phases in literature, no structural or X-ray data is available for comparison. All films were stable in air and were re-measured after 12 months, showing no change in physical properties.

5.4.2 Charge carriers

As evident from the resistivity measurements, the introduction of oxygen vacancies leads to the formation of charge carriers in HfO_{2-x} thin films, thus leading to conductivities exceeding values known for other semiconductors.[211] To clarify the nature of charge carriers in the oxygen deficient films, Hall measurements in van der Pauw geometry at 300 and 5 K have been carried out utilising a MPMS dewar with a field capability of ± 7 Tesla. The obtained Hall voltage as a function of the applied magnetic field follows linear behaviour, as shown in Fig. 5.10. No anomalous Hall effects could be observed. A positive Hall coefficient of R_H = 8.7 x 10^{-4} cm^3/C indicates holes as majority charge carriers with concentrations of 6 x 10^{21} cm^{-3} and mobilities of 2 $cm^2/(Vs)$ for a 50 nm thick HfO_{2-x} film grown under 0.7 Å/s Hf rate, 0.25 sccm oxygen flow rate, 200 W rf-power, and 700 °C substrate temperature on *c*-cut sapphire. Neither the Hall coefficient, nor the charge carrier concentration, nor the mobility changed as a function of temperature in the range of 5 to 300 K. The observed *p*-type conductivity is in agreement with earlier findings, claiming oxygen vacancies being responsible for electrical conductivity in HfO_{2-x}.[203] In contrast, Ko *et al.* emphasise the importance of charged point defects (oxygen interstitials or hafnium vacancies) responsible for high temperature conductivity, rather than oxygen vacancies.[212] Taking the charge carrier concentration of 6 x 10^{21} and the assumption that each oxygen vacancy traps one electron, one can roughly estimate the stoichiometry of this particular film to be x = 0.2. In literature, similarly stoichiometry values have been reported; however, in all these cases neither high conductivity nor a change in optical appearance was reported.[89, 202, 213]

It would be favourable to determine absolute values of oxygen stoichiometry, avoiding indirect methods as the estimation using the charge carrier concentration in highly deficient HfO_{2-x}. Various approaches have been made to determine the oxygen stoichiometry, in many cases X-ray photoelectron spectroscopy has been applied to monitor the O 1*s* and the Hf 4*f* band intensities and positions.[214, 215] These XPS studies can be carried out *in situ* or *ex situ*, in the latter case with or without sputtering for cleaning and/or depth profiling. Sputtered XPS has been applied to determine the stoichiometry of our RMBE-grown films in collaboration with Prof. Schröder, IHP, Frankfurt (Oder), but considered not to be accurate enough due to significant preferential sputtering of oxygen. Preferential sputtering leads to a measured decrease in oxygen content with increasing sputtering time, as evident from depth profiles. Preferential sputtering becomes more and more prominent for increased oxygen deficiency in the investigated films. The determination of x via *ex situ* XPS without sputtering is difficult because of the formation of a surface layer of fully oxidised HfO_2. This surface oxidation occurs when the samples are removed from the growth chamber. However, a shift of the O 1*s* signal as a function of increasing oxidation conditions to higher binding energies could be observed, which is in good agreement with prior findings in literature.[127] Miyake *et al*. report on the determinations of x in HfO_{2-x} via XPS resulting in $HfO_{1.535}$,[202] Capone *et al*. report even higher values of x resulting in $HfO_{1.454}$.[213] These values do not match well to our results, as from the amount of charge carriers our estimated deficiency is in the range of $x = 0.2$, which is more conservatively estimated avoiding unreliable results from XPS of oxygen deficient hafnia.

5.5 Magnetisation

Based on the results described in the previous sections, oxygen vacancies are introduced into hafnium oxide thin films grown by RMBE in a controlled and reproducible manner. Consequently, this allows the investigation of possible d^0-ferromagnetism in undoped transition metal oxides, which is attributed to the presence of oxygen vacancies.[77, 82, 216] Recently, supplementary to the claim of d^0-ferromagnetism for undoped oxides, room temperature ferromagnetism with dopants below the percolation limit, such as, Ni,[91] Co,[90] Fe[89] has caused significant interest in the scientific community. This paragraph describes the investigation of possible d^0-ferromagnetism in dopant-free, oxygen deficient hafnia. Prior to deposition, the composition of the used hafnium source and after deposition the resulting thin films have been investigated by SIMS in order to check for any above mentioned magnetic impurities, and no traces of any magnetic impurity (Fe, Ni, or Co) could be identified. After deposition, magnetisation data of a series of oxygen deficient HfO_{2-x} thin films has been obtained with a MPMS at various magnetic fields and temperatures. Handling samples with metallic tools can lead to a ferromagnetic feature as reported by Abraham *et al*.[84] Extreme care in sample handling was applied to avoid unwanted impurities of any kind. Figure 5.11 (a) to (d) shows magnetisation data obtained at 50 K for 200 nm thick hafnium oxide thin film grown under four different oxygen flow rates (0.3; 0.75 and 1.5 sccm at 200 W; 2.5 sccm at 300 W), other deposition parameters were 0.7 Å/s Hf rate and 700 °C substrate temperature. Note that the diamagnetic substrate contribution from sapphire has not been subtracted. Clearly, the linear diamagnetic behaviour known for diamagnetic and stoichiometric HfO_2 could be observed,

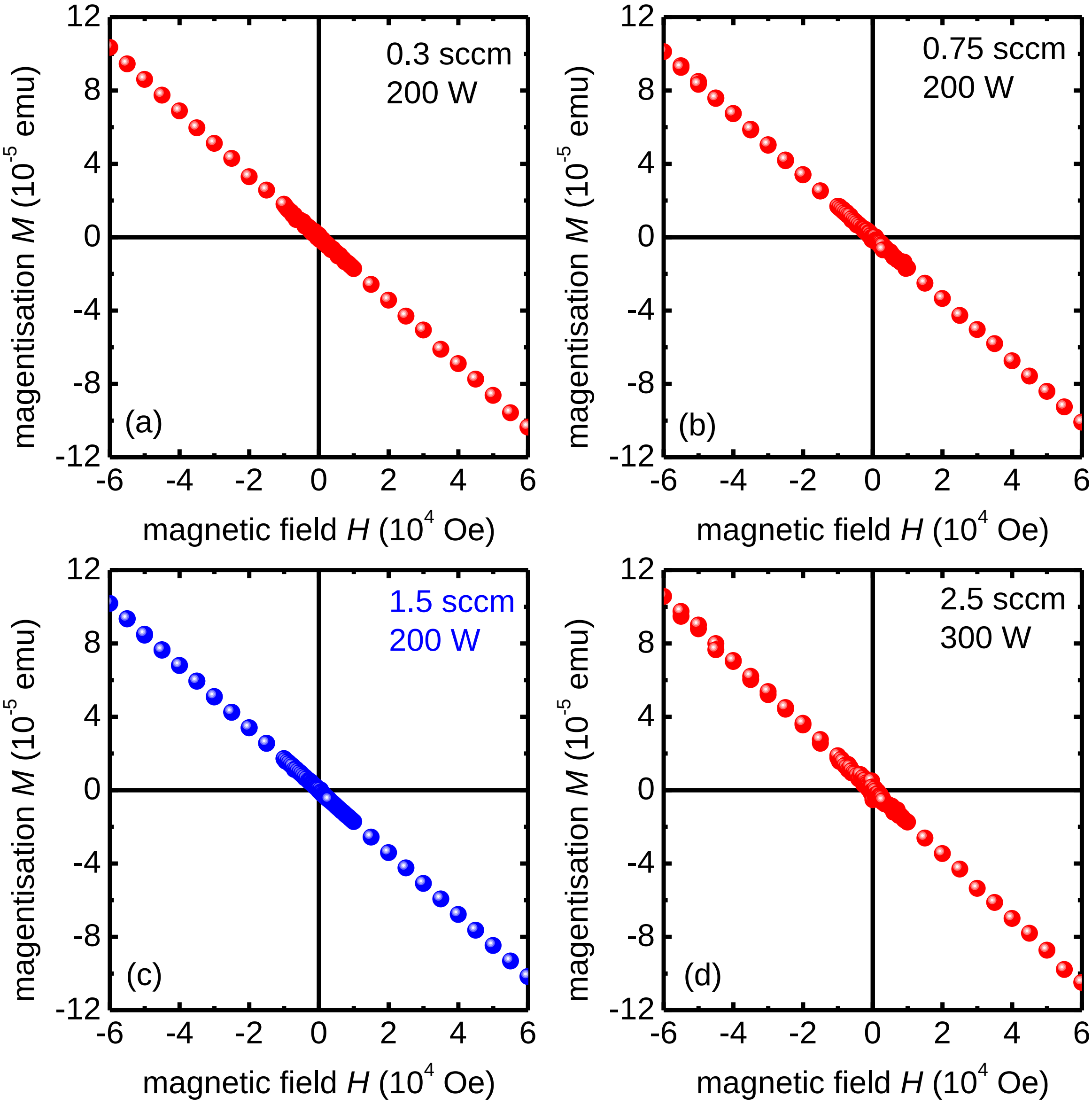

Fig. 5.11: (a) to (d) Magnetisation data obtained at 50 K for 200 nm thick hafnium oxide thin films grown under four different oxygen flow rates (0.3; 0.75 and 1.5 sccm at 200 W; 2.5 sccm at 300 W). Other deposition parameters were 0.7 Å/s Hf rate and 700 °C substrate temperature. The diamagnetic substrate contribution is not subtracted. All investigated films show diamagnetic behaviour, regardless of the oxidation conditions, (c) represents magnetisation data for stoichiometric HfO_2.

with no traces of ferromagnetic features, regardless of the oxidation conditions. The blue curve in Fig. 5.11 (c) corresponds to stoichiometric HfO_2, similar to Fig. 4.18 in section 4.6. This is in good agreement with results found in literature claiming the absence of d^0-ferromagnetism for undoped transition metal oxides.[203]

No temperature dependence of the diamagnetic signal could be observed in the range of 5 to 300 K (not shown). For this study numerous films have been deposited and regularly measured, all results fail to give any evidence for d^0-ferromagnetism in undoped hafnia. This finding stands for films grown under high and low oxidation conditions with oxygen radicals (oxygen flow rate between 0.2 and 2.5 sccm), including films showing a decreased band gap and very low resistivities.

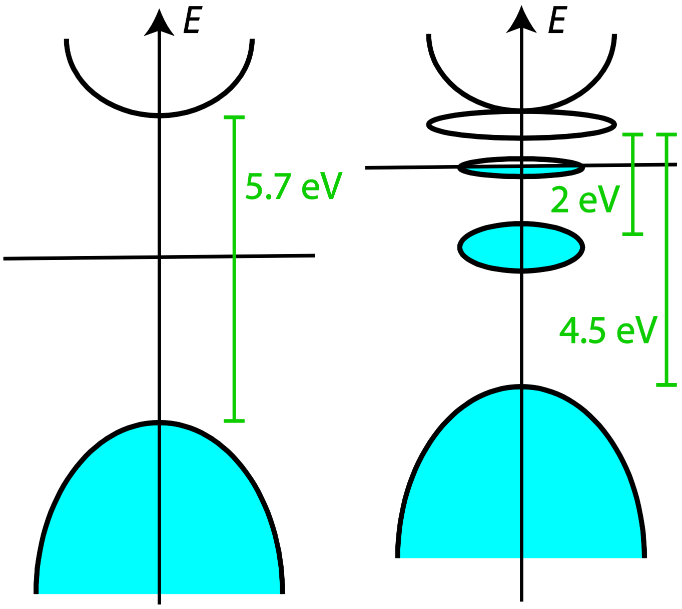

Fig. 5.12: Left side: Band model of stoichiometric HfO_2. Right side: simplified band model of oxygen deficient HfO_{2-x}.

5.6 Defect formation in oxygen deficient HfO_{2-x}

In order to understand the observed electrical conductivity, the decreasing optical band gap as a function of decreasing oxidation conditions, and the appearance of additional features in the α^2 vs. photon energy plots with decreasing oxidation conditions, a simple band structure model has been developed. The model is based on the existing knowledge of individual defect states in HfO_2 which, to our knowledge, has not yet been extended to high defect concentrations. There are mainly three different possible vacancies in hafnia, three-fold and four-fold coordinated oxygen vacancies, and a seven-fold coordinated hafnium vacancy. Oxygen vacancies in hafnia can be double or single positively charged (V_O^{++}, V_O^{+}), neutral (V_O), and single or double negatively charged (V_O^{-}, V_O^{--}), dependent on the number of trapped electrons. The corresponding energy levels have been calculated using the screened exact exchange and weighted density approximation methods within the local density formalism.[105] These methods have the advantage of giving the correct band gap of stoichiometric HfO_2. Similar results have been obtained by several groups.[106-108, 113] One electron level differences only provide a poor estimate of optical transition energies, therefore, time dependent DFT (TDDFT) has been applied leading to different absorption energies.[107] As an example, for V_O^{-} states the transition energy from occupied mid-gap states to the conduction band is calculated to be 3.54 eV via the one-electron level, whereas for TDDFT this energy is calculated to be 3.20 eV. In the case of low defect concentrations, the model of discrete defect states and corresponding energies is valid, whereas for very high defect concentrations as in the present study, defect states are likely to overlap and form defect bands. Calculations for the formation energies for the various oxygen vacancies as a function of Fermi energy predict that the single negatively charged defect V_O^{-} is favoured compared to the other four oxygen vacancy defects for a Fermi level placed near the conduction band.[105, 108] From these calculations one can assume that in highly oxygen deficient HfO_{2-x}, the V_O^{-} is the predominant defect. The overlapping of the defect states leads to two defect bands, one fully filled mid-gap band and one partially filled band in close vicinity of the conduction band, according to the one-electron level energy calculation.

In Fig. 5.12, the probable band structure of oxygen deficient HfO_{2-x} is summarised based on the experiments from this study. The large band gap of stoichiometric HfO_2 of 5.7 eV is reduced to 4.5 eV as experimentally observed. This reduction is most likely due to the hybridisation of defect states with the conduction band. The golden shine of the highly reduced samples as obvious from Fig. 5.3 requires an absorption edge of about 2 eV. This feature can be explained by transitions from the broadened mid-gap band to the conduction band. The Fermi level sits inside a second defect state band in the vicinity of the conduction band. Due to the more than half filling of this band, *p*-type charge carriers are obtained. Takeuchi *et al*. have performed spectroscopic ellipsometry on hafnia thin films identifying an absorption peak at 4.5 eV counted from the upper edge of the valence band.[217] The oxygen deficiency was controlled by the oxidation time of hafnium metal thin films. With increasing film deficiency the width of the defect band considerably broadens. An overall decrease in optical band gap with decreasing annealing time in oxygen could be observed as well. This picture is qualitatively in agreement with the results from this study.

6 Ni-doping of hafnium oxide thin films

6.1 Introduction

In section 5.5, d^0-ferromagnetism in undoped, oxygen deficient hafnium oxide thin films has been investigated, yielding to no evidence for high-T_c ferromagnetism in undoped Hafnia. The following section sheds light on the phenomenon of room temperature ferromagnetism in Ni-doped HfO_2 thin films. There is still disagreement about the physical explanation of room temperature ferromagnetism in doped, oxygen deficient transition metal oxides. Either the observed ferromagnetism is due to the ferromagnetic coupling of defect states (formed due to oxygen deficiency) with *d*-states from metal dopants (such as Fe, Ni, Co), or due to the formation of dopant clusters. Reliable statements on the origin of room temperature ferromagnetism in these materials can only be given when being sure about the distribution of the dopant in the matrix. Main focus of this study is to establish homogeneous doping of hafnium oxide matrices with Ni by a novel growth technique and comparing these results with results obtained for films grown with the 'classical' approach.

6.2 Growth of Ni-doped $HfO_{2\pm x}$

The growth of Ni-doped hafnia has been realised in two ways, at first by standard co-evaporation of Hf and Ni (first series), and second by co-evaporation of Hf and Ni utilising a stainless-steel screen placed between the Ni source and substrate (second series). Doping levels of 0 to 60 atom per cent were targeted resulting in, e.g., a deposition rate of 0.7 Å/s for Hf and 0.0084 Å/s for Ni in the case of a doping level of 4%. The co-evaporation of Hf and Ni without screen between Ni-source and substrate can lead to strong Ni rate fluctuations. As the Ni source has to be operated at very low rates, rate stability is strongly affected by chamber pressure. As described in section 2.5, the tooling factor is used to accommodate the difference in monitored evaporation rate obtained by the source QCM and the evaporation rate obtained

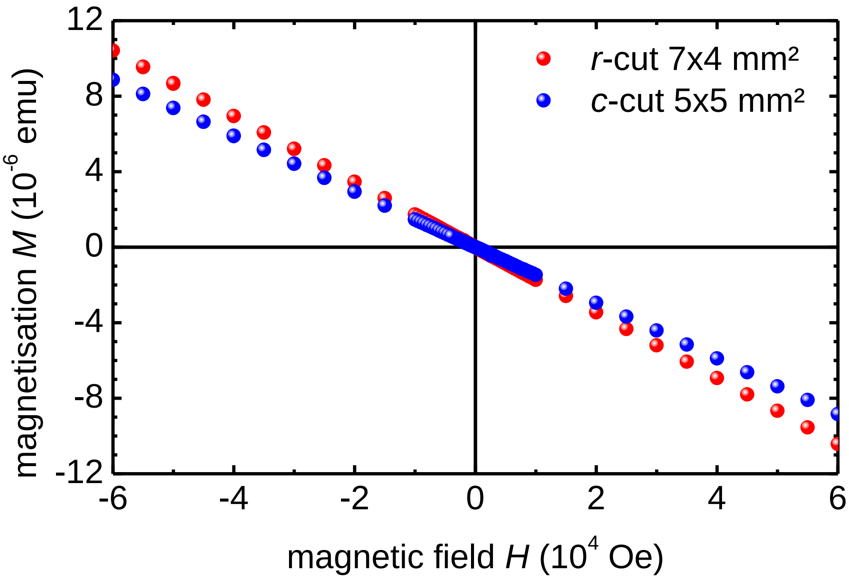

Fig. 6.1: Magnetisation data for bare *r*-cut (7x4 mm²) and *c*-cut (5x5 mm²) sapphire substrates showing a diamagnetic response. The difference in slope can be explained by the difference in mass of both substrates.

at substrate level. Utilising a screen placed spatially between the Ni source and substrate allows reducing the tooling factor by a factor of ten, thus, allowing the operation of the Ni source at (source QCM) deposition rates more than ten times higher, as the screen shields around 90% of the Ni flux.

As substrates, *c*-cut sapphire 7 x 4 mm^2 and 5 x 5 mm^2 single side polished have been used, treated in the same manner as described in section 4.2. Al_2O_3 single crystals exhibit superior crystal quality and material cleanliness, free of ferromagnetic contaminations. This is vital for the study of ferromagnetism in a diamagnetic matrix. Substrate cleanliness has been proven by subsequent magnetic characterisation of bare substrates prior to growth, yielding to as expected diamagnetic behaviour in all cases, see Fig. 6.1.

6.3 First series of Ni-doped $HfO_{2\pm x}$

As mentioned in the previous section, the first series of Ni-doped $HfO_{2\pm x}$ has been grown by co-evaporation of Hf and Ni with *in situ* oxidation using oxygen radicals. 50 nm thick Ni-doped $HfO_{2\pm x}$ thin films were grown testing four different oxidation conditions (0.5; 1.0; 2.0 sccm oxygen flow rate at 200 W, 2.0 sccm at 300 W rf-power), other deposition parameters were 0.7 Å/s Hf rate, 0.0168 Å/s Ni rate (corresponding to 8 atom per cent doping level), and 700 °C substrate temperature. Substrates were rotated continuously during deposition ensuring film homogeneity. Significant rate fluctuations of the Ni source have been observed during growth, which scaled with increasing oxygen partial pressure. Nevertheless, the ratio of the integrated thicknesses obtained by the thickness monitor for Hf and Ni yielded to the desired doping level of 8 atom per cent Ni in hafnia. Two substrates of the same type have been deposited in each run. Figure 6.2 shows exemplarily the 2θ–θ scan for a 50 nm thick hafnium oxide thin film doped with 8 atom per cent Ni on a *c*-cut sapphire substrate grown under 2.0 sccm oxygen flow rate, 200 W rf-power applied to the radical source, 0.7 Å/s Hf rate, 0.0168

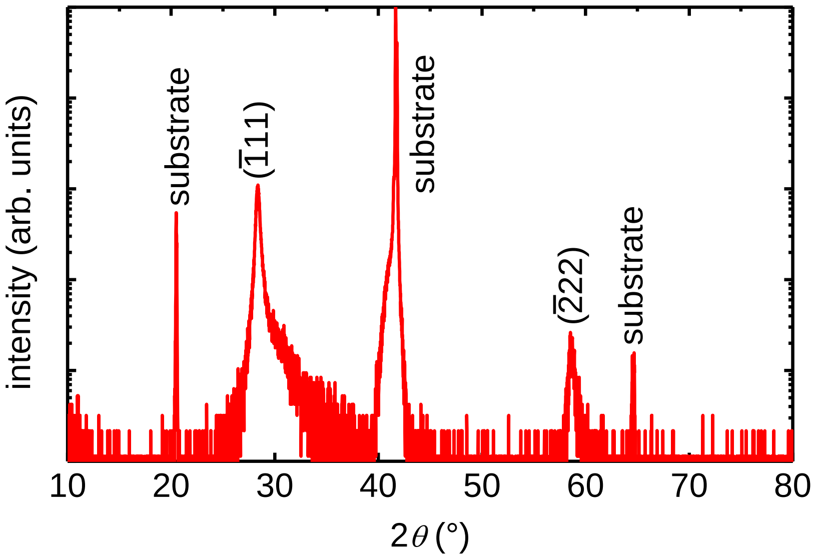

Fig. 6.2: 2θ–θ scan of a 50 nm thick hafnium oxide thin film doped with 8 atom per cent Ni grown on a *c*-cut sapphire substrate under 2.0 sccm oxygen flow rate, 200 W rf-power, and 700 °C substrate temperature. Besides substrate reflections, only (-111) and (-222) reflections of *m*-HfO_2 could be identified.

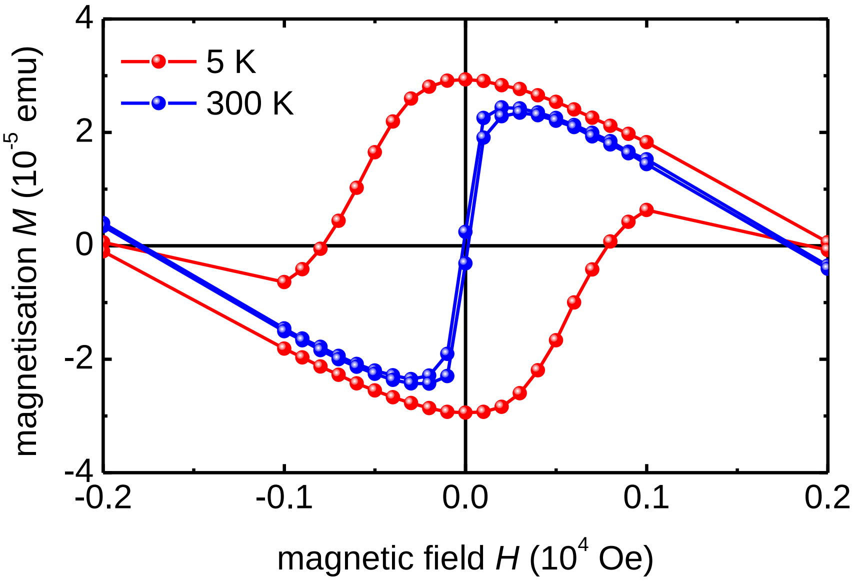

Fig. 6.3: Magnetisation data of a 50 nm thick HfO_2:8%Ni film on *c*-cut Al_2O_3 measured at two different temperatures, 5 and 300 K. In both cases a ferromagnetic hysteresis can be identified, whereas the coercive field increases with decreasing temperature. Note that the displayed data includes the diamagnetic contribution from the substrate.

Ni rate, and 700 °C substrate temperature. Besides the substrate reflections, only the (-111) and (-222) reflections of *m*-HfO_2 can be identified. As no traces of crystalline Ni or NiO could be identified within the X-ray resolution limit, the formation of crystalline Ni clusters inside a hafnium oxide matrix can be ruled out. These results hold for all four different oxidation conditions. Neither a change in crystal structure, nor the appearance of crystalline Ni or NiO could be observed.

Fig. 6.3 shows the magnetisation data of HfO_2 thin film doped with 8 atom per cent Ni grown under 2.0 sccm oxygen flow rate, 200 W rf-power, 0.7 Å/s Hf rate, 0.0168 Ni rate, and 700 °C substrate temperature. Clearly a ferromagnetic hysteresis can be identified. Note that the diamagnetic contribution of the substrate has not been subtracted. The coercive field increases with decreasing temperature, as lesser kinetic energy is provided to allow switching of the Weiß domains. Additionally, the magnetic remanence increased with decreasing temperature. The Curie temperature of the investigated film is above 350 K, as no transition could be observed up to 350 K (limit of the MPMS measurement setup). The second sample from the same deposition run has been characterised accordingly, leading to similar results for X-ray diffraction and magnetisation studies. As presented in section 4.6, stoichiometric hafnium oxide thin films do not exhibit a ferromagnetic feature, regardless of their oxygen content. Consequently, the observed ferromagnetic feature is due to the incorporation of Ni into the grown films. Samples grown under 0.5, 1.0 sccm at 200 W, and 2.0 sccm at 300 W rf-power did not show any ferromagnetic feature. The observation of a ferromagnetic feature for only one film could be explained by Ni rate fluctuations during film growth. A jump in the Ni rate during growth could lead to the provision of more Ni than what could be incorporated homogeneously into the film. Excess Ni could lead to the formation of amorphous Ni clusters in HfO_2. These clusters could give rise to the observable ferromagnetism, independent of the matrix material, in which this cluster is embedded. Another explanation could be that Ni has been incorporated homogeneously into the hafnium oxide matrix, and that these Ni atoms do couple with oxygen vacancies leading to the observed ferromagnetic feature. However, this

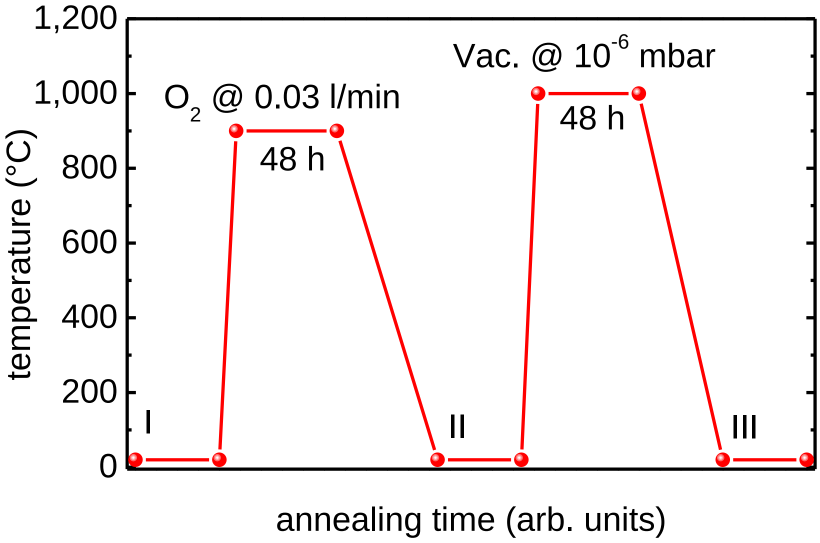

Fig. 6.4: Scheme for the post deposition heat treatment for a 50 nm thick HfO_2:8%Ni film, subsequent SQUID measurements were conducted after each annealing step, I to III.

explanation seems to be unlikely as strong rate fluctuations usually affect film homogeneity adversely.

In literature, examples for post deposition treatments of doped transition metal oxide films with Ni, Co, or Fe to influence the observed ferromagnetic feature can be found.[88, 89] When annealing in oxygen, the magnetic moment decreased as a function of annealing time, temperature, and oxidative character of the annealing atmosphere. Correspondingly, annealing under vacuum recovered the ferromagnetic moment. Similar experiments have been conducted to study the influence of post deposition annealing on the observed ferromagnetic feature. One out of two films exhibiting a ferromagnetic feature has been annealed first in a clean muffle furnace at 900 °C for 48 h under molecular oxygen flow. Molecular oxygen has been introduced to ensure proper film oxidation. After subsequent measurements with the MPMS, the same film has been annealed in vacuum for 48 h at 1000 °C. HV conditions (10^{-6} mbar) were established in a clean quartz tube furnace with integrated thermocouple for direct temperature measurement. Figure 6.4 illustrates the annealing procedure. After annealing under molecular oxygen flow, the ferromagnetic feature vanished, see Fig. 6.5 (a). In the case of existing amorphous Ni clusters, these clusters would have been oxidised to NiO, which itself is diamagnetic. Subsequent annealing under HV conditions leads to a slight recovery of the ferromagnetic feature. However, this feature was much smaller compared to the feature of the pristine sample (see Fig. 6.3). Further annealing in vacuum did not further recover the ferromagnetic feature. Either annealing under HV conditions does not provide sufficient reducing conditions, or diffusion processes during annealing destroy potential Ni clusters and enhance homogeneous Ni distribution in the HfO_2 matrix.

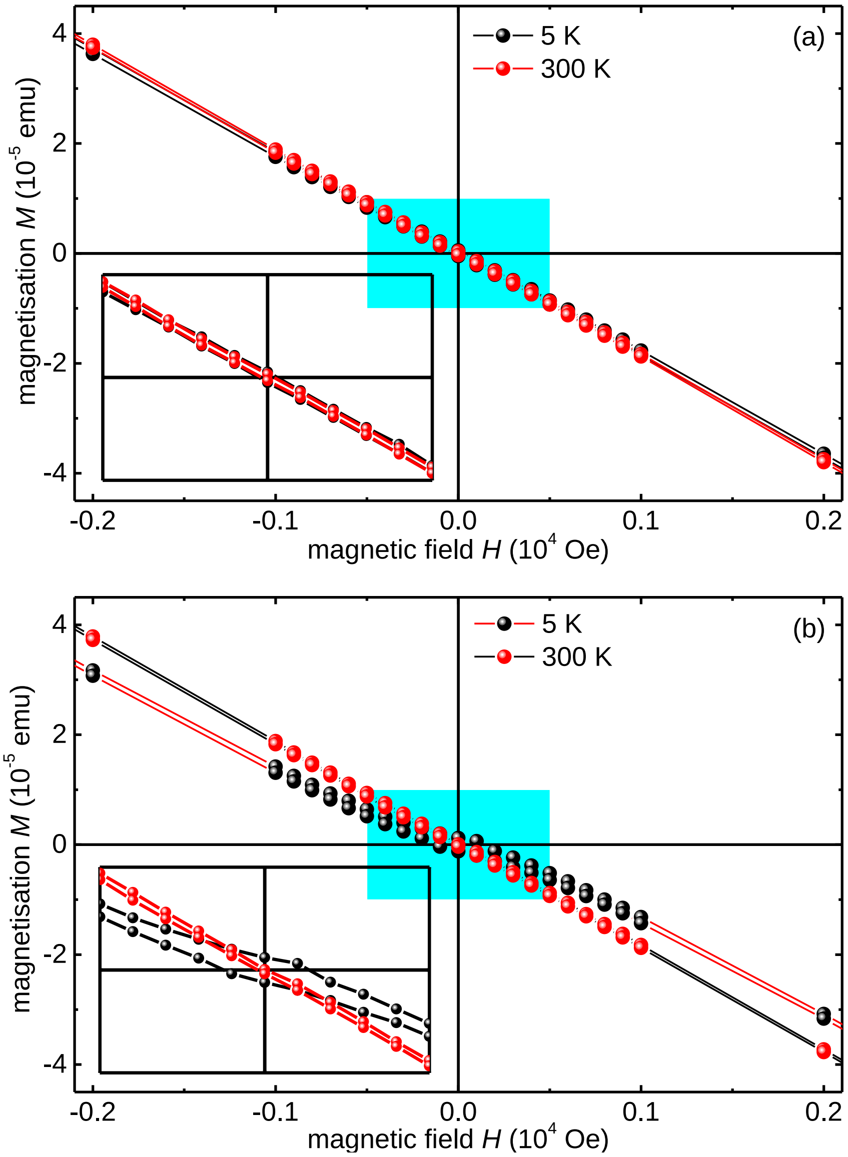

Fig. 6.5: Magnetisation data of a 50 nm thick HfO_2 film doped with 8 atom per cent Ni grown on *c*-cut sapphire substrate, (a) after annealing under molecular oxygen flow and (b) after subsequent annealing under vacuum conditions, insets show blow-ups of the shaded areas in (a) and (b).

6.4 Second series of Ni-doped $HfO_{2\pm x}$

As the observed Ni rate fluctuations bring uncertainty for the interpretation of how Ni is distributed in the hafnium oxide matrix, a second series of Ni-doped hafnia thin films utilising the stainless-steel screen has been grown. Substrate temperature was kept constant at 700 °C for all runs. For *in situ* oxidation, molecular and radical oxygen was used. Film thicknesses were in the range of 27 to 29 nm of Ni-doped HfO_2. Ni doping was varied from 4 atom per cent up to 60 atom per cent, resulting in Ni rates from 0.0084 Å/s (4 atom per cent) up to 0.126 Å/s (60 atom per cent) at 0.7 Å/s Hf rate. As the reported ferromagnetic moment in doped hafnium oxide thin films is attributed to (i) the doping level and (ii) the grade of oxygen deficiency, two studies have been conducted. First, the oxygen content was varied by varying the oxidation conditions during growth, second, the doping level was varied at given oxidation conditions.

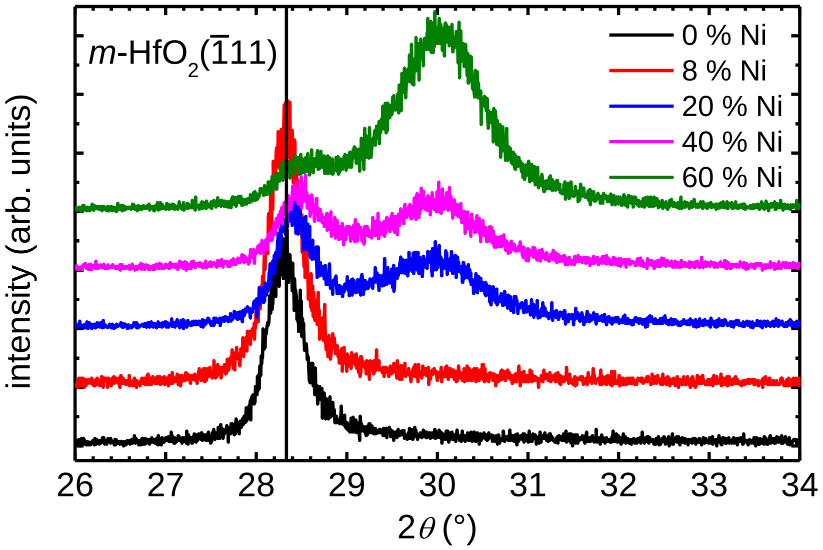

Fig. 6.6: Diffraction data of HfO_2 thin films grown on *c*-cut sapphire substrates under 1.5 sccm oxygen flow rate, 200 W of rf-power, 0.7 Å/s Hf rate, 700 °C substrate temperature, and varying Ni rate. The (-111) reflection of *m*-HfO_2 can be identified, which shifts to lower *d*-values with decreasing intensities as a function of increasing doping level. Another broad reflection at ~30° appears, whose intensity increases with increasing Ni doping rate.

In the case of molecular oxygen as oxidation agent, all grown films (film thickness around 27 nm Ni-doped HfO_2) stabilised in the monoclinic phase of hafnium oxide, (-111) oriented, regardless of the oxygen flow rate during growth (1.5 and 2.0 sccm), and regardless of the Ni doping level (4 and 40 atom per cent). None of the films showed a ferromagnetic hysteresis. In the case of radical oxygen, a series of different oxygen flow rates (1.0; 1.25; 1.5; 1.75; 2.0 sccm at 200 W rf-power) has been grown, each film doped with 4 atom per cent Ni, yielding to similar results in terms of crystal structure, film orientation, and magnetic properties. No room temperature ferromagnetism could be observed for HfO_2 thin films doped with 4 atom per cent Ni, regardless of the oxygen content.

Given an oxygen flow rate of 1.5 sccm, the influence of the Ni doping level has been studied in the range of 0 atom per cent (no doping, reference sample) up to 60 atom per cent Ni. Figure 6.6 displays X-ray diffraction data for HfO_2 thin films doped with various Ni concentrations, only a limited range in 2θ is shown for better clarity. This portion shows all reflections except for the (0006) substrate reflection of *c*-cut sapphire at $2\theta = 41.670°$. With increasing Ni doping level, the (-111) reflection of *m*-HfO_2 shifts towards higher 2θ–values while peak intensity decreases. The (-111) reflection of *m*-HfO_2 shifts from 28.335° for undoped HfO_2 to 28.521° for HfO_2 doped with 60 atom per cent Ni, corresponding to a shift in d of 0.020 Å. Additionally, a second broad reflection at $2\theta = 30.019°$ appears, its intensity increases with increasing doping level. This reflection cannot be assigned to *m*-HfO_2, Ni metal, NiO, and Ni_2O_3. However, *o*-HfO_2, *o*-Hf_3NiO, *c*-HfO_2, and *t*-HfO_2 do show reflections in this range, as evident from Fig. 6.7. As all films are transparent, it can be ruled out that the deposited Ni-doped HfO_2 films are of significant oxygen deficiency, thus the formation of *o*-Hf_3NiO with an oxidation state for Hf lower than +4 is very much unlikely. As no other film reflections could be observed than shown in Fig. 6.6, it is not possible to definitely assign the observed reflection to one of the mentioned crystalline phases of hafnia.

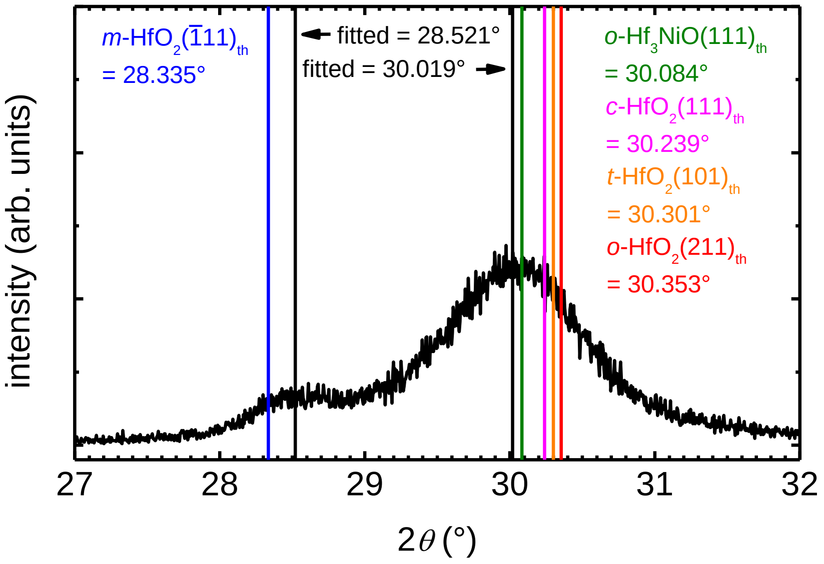

Fig. 6.7: Section of the 2θ–θ scan of a 30 nm thick HfO_2 thin film doped with 60 atom per cent Ni grown under 1.5 sccm oxygen flow rate, 200 W rf-power, and 700 °C substrate temperature. Both reflections have been fitted using a Gaussian peak profile (fit not shown). Reflections of potential candidates for peak indexing have been added.

It is remarkable that even for doping rates of 40 atom per cent Ni in HfO_2, the crystal structure of m-HfO_2 does not fully collapse. The shift of the (-111) reflection indicates that the dopant is incorporated in the crystal lattice rather than forming a separate, clustered phase. This result suggests homogeneous incorporation of Ni in HfO_2. Having homogeneous distribution of Ni in Ni-doped HfO_2 is crucial when it comes to the interpretation of the origin of room temperature ferromagnetism. The argumentation that the observed ferromagnetism is due to the formation of dopant clusters, thus of inhomogeneous distribution of the dopant in the crystal lattice, is not valid anymore. Besides homogeneity, it is important to get information on the absolute doping level, as it could be possible that the doping level approximated by the thickness ratio of the deposition rate controller after deposition is in reality higher or lower. It is known that for thin film growth in general, monitored thicknesses of the deposition rate controller usually differ with respect to real film thickness. Deposition of Ni-doped HfO_2 has been terminated (shutter closed) as soon as the thickness monitor of metal Hf has reached 20 nm getting an estimation on real doping level. As for all runs the Hf rate and the oxygen flow rate have been kept constant, a change in film thickness corresponds to a change in Ni content. Figure 6.8 displays film thickness (determined via XRR) as a function of the calculated Ni doping level. The higher the Ni doping is, the higher the resulting film thickness.

Up to 20 atom per cent of Ni, a linear increase with increasing doping level is observed. For doping levels of 40 and 60 atom per cent, the linear trend vanishes. This could be attributed to source drift as a function of time. Considering that Ni gets incorporated in the m-HfO_2 matrix and comparable ionic radii of 8-fold coordinated Hf^{4+} and 6-fold coordinated Ni^{2+} of 83 and 70 pm, respectively, a doping level of 20% Ni in HfO_2 should lead to an increase in film thickness of about 20%. As evident from Fig. 6.8, the HfO_2 film doped with 20 atom per cent Ni is only 9% thicker than a bare HfO_2 film grown with similar deposition time. Based on this result, the real doping level is estimated to be 50% lower than what extracted from the rate thickness controller.

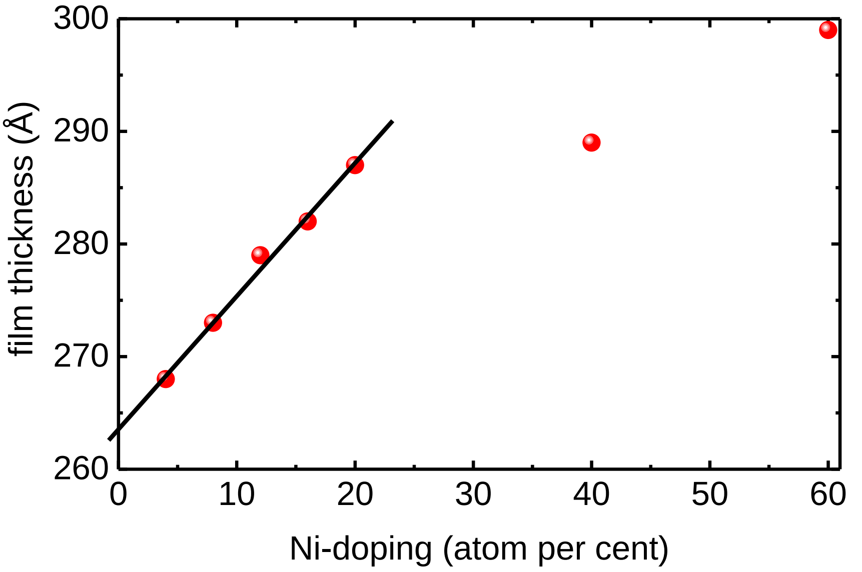

Fig. 6.8: Film thickness as a function of Ni doping level.

SIMS depth profiles on Ni-doped HfO_2 thin films have been carried out in collaboration with Dr. Flege, Institute of Materials Science, TU Darmstadt, to (i) check incorporation of Ni in hafnia thin films, and (ii) to verify the homogeneous distribution of Ni in HfO_2. Figure 6.9 shows a depth profile of a 27 nm thick HfO_2:8%Ni thin film monitoring the corresponding masses of oxygen, hafnium, aluminium, and nickel. Sample surface was subjected to continuous ion bombardment, which leads to a mixing of the first atomic layers, obtaining depth profiles. The mixing effect limits depth resolution, thus the accuracy in determining the film/substrate interface. Surface mixing leads to a steadily increasing Al signal, whereas the Hf signal decreases at the same time. This effect has been observed earlier for pure HfO_2 thin films, as the Hf signal decreased very slowly with increasing sputtering time. Another reason for the slow decrease of the Hf signal as a function of sputtering time could be sputtering of the sputter crater sides. This effect could explain the slow decrease of the Ni signal with similar slope as the Hf signal for sputtering times longer than ~3,500 seconds. The Ni signal shows a fluctuation in intensity vs. sputtering time, which could be an indication for inhomogeneity of Ni content as a function of film thickness. However, the variation of the Ni signal is considered to be originated by the sputtering process, rather than resulting from inhomogeneous Ni depth distribution. As deposition rates during film growth have been extremely stable, it is unlikely that significant concentration gradients occur in a 27 nm thick film.

SIMS is a versatile tool for qualitative information on sample composition, but lacks of possibilities for quantification without available standards. The preparation of Ni-doped HfO_2 thin film standards, which could be investigated by RBS for quantifying the Ni content, has not yet been conducted. Having at least two RBS calibrated standards would allow calibrating obtained SIMS data and thus transforming relative intensities to absolute concentrations, considering that matrix contributions do not change significantly as a function of Ni-doping. For all Ni-doped HfO_2 thin films, magnetisation measurements have been conducted at 300 and 5 K to check for ferromagnetic features. None of the films, regardless of the doping level exhibited ferromagnetic features. All films showed linear, diamagnetic behaviour, as observed for undoped HfO_2. Considering that the real doping level is about 50% lower than the doping level extracted from the rate thickness controller, a doping level of 60% Ni yields to a real

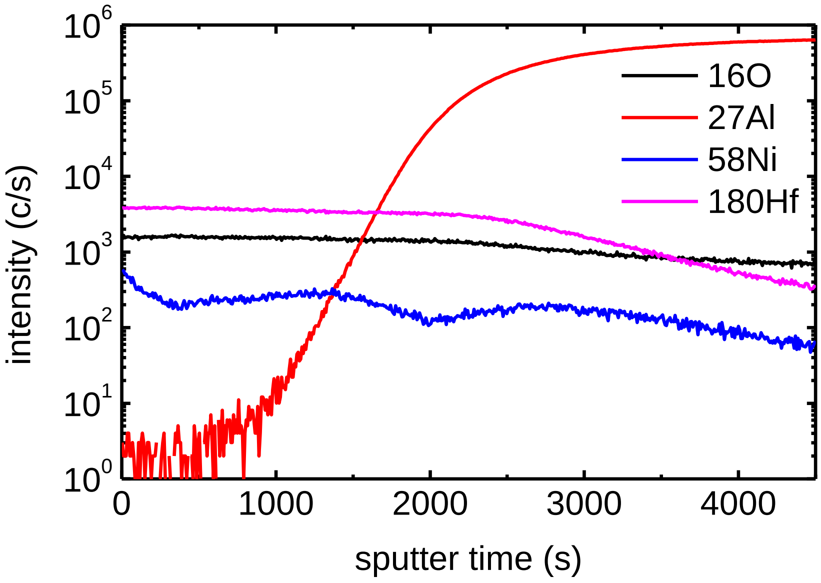

Fig. 6.9: SIMS studies of a 27 nm thick HfO_2 thin film doped with 8 atom per cent Ni.

doping level in the range of ∼30%. Even films with such high doping concentrations did not show any ferromagnetic feature in SQUID. This result supports the assumption of homogeneous distribution of Ni in the HfO_2 matrix, as the distance of Ni atoms is too big for ferromagnetic coupling. The formation of Ni clusters during deposition can be ruled out, as they would certainly contribute to a ferromagnetic signal.

Summarising the Ni-doping studies it is evident that for Ni doping experiments without rate fluctuations the formation of Ni clusters in the films can be ruled out, as even extreme high doping rates of more than 40 atom per cent Ni in HfO_2 did not show any ferromagnetic feature. The formation of crystalline NiO is also ruled out, as no evidence for NiO has been found during X-ray studies. The observed shift in d for increasing Ni doping could be due to the incorporation of Ni into the crystal structure of hafnia; however, doping rates of 40 atom per cent did not show any ferromagnetic feature. From the annealing experiments conducted for the film showing a ferromagnetic hysteresis (grown with rate fluctuations) it is evident that the ferromagnetic moment vanishes when annealing under oxygen, but does not recover when annealing under vacuum. The phenomenon of high-T_c ferromagnetism seems to be more complex and further studies are necessary to unravel how the reported ferromagnetism can be explained.

7 Summary and outlook

The following two sections give a brief summary of the scientific results of the growth and characterisation of hafnium oxide thin films grown by RMBE, and provide a short prospective of what kind of studies can be done in future. It is worth to mention that thin film growth by RMBE involves extensive technical efforts, as state-of-the-art RMBE units are unfortunately not commercially available, so custom-design and fabrication has to go hand in hand with science. During the preparation of this thesis, significant contributions have been made to design and set up an entirely new advanced oxide MBE (ADOMBE) unit integrated into a UHV-based deposition cluster system.

7.1 HfO_2 thin films

- Thin films of hafnium oxide have been grown on various substrates by RMBE, based on e-beam evaporation of metal Hf and oxidation via oxygen radicals.
- The influence of substrate temperature, oxygen flow rate supplied to the radical source, and rf-power applied to the radical source on film quality in terms of crystallinity and orientation has been investigated.
- For optimal growth parameters (0.7 Å/s Hf rate, 1.5 sccm oxygen flow rate, 200 W rf-power, and 700 °C substrate temperature), single (-111)-oriented films of monoclinic HfO_2 could be grown in a reproducible way on *c*-cut sapphire.
- Films exhibited surface roughness's of 0.22 nm RMS in a measured area of 1 μm^2 measured by AFM and showed clear X-ray intensity oscillations in XRR for film thicknesses up to 200 nm.
- Under reduced growth rates, films grow epitaxially on *c*-cut sapphire, the epitaxial relations for (-111)-oriented films are m-HfO_2(-111)||Al_2O_3(0006) for out-of-plane and m-HfO_2[220]||Al_2O_3[1-100] for in-plane.
- The corresponding rocking curve of the (-111) reflection yielded to a FWHM of 0.08°.
- RHEED oscillations have been observed for (-111) oriented films.
- Hafnium oxide thin films above 15 nm thickness grow strain-free (relaxed) on *c*-cut sapphire, but stay highly textured.
- Annealing experiments of deposited hafnia films on *c*-cut sapphire under oxygen at 1,000 °C did not improve crystal quality.
- Stoichiometric thin films of hafnia were transparent, exhibited a band gap of 5.7 eV, and showed diamagnetic behaviour.

7.2 $HfO_{2\pm x}$ thin films

- Oxygen defects have been introduced into the films *in situ* during growth by varying oxygen flow rate and the rf-power.
- $HfO_{2\pm x}$ film orientation changed as a function of oxidation conditions from pure (-111) orientation to single (002)-oriented films.
- Regardless of how far the oxidation conditions were varied, hafnia stabilised in its monoclinic structure.

- Films mixed of hafnium oxide and metal hafnium were obtained only for molecular oxygen as oxidation agent at very low flow rates (< 0.2 sccm).
- As a function of deficiency, film colour changed from transparent and colourless (HfO_2) to dark and opaque (HfO_{2-x}).
- Film luminescence was evoked for deficient films of hafnia that scaled with oxidation conditions, the lower the oxygen content is, the stronger the observed photoluminescence.
- The optical band gap has been investigated as a function of deficiency resulting in a parabolic behaviour of E_g vs. oxidation conditions spanning more than 1 eV in E_g.
- Electrical characterisation revealed resistivities in the range of 300 $\mu\Omega$cm for films grown under very low oxidation conditions.
- Resistivity could be reproducibly tuned within five orders of magnitude by changing the amount of oxygen vacancies.
- Temperature dependent ρ-T measurements show metallic behaviour for highly reduced samples.
- Hall measurements show no anomalous Hall effect and reveal p-type conductivity with charge carrier concentrations of 6 x 10^{21} cm^{-3} and mobilities of 2 $cm^2/(Vs)$.
- The observed conductivity is neither due to crystalline nor due to amorphous hafnium as evident from X-ray and HRTEM studies
- No evidence for d^0-ferromagnetism in contamination-free thin films was found, regardless of the oxygen content.
- A simplified defect band structure model has been developed for oxygen deficient HfO_{2-x} accounting for the observed p-type conductivity and the change in transparency.

7.3 Ni-doped hafnia

- Hafnium oxide thin films have been *in situ* doped at atomic concentrations of a few per cent by e-beam evaporation in a highly reproducible manner utilising a screen.
- With increasing dopant concentration, the (-111) reflection of hafnia shifts by 0.020 Å to lower d-values, which could be explained by the incorporation of Ni into the crystal structure of hafnia.
- SIMS studies confirm the incorporation of nickel into the films; XRR studies as a function of dopant concentration underline these results.
- Only two films grown with rate fluctuations exhibited a ferromagnetic feature with a Curie temperature above 350 K.
- Annealing experiments of these two films yielded to vanishing high-T_c ferromagnetism, whereas annealing under vacuum conditions did not fully retrieve the ferromagnetism.
- All other films showed diamagnetic behaviour up to doping concentrations of 60 atom per cent, regardless of oxidation conditions.
- The formation of Ni clusters in the grown films can be ruled out.
- The formation of crystalline NiO can be ruled out.

From a broader perspective, this study demonstrates the capabilities of RMBE when it comes to the growth of oxide thin films with defined oxygen deficiency. As nowadays the role of oxygen content and oxygen vacancies becomes more and more important for the explanation of physical phenomena, RMBE is the right answer allowing precise controlling of oxygen stoichiometry. In contrast to strontium titanate thin films, in which oxygen content can be varied by comparably simple post deposition annealing techniques, this is obviously not possible for hafnium oxide. Additionally, in strontium titanate and in titanium oxide there are stable crystalline phases with oxidation states of Sr and Ti lower than 2+ and 4+, respectively, which seems not to be the case for hafnium oxide. From these aspects, RMBE, as a versatile growth technique for *in situ* introducing oxygen vacancies and allowing the stabilisation of films in metastable states far away from thermodynamic equilibrium, is the deposition method of choice for the growth of oxygen deficient hafnia thin films.

7.4 Future prospects

This section gives a brief overview on possible research topics based on the results of this study.

- Nowadays oxygen vacancies have to be introduced by a formation step in memristive devices based on hafnia. The introduction of oxygen vacancies could be achieved *in situ* by RMBE during growth, possibly making the formation step unnecessary.
- RMBE-grown films of HfO_{2-x} could help to further investigate the origin of the switching effect, as the dependence of resistive switching as a function of the overall defect concentration could be investigated in more detail.
- The role of Ti electrodes in such devices could be investigated, as no electrodes with high oxide formation energies to create oxygen deficiency in hafnia might be necessary.
- The discovery of *p*-type conductivity in oxygen deficient hafnia could be of high importance for semiconductor industry, as having an insulator (dielectric) and a conductor (electrode) made of one material allows the fabrication of functional devices made of one single material.
- Transferring the results of this study to other oxide thin film systems, such as TiO_2 or ZrO_2, could lead to the discovery of similar effects as a function of oxygen content (e.g., electrical conductivity, optical band gap).
- To complete the studies on the origin of high-T_c ferromagnetism in transition metal oxides, XMCD studies were already carried out but have to be evaluated carefully.

List of figures

List of Tables

References

[1] K. Ploog and A. Fischer, Appl. Phys. **13**, 111 (1977).

[2] K. Ploog, A. Fischer, R. Trommer, and M. Hirose, J. Vac. Sci. Technol. **16**, 290 (1979).

[3] R. A. Stall, J. Vac. Sci. Technol. B **1**, 135 (1983).

[4] T. J. Maloney, J. Vac. Sci. Technol. B **1**, 773 (1983).

[5] R. A. Betts and C. W. Pitt, Electron. Lett. **21**, 960 (1985).

[6] S. Hosokawa and S. Ichimura, Rev. Sci. Instrum. **62**, 1614 (1991).

[7] K. Iwata, P. Fons, S. Niki, A. Yamada, K. Matsubara, K. Nakahara, T. Tanabe, and H. Takasu, J. Cryst. Growth **214**, 50 (2000).

[8] Varian Vacuum Products, Lexington, MA.

[9] C. D. Theis and D. G. Schlom, J. Vac. Sci. Technol. A **14**, 2677 (1996).

[10] K. Horiba, H. Ohguchi, H. Kumigashira, M. Oshima, K. Ono, N. Nakagawa, M. Lippmaa, M. Kawasaki, and H. Koinuma, Rev. Sci. Instrum. **74**, 3406 (2003).

[11] H. Koinuma and I. Takeuchi, Nat. Mater. **3**, 429 (2004).

[12] A. Tsukazaki, A. Ohtomo, T. Kita, Y. Ohno, H. Ohno, and M. Kawasaki, Science **315**, 1388 (2007).

[13] L. Pfeiffer and K. W. West, Physica E **20**, 57 (2003).

[14] D. A. Muller, N. Nakagawa, A. Ohtomo, J. L. Grazul, and H. Y. Hwang, Nature **430**, 657 (2004).

[15] C. L. Jia and K. Urban, Science **303**, 2001 (2004).

[16] D. G. Schlom, J. H. Haeni, J. Lettieri, C. D. Theis, W. Tian, J. C. Jiang, and X. Q. Pan, Mater. Sci. Eng. B **87**, 282 (2001).

[17] J. H. Haeni, C. D. Theis, and D. G. Schlom, J. Electroceram. **4**, 385 (2000).

[18] Y. Horikoshi, M. Kawashima, and H. Yamaguchi, Jpn. J. Appl. Phys., Part 1 **27**, 169 (1988).

[19] G. Logvenov, A. Gozar, and I. Bozovic, Science **326**, 699 (2009).

[20] J. H. Haeni, C. D. Theis, D. G. Schlom, W. Tian, X. Q. Pan, H. Chang, I. Takeuchi, and X. D. Xiang, Appl. Phys. Lett. **78**, 3292 (2001).

[21] K. Iijima, T. Terashima, Y. Bando, K. Kamigaki, and H. Terauchi, J. Appl. Phys. **72**, 2840 (1992).

[22] H. L. Cai, X. S. Wu, and J. Gao, Chem. Phys. Lett. **467**, 313 (2009).

[23] R. Ramesh and N. A. Spaldin, Nat. Mater. **6**, 21 (2007).

[24] R. A. McKee, F. J. Walker, and M. F. Chisholm, Phys. Rev. Lett. **81**, 3014 (1998).

[25] J. Son, P. Moetakef, B. Jalan, O. Bierwagen, N. J. Wright, R. Engel-Herbert, and S. Stemmer, Nat. Mater. **9**, 482 (2010).

[26] B. Jalan, R. Engel-Herbert, N. J. Wright, and S. Stemmer, J. Vac. Sci. Technol. A **27**, 461 (2009).

[27] Y. Kozuka, M. Kim, C. Bell, B. G. Kim, Y. Hikita, and H. Y. Hwang, Nature **462**, 487 (2009).

[28] S. Karimoto and M. Naito, Physica C **412**, 1349 (2004).

[29] M. Naito, S. Karimoto, and A. Tsukada, Supercond. Sci. Technol. **15**, 1663 (2002).

[30] M. E. Jones and R. E. Marsh, J. Am. Chem. Soc. **76**, 1434 (1954).

[31] J. Nagamatsu, N. Nakagawa, T. Muranaka, Y. Zenitani, and J. Akimitsu, Nature **410**, 63 (2001).

[32] M. Balog, M. Schieber, M. Michman, and S. Patai, J. Cryst. Growth **17**, 298 (1972).

[33] M. Balog, M. Schieber, M. Michman, and S. Patai, Thin Solid Films **41**, 247 (1977).

[34] E. Ryshkewitch and D. W. Richerson, *Oxide ceramics: Physical chemistry and technology* (Academic, Florida, 1985).

[35] J. Wang, H. P. Li, and R. Stevens, J. Mater. Sci. **27**, 5397 (1992).

[36] M. C. Cheynet, S. Pokrant, F. D. Tichelaar, and J. L. Rouviere, J. Appl. Phys. **101**, 054101 (2007).

37 F. L. Martinez, M. Toledano-Luque, J. J. Gandia, J. Carabe, W. Bohne, J. Rohrich, E. Strub, and I. Martil, J. Phys. D: Appl. Phys. **40**, 5256 (2007).

38 C. J. Howard, R. J. Hill, and B. E. Reichert, Acta Crystallogr., Sect. B: Struct. Sci. **44**, 116 (1988).

39 R. Ruh and P. W. Corfield, J. Am. Ceram. Soc. **53**, 126 (1970).

40 F. A. Cotton, *Advanced inorganic chemistry* (Wiley, New York [u.a.], 1999).

41 J. E. Jaffe, R. A. Bachorz, and M. Gutowski, Phys. Rev. B **72**, 144107 (2005).

42 A. J. Waldorf, J. A. Dobrowolski, B. T. Sullivan, and L. M. Plante, Appl. Opt. **32**, 5583 (1993).

43 J. E. Lowther, J. K. Dewhurst, J. M. Leger, and J. Haines, Phys. Rev. B **60**, 14485 (1999).

44 T. V. Perevalov, V. A. Gritsenko, S. B. Erenburg, A. M. Badalyan, H. Wong, and C. W. Kim, J. Appl. Phys. **101**, 053704 (2007).

45 A. Jayaraman, S. Y. Wang, S. K. Sharma, and L. C. Ming, Phys. Rev. B **48**, 9205 (1993).

46 L. G. Liu, J. Phys. Chem. Solids **41**, 331 (1980).

47 R. Puthenkovilakam and J. P. Chang, J. Appl. Phys. **96**, 2701 (2004).

48 K. Momma and F. Izumi, J. Appl. Crystallogr. **44**, 1272 (2011).

49 Y. Ohshita, A. Ogura, A. Hoshino, S. Hiiro, and H. Machida, J. Cryst. Growth **233**, 292 (2001).

50 T. Mori, M. Fujiwara, R. R. Manory, I. Shimizu, T. Tanaka, and S. Miyake, Surf. Coat. Technol. **169**, 528 (2003).

51 T.-H. Moon and J.-M. Myoung, Appl. Surf. Sci. **240**, 197 (2005).

52 T. Nishide, S. Honda, M. Matsuura, and M. Ide, Thin Solid Films **371**, 61 (2000).

53 M. Villanueva-Ibanez, C. Le Luyer, O. Marty, and J. Mugnier, Opt. Mater. **24**, 51 (2003).

54 M. G. Blanchin, B. Canut, Y. Lambert, V. S. Teodorescu, A. Barau, and M. Zaharescu, J. Sol-Gel Sci. Technol. **47**, 165 (2008).

55 Y. Aoki, T. Kunitake, and A. Nakao, Chem. Mat. **17**, 450 (2005).

56 J. D. Wright and N. A. J. M. Sommerdijk, *Sol-gel materials : chemistry and applications* (CRC Press, Boca Raton [u.a.], 2001).

57 Z. J. Wang, T. Kumagai, H. Kokawa, J. Tsuaur, M. Ichiki, and R. Maeda, J. Cryst. Growth **281**, 452 (2005).

58 C. T. Kuo, R. Kwor, and K. M. Jones, Thin Solid Films **213**, 257 (1992).

59 G. He, M. Liu, L. Q. Zhu, M. Chang, Q. Fang, and L. D. Zhang, Surf. Sci. **576**, 67 (2005).

60 L. Pereira, P. Barquinha, E. Fortunato, and R. Martins, Mater. Sci. Eng. B **118**, 210 (2005).

61 R. K. Nahar and A. Sharma, Microelectron. Int. **24**, 46 (2007).

62 M. A. Sahiner, J. C. Woicik, P. Gao, P. McKeown, M. C. Croft, M. Gartman, and B. Benapfla, Thin Solid Films **515**, 6548 (2007).

63 H. Hu, C. X. Zhu, Y. F. Lu, Y. H. Wu, T. Liew, M. F. Li, B. J. Cho, W. K. Choi, and N. Yakovlev, J. Appl. Phys. **94**, 551 (2003).

64 H. Wang, et al., Appl. Phys. A: Mater. Sci. Process. **93**, 681 (2008).

65 H. Wang, Y. Wang, J. Zhang, C. Ye, H. B. Wang, J. Feng, B. Y. Wang, Q. Li, and Y. Jiang, Appl. Phys. Lett. **93**, 202904 (2008).

66 X. Q. Zhang, H. L. Tu, X. N. Wang, Y. H. Xiong, M. M. Yang, L. Wang, and J. Du, J. Cryst. Growth **312**, 2928 (2010).

67 S. Van Elshocht, et al., J. Electrochem. Soc. **151**, F228 (2004).

68 S. Hino, M. Nakayama, K. Takahashi, H. Funakubo, and E. Tokumitsu, Jpn. J. Appl. Phys., Part 1 **42**, 6015 (2003).

69 S. Nafis, J. Owyang, and S. Chatterji, Solid State Technol. **49**, 37 (2006).

70 K. Mistry, et al., IEEE Int. Elec. Dev. Meet., 247 (2007).

[71] http://www.cambridgenanotech.com/.
[72] J. Niinisto, K. Kukli, M. Heikkila, M. Ritala, and M. Leskela, Adv. Eng. Mater. **11**, 223 (2009).
[73] J. H. Choi, Y. Mao, and J. P. Chang, Mater. Sci. Eng. R **72**, 97 (2011).
[74] Z. J. Yan, R. Xu, Y. Y. Wang, S. Chen, Y. L. Fan, and Z. M. Jiang, Appl. Phys. Lett. **85**, 85 (2004).
[75] W. C. Lee, et al., J. Cryst. Growth **278**, 619 (2005).
[76] J. P. Lehan, Y. Mao, B. G. Bovard, and H. A. Macleod, Thin Solid Films **203**, 227 (1991).
[77] M. Venkatesan, C. B. Fitzgerald, and J. M. D. Coey, Nature **430**, 630 (2004).
[78] T. Fukumura, Y. Yamada, H. Toyosaki, T. Hasegawa, H. Koinuma, and M. Kawasaki, Appl. Surf. Sci. **223**, 62 (2004).
[79] J. M. D. Coey, M. Venkatesan, and C. B. Fitzgerald, Nat. Mater. **4**, 173 (2005).
[80] K. Potzger, et al., J. Magn. Magn. Mater. **323**, 1551 (2011).
[81] J. B. Goodenough, *Magnetism and the chemical bond* (Krieger, Huntington, N.Y, 1976).
[82] J. M. D. Coey, M. Venkatesan, P. Stamenov, C. B. Fitzgerald, and L. S. Dorneles, Phys. Rev. B **72**, 024450 (2005).
[83] W. D. Wang, Y. J. Hong, M. H. Yu, B. Rout, G. A. Glass, and J. K. Tang, J. Appl. Phys. **99**, 08m117 (2006).
[84] D. W. Abraham, M. M. Frank, and S. Guha, Appl. Phys. Lett. **87**, 252502 (2005).
[85] M. S. Ramachandra Rao, et al., Appl. Phys. Lett. **88**, 142505 (2006).
[86] S. B. Ogale, et al., Phys. Rev. Lett. **91**, 077205 (2003).
[87] W. Prellier, A. Fouchet, and B. Mercey, J. Phys. Condens. Matter **15**, R1583 (2003).
[88] N. H. Hong, J. Sakai, N. Poirot, and A. Ruyter, Appl. Phys. Lett. **86**, 242505 (2005).
[89] N. H. Hong, N. Poirot, and J. Sakai, Appl. Phys. Lett. **89**, 042503 (2006).
[90] Y. L. Soo, et al., Phys. Rev. B **76**, 132404 (2007).
[91] M. K. Sharma, A. Kanjilal, M. Voelskow, D. Kanjilal, and R. Chatterjee, Nucl. Instrum. Methods Phys. Res., Sect. B **268**, 1631 (2010).
[92] Y. Yamada, et al., Science **332**, 1065 (2011).
[93] X. Y. Qiu, Q. M. Liu, F. Gao, L. Y. Lu, and J. M. Liu, Appl. Phys. Lett. **89**, 242504 (2006).
[94] R. Waser and M. Aono, Nat. Mater. **6**, 833 (2007).
[95] Z. R. Wang, H. Y. Yu, X. A. Tran, Z. Fang, J. H. Wang, and H. B. Su, Phys. Rev. B **85**, 195322 (2012).
[96] D. H. Kwon, et al., Nat. Nanotechnol. **5**, 148 (2010).
[97] R. Waser, R. Dittmann, G. Staikov, and K. Szot, Adv. Mater. **21**, 2632 (2009).
[98] C. Walczyk, et al., J. Appl. Phys. **105**, 114103 (2009).
[99] C. Walczyk, et al., IEEE Trans. Electron Devices **58**, 3124 (2011).
[100] H. Y. Lee, et al., IEEE Int. Elec. Dev. Meet.: Tec. Dig., 4 (2008).
[101] L. Goux, et al., Appl. Phys. Lett. **97**, 243509 (2010).
[102] T. Bertaud, et al., Thin Solid Films **520**, 4551 (2012).
[103] J. J. Yang, M. D. Pickett, X. M. Li, D. A. A. Ohlberg, D. R. Stewart, and R. S. Williams, Nat. Nanotechnol. **3**, 429 (2008).
[104] M. Houssa, G. Pourtois, M. M. Heyns, and A. Stesmans, J. Phys. Condens. Matter **17**, S2075 (2005).
[105] K. Xiong, J. Robertson, M. C. Gibson, and S. J. Clark, Appl. Phys. Lett. **87**, 183505 (2005).
[106] D. Munoz Ramo, J. L. Gavartin, A. L. Shluger, and G. Bersuker, Phys. Rev. B **75**, 205336 (2007).
[107] D. Munoz Ramo, A. L. Shluger, J. L. Gavartin, and G. Bersuker, Phys. Rev. Lett. **99**, 155504 (2007).
[108] P. Broqvist and A. Pasquarello, Appl. Phys. Lett. **89**, 262904 (2006).
[109] J. Ni, Q. Zhou, Z. C. Li, and Z. J. Zhang, Appl. Phys. Lett. **93**, 011905 (2008).

110 A. S. Foster, F. L. Gejo, A. L. Shluger, and R. M. Nieminen, Phys. Rev. B **65**, 174117 (2002).

111 J. Robertson, O. Sharia, and A. A. Demkov, Appl. Phys. Lett. **91**, 132912 (2007).

112 H. M. Weng and J. M. Dong, Phys. Rev. B **73**, 132410 (2006).

113 C. Das Pemmaraju and S. Sanvito, Phys. Rev. Lett. **94**, 217205 (2005).

114 X. Han, J. Lee, and H.-I. Yoo, Phys. Rev. B **79**, 100403 (2009).

115 D. Misra, H. Iwai, and H. Wong, Electrochem. Soc. Interface **14**, 30 (2005).

116 G. E. Moore, Proc. IEEE **86**, 82 (1998).

117 A. Kawamoto, K. J. Cho, and R. Dutton, J. Comput.-Aided Mater. Des. **8**, 39 (2001).

118 S. O. Kasap, *Principles of electronic materials and devices* (McGraw-Hill, Boston, 2006).

119 G. D. Wilk, R. M. Wallace, and J. M. Anthony, J. Appl. Phys. **89**, 5243 (2001).

120 G. Dutta, Appl. Phys. Lett. **94**, 012907 (2009).

121 D. Fischer and A. Kersch, J. Appl. Phys. **104**, 084104 (2008).

122 H. Kim, P. C. McIntyre, and K. C. Saraswat, Appl. Phys. Lett. **82**, 106 (2003).

123 M. M. Frank, 41st Europ. Solid State Dev. Res. Conf., 25 (2011).

124 C. Nanotechnology, 2010), Vol. 2012.

125 M. A. Herman, W. Richter, and H. Sitter, *Epitaxy: physical principles and technical implementation* (Springer, Berlin [u.a.], 2004).

126 M. A. Herman and H. Sitter, *Molecular beam epitaxy: fundamentals and current status* (Springer, Berlin [u.a.], 1996).

127 M. Ohring, *Materials science of thin films: deposition and structure* (Academic Press, London [u.a.], 2002).

128 J. Venables, *Introduction to surface and thin film processes* (Cambridge Univ. Press, Cambridge, 2001).

129 S. A. Chambers, Surf. Sci. Rep. **39**, 105 (2000).

130 I. Bozovic, G. Logvenov, I. Belca, B. Narimbetov, and I. Sveklo, Phys. Rev. Lett. **89**, 107001 (2002).

131 X. M. Li, M. Kanai, T. Kawai, and S. Kawai, Jpn. J. Appl. Phys., Part 2 **31**, L217 (1992).

132 Y. Terashima, R. Sato, S. Takeno, S. Nakamura, and T. Miura, Jpn. J. Appl. Phys., Part 2 **32**, L48 (1993).

133 I. Bozovic, IEEE Trans. Appl. Supercon. **11**, 2686 (2001).

134 I. Bozovic, G. Logvenov, M. A. J. Verhoeven, P. Caputo, E. Goldobin, and T. H. Geballe, Nature **422**, 873 (2003).

135 R. Triboulet and J. Perriere, Prog. Cryst. Growth Charact. Mater. **47**, 65 (2003).

136 P. Chang, W. C. Lee, T. D. Lin, C. H. Hsu, J. Kwo, and M. Hong, J. Cryst. Growth **323**, 511 (2011).

137 B. J. Gibbons, M. E. Hawley, S. Trolier-McKinstry, and D. G. Schlom, J. Vac. Sci. Technol. A **19**, 584 (2001).

138 K. L. Chopra, *Thin film phenomena* (Krieger, New York, 1979).

139 R. F. C. Farrow, *Molecular beam epitaxy: applications to key materials* (Noyes Publ., Park Ridge, NJ, 1995).

140 R. Riedel, *Ceramics science and technology* (Wiley-VCH, Weinheim, 2011).

141 H. Okamoto, J. Phase Equilib. Diffus. **26**, 648 (2005).

142 Y. Yamada, T. Harada, H. Uyama, T. Murata, and H. Nozoye, Thin Solid Films **377**, 92 (2000).

143 M. Nagamine, H. Itoh, H. Satake, and A. Toriumi, Int. Elec. Dev., 593 (1998).

144 Y. Tazoh and S. Miyazawa, Appl. Phys. Lett. **62**, 408 (1993).

145 J. E. Pollard, Rev. Sci. Instrum. **63**, 1771 (1992).

146 L. S. Yujahnes, W. T. Brogan, A. C. Anderson, and M. J. Cima, Rev. Sci. Instrum. **63**, 4149 (1992).

147 K. Dittmann, D. Drozdov, B. Krames, and J. Meichsner, J. Phys. D-Appl. Phys. **40**, 6593 (2007).

148 C. Buzea and K. Robbie, Rep. Prog. Phys. **68**, 385 (2005).

149 C.-s. Lu, J. Vac. Sci. Technol. **12**, 578 (1975).

150 C. D. Theis, J. Yeh, D. G. Schlom, M. E. Hawley, G. W. Brown, J. C. Jiang, and X. Q. Pan, Appl. Phys. Lett. **72**, 2817 (1998).

151 A. Ichimiya and P. I. Cohen, *Reflection high-energy electron diffraction* (Cambridge Univ. Press, Cambridge [u.a.], 2004).

152 W. Braun, *Applied rheed: reflection high energy electron diffraction during crystal growth* (Springer, Berlin [u.a.], 1999).

153 W. Borchardt-Ott, *Crystallography* (Springer, Berlin [u.a.], 1995).

154 B. D. Cullity and S. R. Stock, *Elements of X-ray diffraction* (Pearson/Prentice Hall, Upper Saddle River, NJ [u.a.], 2001).

155 M. De Graef and M. E. McHenry, *Structure of materials: an introduction to crystallography, diffraction, and symmetry* (Cambridge University Press, Cambridge [u.a.], 2010).

156 T. Hahn, U. Shmueli, A. J. C. Wilson, and International Union of Crystallography., *International tables for crystallography* (D. Reidel Pub. Co.; Sold and distributed in the U.S.A. and Canada by Kluwer Academic Publishers Group, Dordrecht, Holland; Boston, U.S.A., Hingham, MA, 1984).

157 A. R. Verma and O. N. Srivastava, *Crystallography for solid state physics* (Wiley, New York, 1982).

158 J. Wang, G. Li, P. Yang, M. Q. Cui, X. M. Jiang, B. Dong, and H. Liu, Europhys. Lett. **42**, 283 (1998).

159 C. Rincon and G. Sanchez Perez, Prog. Cryst. Growth Charact. **10**, 307 (1984).

160 A. K. S. Aqili and A. Maqsood, Appl. Opt. **41**, 218 (2002).

161 D. Meschede and C. Gerthsen, *Gerthsen Physik* (Springer, Heidelberg [u.a.], 2010).

162 P. A. Tipler and G. Mosca, *Physics for scientists and engineers: with modern physics* (W.H. Freeman, New York, NY, 2008).

163 J. W. Ekin, *Experimental techniques for low-temperature measurements: cryostat design, material properties, and superconductor critical-current testing* (Univ. Pr., Oxford [u.a.], 2007).

164 L. J. van der Pauw, Philips Res. Repts. **13**, 1 (1958).

165 L. J. van der Pauw, Philips Tech. Rev. **26**, 220 (1958).

166 D. C. Look, *Electrical characterization of GaAs materials and devices* (Wiley, Chichester, New York, 1989).

167 O. Bierwagen, T. Ive, C. G. Van de Walle, and J. S. Speck, Appl. Phys. Lett. **93**, 242108 (2008).

168 A. Benninghoven, F. G. Rüdenauer, and H. W. Werner, *Secondary ion mass spectrometry: basic concepts, instrumental aspects, applications, and trends* (J. Wiley, New York, 1987).

169 E. d. Hoffmann and V. Stroobant, *Mass spectrometry : principles and applications* (J. Wiley, Chichester, West Sussex, England; Hoboken, NJ, 2007).

170 J. C. Vickerman, A. A. Brown, and N. M. Reed, *Secondary ion mass spectrometry: principles and applications* (Clarendon Press; Oxford University Press, Oxford; New York, 1989).

171 K. M. Lang, D. A. Hite, R. W. Simmonds, R. McDermott, D. P. Pappas, and J. M. Martinis, Rev. Sci. Instrum. **75**, 2726 (2004).

172 P. J. Eaton and P. West, *Atomic force microscopy* (Oxford University Press, Oxford, NY, 2010).

173 D. B. Williams and C. B. Carter, *Transmission electron microscopy: a textbook for materials science* (Springer, New York, 2008).

174 W. Buckel and R. Kleiner, *Superconductivity: fundamentals and applications* (Wiley-VCH, Weinheim, 2004).

175 J. Clarke and A. I. Braginski, *The SQUID handbook* (Wiley-VCH, Weinheim, 2004).

[176] J. D. McCullough and K. N. Trueblood, Acta Crystallogr. **12**, 507 (1959).

[177] M. P. Agustin, G. Bersuker, B. Foran, L. A. Boatner, and S. Stemmer, J. Appl. Phys. **100**, 024103 (2006).

[178] J. H. Park, J. S. Hyun, B. C. Kang, and J. H. Boo, Surf. Coat. Technol. **201**, 5336 (2007).

[179] E. P. Gusev, H. Shang, M. Copel, M. Gribelyuk, C. D'Emic, P. Kozlowski, and T. Zabel, Appl. Phys. Lett. **85**, 2334 (2004).

[180] C. Liu, E. F. Chor, and L. S. Tan, Semicond. Sci. Technol. **22**, 522 (2007).

[181] H. S. Kim, I. Ok, M. H. Zhang, F. Zhu, S. Park, J. Yum, H. Zhao, and J. C. Lee, Appl. Phys. Lett. **91**, 042904 (2007).

[182] Y. Q. Wu, Y. Xuan, T. Shen, P. D. Ye, Z. Cheng, and A. Lochtefeld, Appl. Phys. Lett. **91**, 022108 (2007).

[183] M. Kundu, N. Miyata, T. Nabatame, T. Horikawa, M. Ichikawa, and A. Toriumi, Appl. Phys. Lett. **82**, 3442 (2003).

[184] K. Hasegawa, P. Ahmet, N. Okazaki, T. Hasegawa, K. Fujimoto, M. Watanabe, T. Chikyow, and H. Koinuma, Appl. Surf. Sci. **223**, 229 (2004).

[185] C. Wiemer, M. Fanciulli, B. Crivelli, G. Pavia, and M. Alessandri, Appl. Phys. Lett. **83**, 5271 (2003).

[186] E. K. Hollmann, O. G. Vendik, A. G. Zaitsev, and B. T. Melekh, Supercond. Sci. Technol. **7**, 609 (1994).

[187] M. Yoshimoto, T. Maeda, T. Ohnishi, H. Koinuma, O. Ishiyama, M. Shinohara, M. Kubo, R. Miura, and A. Miyamoto, Appl. Phys. Lett. **67**, 2615 (1995).

[188] K. K. Bharathi, N. R. Kalidindi, and C. V. Ramana, J. Appl. Phys. **108**, 083529 (2010).

[189] J. Aarik, A. Aidla, A. A. Kiisler, T. Uustare, and V. Sammelselg, Thin Solid Films **340**, 110 (1999).

[190] M. Y. Ho, et al., J. Appl. Phys. **93**, 1477 (2003).

[191] D. M. Adams, S. Leonard, D. R. Russell, and R. J. Cernik, J. Phys. Chem. Solids **52**, 1181 (1991).

[192] A. Benyagoub, Eur. Phys. J. B **34**, 395 (2003).

[193] K. Cherkaoui, et al., J. Appl. Phys. **104**, 064113 (2008).

[194] V. Sammelselg, R. Rammula, J. Aarik, A. Kikas, K. Kooser, and T. Kaambre, J. Electron. Spectrosc. Relat. Phenom. **156**, 150 (2007).

[195] M. Modreanu, J. Sancho-Parramon, D. O'Connell, J. Justice, O. Durand, and B. Servet, Mater. Sci. Eng. B **118**, 127 (2005).

[196] R. I. Barabash, W. Donner, and H. Dosch, Appl. Phys. Lett. **78**, 443 (2001).

[197] I. Vartanyants, C. Ern, W. Donner, H. Dosch, and W. Caliebe, Appl. Phys. Lett. **77**, 3929 (2000).

[198] M. Gillet, A. Al-Mohammad, and C. Lemire, Thin Solid Films **410**, 194 (2002).

[199] J. Robertson, MRS Bulletin **27**, 217 (2002).

[200] J. Aarik, H. Mandar, M. Kirm, and L. Pung, Thin Solid Films **466**, 41 (2004).

[201] S. S. Hullavarad, D. E. Pugel, E. B. Jones, R. D. Vispute, and T. Venkatesan, J. Electron. Mater. **36**, 648 (2007).

[202] S. Miyake, I. Shimizu, R. R. Manory, T. Mori, and G. Kimmel, Surf. Coat. Technol. **146**, 237 (2001).

[203] N. Hadacek, A. Nosov, L. Ranno, P. Strobel, and R. M. Galera, J. Phys. Condens. Matter **19**, 486206 (2007).

[204] J. Mannhart and D. G. Schlom, Nature **430**, 620 (2004).

[205] A. Kalabukhov, R. Gunnarsson, J. Borjesson, E. Olsson, T. Claeson, and D. Winkler, Phys. Rev. B **75**, 121404 (2007).

[206] E. E. Hoppe, R. S. Sorbello, and C. R. Aita, J. Appl. Phys. **101**, 123534 (2007).

[207] J. W. Park, D. K. Lee, D. Lim, H. Lee, and S. H. Choi, J. Appl. Phys. **104**, 033521 (2008).

[208] Y. B. Zheng, S. J. Wang, and C. H. A. Huan, Thin Solid Films **504**, 197 (2006).

[209] H. Tomaszewski, H. Poelman, D. Depla, D. Poelman, R. De Gryse, L. Fiermans, M. F. Reyniers, G. Heynderickx, and G. B. Marin, Vacuum **68**, 31 (2002).

[210] V. K. S. Shante and S. Kirkpatrick, Adv. Phys. **20**, 325 (1971).

[211] T. Dietl, H. Ohno, F. Matsukura, J. Cibert, and D. Ferrand, Science **287**, 1019 (2000).

[212] C. Ko, M. Shandalov, P. C. McIntyre, and S. Ramanathan, Appl. Phys. Lett. **97**, 082102 (2010).

[213] S. Capone, G. Leo, R. Rella, P. Siciliano, L. Vasanelli, M. Alvisi, L. Mirenghi, and A. Rizzo, J. Vac. Sci. Technol. A **16**, 3564 (1998).

[214] D.-Y. Cho, L. Jae-Min, S. J. Oh, H. Jang, J. Y. Kim, J. H. Park, and A. Tanaka, Phys. Rev. B **76**, 165411 (2007).

[215] K. C. Liu, J. R. Tsai, W. K. Lin, C. S. Li, and J. N. Chen, Thin Solid Films **519**, 5110 (2011).

[216] G. Bouzerar and T. Ziman, Phys. Rev. Lett. **96**, 207602 (2006).

[217] H. Takeuchi, D. Ha, and T. J. King, J. Vac. Sci. Technol. A **22**, 1337 (2004).